IJCESEN

Indexing/Abstracting Databases

ASOS indeks

INDEX COPERNICUS INTERNATIONAL

INTERNATIONAL SERVICES FOR IMPACT FACTOR AND INDEXING (ISIFI)

GENERALIMPACTFACTOR
Universal Digital Object Information

Google Scholar

DRJI

ISI INTERNATIONAL Scientific Indexing

publons

Cosmos

SIS

J-Gate

WorldCat

ESJI Eurasian Scientific Journal Index
www.ESJIndex.org

JIF JIFACTOR

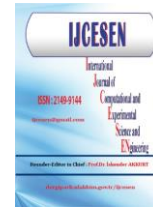CiteFactor
Academic Scientific Journals

Academic Resource Index
ResearchBib

Scientific Journal Impact Factor
TOGETHER WE REACH THE GOAL

Table of Contents

ResearchArticle

Comparison of Experimental Curves of Alloy Steels after Gas Nitriding

Naim SYLA[1], Fisnik ALIAJ[2,*], Njomza ELEZAJ[3], Bashkim DALIPI[4]

[1]University of Prishtina, Department of Physics, Eqrem Cabej Str. 51, 10000 Prishtina, Republic of Kosovo
naim.syla@uni-pr.edu -- **ORCID:** 0000-0003-0857-4685

[2]University of Prishtina, Department of Physics, Eqrem Cabej Str. 51, 10000 Prishtina, Republic of Kosovo
* **Corresponding Author** : fisnik.aliaj@uni-pr.edu-- **ORCID:** 0000-0002-9967-8334

[3]University of Prishtina, Department of Physics, Eqrem Cabej Str. 51, 10000 Prishtina, Republic of Kosovo
njomza.elezaj@uni-pr.edu -- **ORCID:** 0000-0003-3967-8452

[4]University of Gjilan, Faculty of Education, Zija Shmesiu Str. 3, 60000 Gjilan, Republic of Kosovo
bashkim.dalipi@uni-gjilan.net -- **ORCID:** 0000-0002-8133-0452

Abstract:

This study is concerned with experimental curves of: hardness, residual stress and concentration of nitrogen at the precipitation layer at alloy steels after gas nitriding. The purpose of this treatment is that through experimental curves to identify the relationship and causality between hardness, on one side, and on the other, residual stress respectively concentration of nitrogen. Comparing the shape and slope of these curves we can conclude that, concentration of diffused nitrogen on the steel lattice, respectively ferrite, is a cause of increased hardness at the precipitation layer. More to the point, as a result of nitrogen diffusion, residual stress emerge which cause increase of hardness. The intensity and slope of the curves of hardness depends on the intensity and slope of the nitrogen concentration respectively residual stress.

1. Introduction

With the aim of improving the physical characteristics of iron materials, and more specifically of steels, various methods are used, and one of them is nitriding [1-8]. This process takes place in temperatures of over 500^0C and in solid, liquid or gas environments [9]. Irrespective of the environment in which nitriding takes place, the aim is almost the same: enriching the steel's surface with atomic nitrogen. As a result of the diffusion (enrichment) of the nitride on the surface of the material, physical changes occur within it and these are noticeably improved by the conditions of application of different equipment [10-14]. In this paper we deal with the results of nitriding of two types of steel in gas environments. Specifically, we have researched the effect of nitriding on 16MnCr5 and 31CrMoV9 steel in the temperatures of 550^0C

and 590^0C and over two periods of time, giving a total of eight samples.

2. Method

The nitriding process was carried out in an air dopped ammonia atmosphere with the nitriding potentials as given in Table 1, while the nitriding period was chosen such that comparable layers of nitriding could be obtained for different temperatures as in Table 2.

Before the samples were investigated experimentally they were prepared metallographically with grinding and polishing of their surface. The details of specimen preparation are given in our earlier papers [11, 15]. The chemical analysis of the samples was carried out with a spark emission spectroscopy (Jobin Yvon, model JY-132F), and the results are listed in Table 3. The experimental research methods were: Vickers method for hardness measurements, Electron Probe Micro-Analysis (EPMA) for

nitrogen-depth profiling, and X-ray diffraction (XRD) method for residual stress analysis.

Hardness measurement were performed on polished cross-sections of nitrided specimens by using a PCE Leco hardness tester under a load of 0.9807 N ($HV_{0.1}$). The distance between two succsesive measuring points was 50 μm. For comparison purposes, five more hardness measurements were taken outside of the nitrided area, i.e., in the matrix. Nitrogen concentration-depth profiles were determined with a Joel JXA-8900RL microanalyser operated at 20 kV and 40 nA. EPMA measurements were performed on polished cross-section of nitrided specimens, perpendicular to the surface, starting at the surface and moving in 5 μm increments towards the depth. Residual stresses were evaluated with XRD by using a Huber diffractometer with Cr-Kα radiation on the {211} diffraction plane of α-Fe. The $\sin^2\psi$ method [16-18] was used with the following measuring conditions: voltage/current X-ray tube parameters 40 kV/30 mA, measuring interval $\sin^2\Psi = 0$ to ±0.5, measuring step width $\Delta\sin^2\Psi = 0.1$, measuring time interval 10-20 s, α-Fe elastic constants $E_{(211)} = 220$ GPa and $\nu_{(211)} = 0.8$.

***Table 1.** Nitriding parameters*

Temp./ °C	The atmosphere of nitriding	Nitriding potential, K_n
550	Air dopped ammonia gas	3
590	Air dopped ammonia gas	2.82

***Table 2.** Sample labelling, nitriding temperature and time*

Temp./ °C	Time /h	Sample label	
		16MnCr5	31CrMoV9
550	9	16-9	31-9
	64	16-15	31-15
590	4	16-17	31-17
	36	16-23	31-23

3. Results and Discussions

For each sample we found experimental curves for strength (HV), residual stress (RS), and the profile of distribution of nitrogen (N). Subsequently, with the aim of comparing the experimental results, we presented the curves jointly in a graphic. In order to for the comparison to be clearer, we normed the maximal values of HV, RS and N as 1 so that on

the *y* axis we can see the relative impact of these values on depth. The results were displayed in figüre 1-8.

4. Conclusions

The intensity of curve N is in proportion with that of RS and HV. The more nitride diffuses in the steel network (the greater the intensity of curve N) the higher the intensity of residual stress RS. This is the case because during nitriding, deformation occurs to the steel network which produces stress in (negative) pressure. Likewise, the intensity of the residual stress RS is comparable with that of HV. In this assessment we consider that the diffusion of nitrogen causes residual stress in the network and as a result an increase occurs in the HV strength of the steel. Since the diffusion of nitrogen depends on the nitriding conditions it is possible to change the physical characteristics of steel and in this specific case by using the parameters of nitriding – time, temperature, nitriding potential and the type of steel.

***Table 3.** Chemical composition (in wt.%) of steels. The difference to 100 wt.% is Fe*

	16MnCr5	31CrMoV9
C	0.18	0.29
Cr	0.71	2.17
Mn	1.06	0.70
V	0.001	0.15
Mo	0.009	0.27
Si	0.31	0.26
S	0.026	0.004
P	0.028	0.016
Al	0.088	0.022

***Figure 1.** HV, RS and N curves for sample of 16_9 (see table 2)*

Figure 2. *HV, RS and N curves for sample of 16_15 (see table 2)*

Figure 3. *HV, RS and N curves for sample of 16_17 (see table 2)*

Figure 4. *HV, RS and N curves for sample of 16_23 (see table 2)*
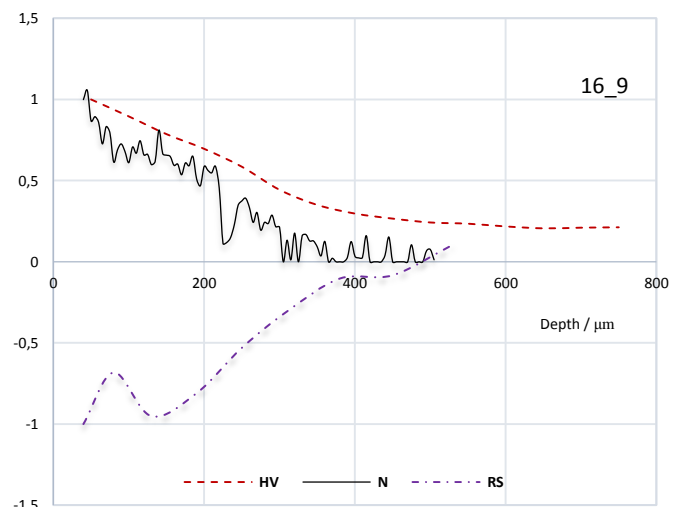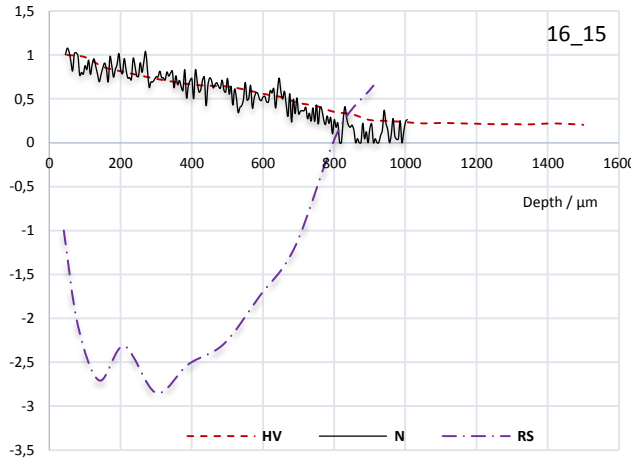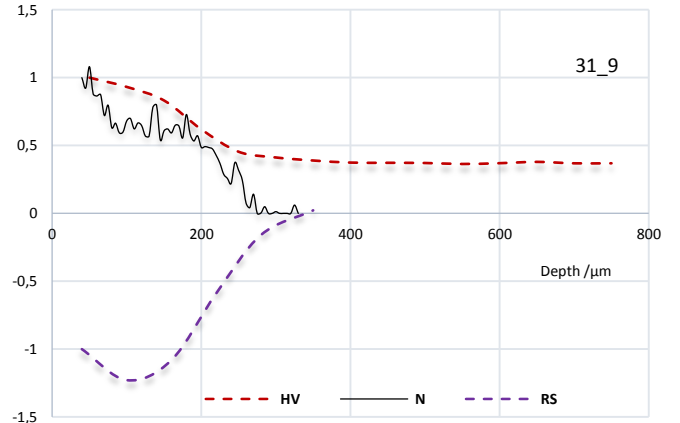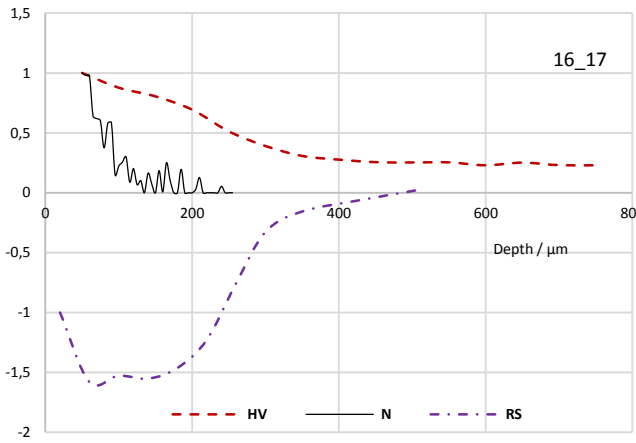

Figure 5. *HV, RS and N curves for sample of 31_9 (see table 2)*

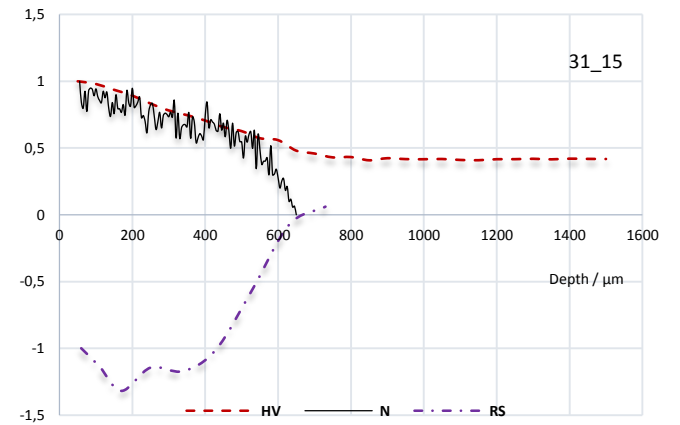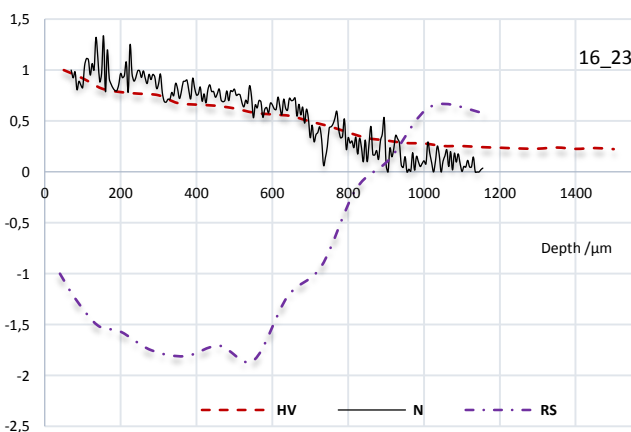**Figure 6.** *HV, RS and N curves for sample of 31_15 (see table 2)*
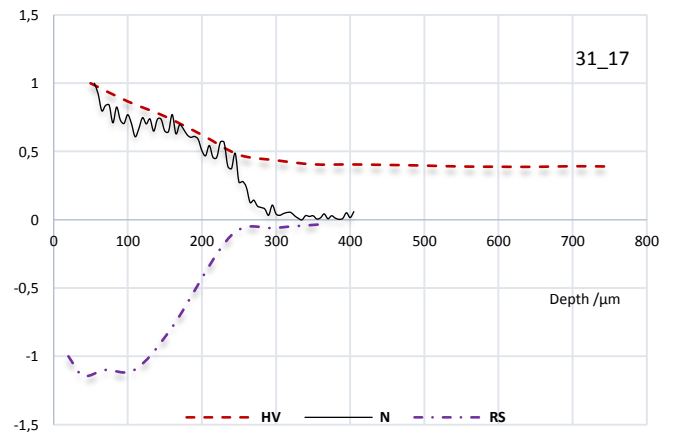
Figure 7. *HV, RS and N curves for sample of 31_17 (see table 2)*
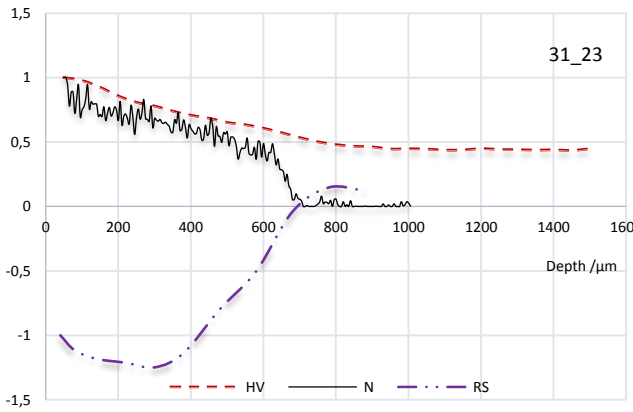
Figure 8. *HV, RS and N curves for sample of 31_23 (see table 2)*

Author Statements:

- The authors declare that they have equal right on this paper.
- The authors declare that they have no known competing financial interests or personal relationships that could have appeared to influence the work reported in this paper
- The authors acknowledge that this paper presented as oral presentation in ICCESEN

References

[1] I. Altinsoy, G. F. Çelebi Efe, T. Yener, K. G. Önder, and C. Bindal, Effect of double stage nitriding on 34CrAlNi7-10 nitriding steel, Acta Phys. Pol. *A* 132 (2017) 663-666. *DOI:* 10.12693/APhysPolA.132.663

[2] C. W. Kang, S. R. Meka, T. Steiner, R. E. Schacherl, and E. J. Mittemeijer, Microstructural evolution of 31CrMoV9 steel upon controlled gaseous nitriding treatment, HTM - J. Heat Treat. Mater. 71 (2016) 181-190. *DOI*: 10.3139/105.110296

[3] N. Syla, N. Elezaj, F. Aliaj, Z. Tolaj, and A. Zeqiraj, Finite element modeling of 31CrMoV9 steel hardness curves after gas nitriding, Indian J. Chem. Technol. 26 (2019) 358-361.

[4] N. Syla, B. Dalipi, N. Elezaj, F. Aliaj, Z. Tolaj, and A. Zeqiraj, Finite element (FE) modeling of the nitrogen concentration profile in 31CrMoV9 steel after gas nitriding, Emerg. Mater. Res. (2019), Accepted.

[5] D. Mohamed, B. N. Eddine, and D. Nacer, Effect of substrate preheating, roughness and particle size on splat morphology of thermal sprayed coatings, Int. J. Comput. Exp. Sci. Eng. 1 (2015) 16-18.

[6] N. Ozsoy, and M. Ozsoy, Optimization of surface roughness in the turning process of AISI 4340 tempering steel, Emerging Mater. Res. 9 (2020). *DOI:* 10.1680/jemmr.18.00141

[7] E. Altuncu, and M. Tarim, Laser cladding of martensitic stainless steels on armor steels, Emerging Mater. Res. 9 (2020). *DOI:* 10.1680/jemmr.18.00120

[8] N. Syla, A. Zeqiraj, N. Hasi, and N. Elezaj, Investigation of the compound layer formed by steel 16MnCr5 after gas nitriding, Emerging Mater. Res. 9 (2020). *DOI:* 10.1680/jemmr.18.00117

[9] E. J. Mittemeijer, in ASM Handbook: Fundamentals of Nitriding and Nitrocarburizing, Eds. J. L. Dossett and G. E. Totten, Vol. 4A (ASM International, Ohio, 2013) pp. 619-646. *DOI:* 10.31399/asm.hb.v04a.a0005818

[10] Z. Pokorný, D. Dobrocký, J. Kadlec, and Z. Studený, Influence of alloying elements on gas nitriding process of high-stressed machine parts of weapons, Met. Mater., 56 (2018) 97–103. *DOI*: 10.4149/km_2018_2_97

[11] N. Syla, F. Aliaj, and B. Dalipi, The law of growth of nitrided layer in 31CrMoV9 steel, Acta Phys. Pol. *A* 130 (2016) 83-86. *DOI:* 10.12693/APhysPolA.130.83

[12] M. A. Terres, L. Ammari, and A. Chérif, Study of the Effect of Gas Nitriding Time on Microstructure and Wear Resistance of 42CrMo4 Steel, Mater. Sci. Appl. 8 (2017) 93–507. *DOI:* 10.4236/msa.2017.86034

[13] W. A.-R. Dhafer, V. Kostyk, K. Kostyk, A. Glotka, and M. Chechel, The choice of the optimal temperature and time parameters of gas nitriding of steel, Eastern-European J. Enterp. Technol. 3 (2016) 44-50. *DOI:* 10.15587/1729-4061.2016.69809

[14] N. Syla, F. Aliaj, and M. Rama, Hardness curves for 31CrMoV9 steel after gas nitriding, Acta Phys. Pol. A 132 (2017) 484-486. *DOI:* 10.12693/APhysPolA.132.484

[15] N. Syla, F. Aliaj, Z. Tolaj, N. Mahmudi, and A. Zeqiraj, "The gas nitriding behavior of 31CrMoV9 grade steel," J. Eng. Appl. Sci. 13 (2018) 6713-6718

[16] I. C. Noyan, J. B. Cohen. Residual stress – measurement by diffraction and interpretation, Springer-Verlag, New York, 1987

[17] F. Aliaj, and N. Syla, Influence of Al Content and Bias Voltage on the Microstructure of Ti1-xAlxN Hard Coatings, J. Eng. Appl. Sci., 5 (2010) 394–402. *DOI:* 10.3923/jeasci.2010.394.402

[18] P. S. Prevéy, Current applications of XRD diffraction residual stress measurement, Dev. Mater. Charact. Technol. ASM Int., 513 (1996) 103-110

Research Article

Optimization of Stamping Process Parameters

Tunahan ÇİFTÇİ[1*], Levent AYDIN[2], İrem ERTEN[3]

[1]Student, İzmir Kâtip Çelebi University, Mechanical Engineering Department, İzmir-Turkey
* **Corresponding Author** : tunahan-cftc@hotmail.com -- **ORCID:** 0000-0003-4833-896X

[2]Instructer, İzmir Kâtip Çelebi University, Mechanical Engineering Department, İzmir-Turkey
leventaydinn@gmail.com-- **ORCID:**0000-0003-0483-0071

[3]Student, İzmir Institute of Technology, Mechanical Engineering Department, İzmir-Turkey
erteniremm@gmail.com -- **ORCID:**0000-0002-6103-0030

Abstract:

Stamping is one of the significant sheet metal forming process which is used for producing components especially in automobile industry. Sheet metal flow into the die cavity occurs the applied force in stamping process. While the extreme compressive stresses of sheet metal end up with wall thickening, tensile stresses lead of thinning problems in the wall zone of the part. The excessive thinning may cause crack formation or fracture of the metal sheet. This faulty process design eventually produces non-conforming products. In order to have successful design of stamping process, designing of tooling and identification of the optimum level of the process parameters are needed. In this regard, the present paper is an attempt to set the stamping process parameters for minimum thinning of blank and optimal results by a stochastic search method (modified Differential Evolution) based on multiple nonlinear regression analysis. The results have been compared with the results those of the previous study. It is shown that the current results show that the present optimization study is successful as further increase the thickness.

1. Introduction

The stamping process is a process in which variety of sheet metal forming production processes, such as; punching, drawing, bending, flanging, coining and embossing are performed by using machine presses or stamping presses. The process is generally carried out the sheet metals as well as other materials such as polystyrene.
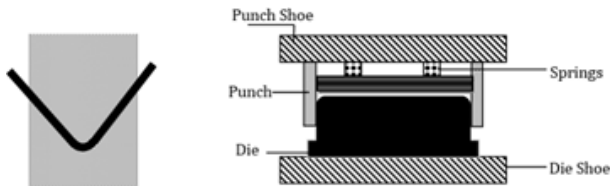
(a) Bending using matched (b) Wipe Forming punch and die set

Figure 1. *a) Bending using matched punch and die set [2]   b) Wipe forming [2]*

Stamping can be done in a single mold station or in multiple mold stations with the help of progressive dies. When the workpiece has a bending angle greater than 90 ° or the part contains intermittent properties, progressive dies are generally used [1].
As showing in figure 1. bending using matched punch and die set (in a) and wipe forming (in b) [2]. During the design of prosperous sheet metal forming process, it is need of real experiments to reach a successful prod.uct as well as expensive and time-consuming prototype tests [3].

One of the significant step of stamping is the drawing processing. In the drawing, the plate holder is formed against the mold with the help of the upper die of punch, while the blank holder is applied to the mold by a foregone force in order to check the material flow. In the drawn part, usually the team experiment stage, forming errors which are wrinkling, thinning and fracture of the material are monitored [4,5]. The Finite Element Method

(FEM) is comprehensively put to use for simulation of sheet metal forming to remove unwanted forming defects, and to anticipate blank stresses for prevent failures [6,7]. The parameters which are related to the blank geometry, work material, die and presses are some of the important parameters that influence the process. Also the other significant process prameters are punch radius, die radius, blank holder force, draw tonnage, binder stroke, drawbead hight and contect coefficient of friction.

Figure 2. Example of Forming Error, Cracking [8]

An example of Forming Error, Cracking is shown in figüre 2 [8]. It is quite hard to determine the process parameter effects on the quality of final product. For the better efficiency of the process, the parameters must set at an optimum level [9]. The traditional method of determination the optimum level of the process parameter is expensive and time consuming. It seriously depends on the trial and error, expertise, and skill of workers. The improper setting of the parameters can cause to manufacturing of faulty products. So the primary purpose of stamping process designers is designing manufacture forming tools and setting process parameter for the production of flawless products within the required surface quality and desired dimensional tolerances. In the present study, it is aimed to create an 'Objective Function' that expresses the relation between predictor parameters and response of stamping process by using the FEM simulation results from the reference article [10]. Optimization works at this stage and enables to find the conditions where the process parameters are optimum level.

1.1. Process parameters

The process parameters which is also called as 'Desing Variables'of the stamping process are given in the Table 1.

DR. Die Radius

The radius of die is the one of the parameters that influences drawing operations using the flat blank holder. When the die radius set too bit, there is

Table 1. Process Prameters of Stamping Process [10].

Nomenclature
DR Die radius (mm)
PR Punch radius (mm)
DT Draw tonnage (Ton)
BH Blank holder force (Ton)
BS Binder stroke (mm)
CCF Contact coefficient of friction
DH Drawbead height (mm)

chance of split of material owing to the excessive limiting force which are caused by the sheet's bending and unbending around a small radius. Besides, these bending and unbending generate heat in high quantity throughout the operation. Nevertheless, wrinkling of blank occurs due to a large die radius [10,11].

PR. Punch Radius

Pressure is practiced by using a punch standing on the blank results in deformation in sheet metal forming. For material behaviour, the punch radius is an important influence, the tiny radius punch leads to shearing of the sheet metal between the die and punch, while the excessive radius causes strecthing of the sheet throughout the radius. The proper punch selection is affected by material properties and thickness of a blank [10,12,13,14].

DT. Draw Tonnage

DT is the required force for the blank's deformation in the desired form. The too many variations in present DR might cause the faults. It can be given examples for faults such as compressive stresses development in the blank and unfinished deformation of the blank [10].

BHF. Blank Holder Force

Inadequate material flow into the die causes stretching and ultimately causes blank's tearing. In contrast, the excessive flow results in blank's wrinkling. Thus, the optimal setting of blank holder force might prevent the occurrence of wrinkling and tearing in the installed part. The fundamental blank holder force characteristically is applied by the press cushion system. Blank holder force checks the material flow in the die and significant impact on quality of the product. Higher BHF reduces wrinkling in deep drawn products. However, it is common practice (maybe, it might be application to calculate the minimum required BHF [10,15,17].

BS. Binder Stroke

In forming operations of the sheet metal, the circumferential compressive force is exerted by a punch on blank force the blank in the die cavity, whereas the blank put up resistance to flow. The blank's quite high resistance to flow might cause crack of the cup. The blank's thinning and stretching are also affected by the distance between post and blank edge. When the post is properly set from the blank edge, and the die's inlet radius is properly placed, the metal enters into the die as gradually and freely flow in the cavity. Binder stroke is accommodately locked by using shoulder bolts or spool keepers [10].

CCF. Contact Coefficient Friction

Contact coefficient friction has crucial influence on the quality of surface of the product. The static friction between the blank and tool affects draw ability of sheet metal. The existence of decent lubricating film between the contact areas is crucial for getting more effective stamping process qua strain distribution in the vacancy is influenced by contact friction. Also the contact friction makes contribution to the blank wear and tool. The more stable strain distribution is possible when the large value of full film lubrication regions applied. The largest contact area ratio is happened when the surface roughness of blank and mold contacts, and it will couses the larger frictional stress values. Friction which have lower value cause a more stable radial strain distribution [10,12,18].

DH. Drawbead Height

The draw bead and blank holder provide the restrictive force which is required for controling the material flow. The minor groove on the binder surface/die surface, which is called the draw bead, matched together by a protrusion on the die or binder surface. After the binder with closure, the sheet metal is drawn above the drawbead [10,19].

2. Methods

2.1. Optimization

Optimization can be defined as making something the best as much as possible by using of any available resources. With optimization by using the mathematical function, results can be maximized or minimized with respect to the desired situation, by changing with specific parameters. To make optimization studies which is related to a subject, firstly we should have certain data set composed of parameters which is called as design variables.

After that with respect to regression analysis type the mathematical model which is called as 'Objective Funtion' of the problem must be defined. After that the objective function can be minimized or maximized by optimization [20].

2.2. Regression

The definition of regression analysis can be described as forming approximative modelling technique that examines relationships between independent and dependent variables. This technique is used for estimating, finding and modelling the causative effects to the relationships between the variables. In the analyzing and modelling data, regression analysis is crucial technique. There are also several advantages of this technique. Such as:

- Important relationships between the dependent variables and independent variables can be indicated by regression.

- It enables to see the power of effects of several independent variables on a dependent variable.

Also, comparing the effects of variables, which made measurement on different scales, for instance, the effect of price changes and the number of promotional activities, are calculated by the regression analysis. These advantages offer service market researchers, data scientists or data analysts to evaluating and selecting the best set of variable to be used for setup successfull approximative models between the input and output variables [21].

There exist several kinds of useful regression methods in order to make a guess. In the main, these methods are seperated into three groups such as; number of independent variables, dependent variable types and regression line shape (See Fig. 3).
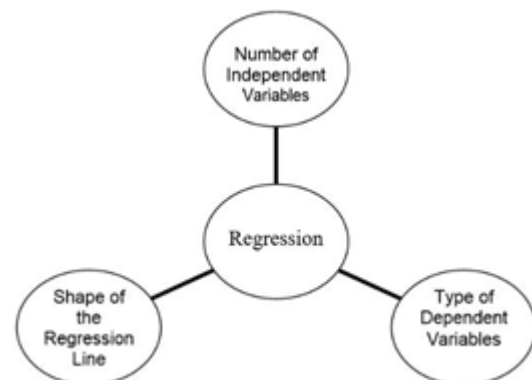

Figure 3. *Various kinds of regression techniques [21].*

The regression analysis may be linear/non-linear or may multiple/simple. These are the examples of regression techniques;

- Linear Regression
- Logistic Regression
- Polynomial Regression
- Stepwise Regression
- Lasso Regression
- ElasticNet Regression
- Ridge Regression

In the peresent study, multiple non-linear regression analysis was used and the mathematical model of the problem was formed as second order multiple polynomial function [21].

2.3. Wolfram Mathematica

In present study, the regression and optimization studies were performed by using 'Wolfram Mathematica' Software.

Mathematical operations with mathematics, equations, integrals, matrices, arrays, functions, vectors can be made with a few simple Wolfram Language commands. Wolfram Mathematica, with its features in mathematics, provides solutions in a very short time. Wolfram Mathematica includes the Wolfram Notebook file type, which has an .nb extension for you to do any kind of process or project, including mathematical operations. In this file type, you can write your commands int input cells and display the output of your codes in Out cells. The commands that used in the present study by using Mathematica, is introduced below [22].

2.3.1. FindFit

The general expression of FindFit command can be described as:
FindFit [data, expr, pars, vars]
This command finds out numerical values of design parameters which is represented as 'pars' that make 'expr' give best fit to 'data' as a function of 'vars'. The possible method choice include for the FindFit command, "ConjugateGradient", "Gradient", "LevenbergMarquardt", "Newton", "NMinimize", and "QuasiNewton", with the default being Automatic that was used in the present study [22].

2.3.2. NMinimize

The general expression of NMinimize command can be described as:
NMinimize [f, x∈ reg]

This command minimizes f function numerically with respect to x and constrains x to be in the region reg. The Method option in Mathematica for the NMinimize command include "NelderMead", "DifferentialEvolution", "SimulatedAnnealing", and "RandomSearch". The method was chosen as default being Automatic in the present study [22].

3. Problem Definition

The problem that concerned in this study is the thinning problem that occurs in stamping process. Thinning problem is caused when thickness variation in metal forming operation beyond the limit and it is the important fault of concern at the die tryout stage, while ideally the thickness of the stamped component is desired to remain unchanged. Thinning of the sheet at several critical sections or points might cause thinness of the wall and might cause cracking.

In the reference article, the data set consisting of 27 experiments were obtained from the experiments with FEM simulations by using Taguchi Orthogonal Array Method. In the present study, the data set that taken from the reference article was used. Simulation results for 27 experiments of Stamping process are given in Table 2.

Table 2. *Simulation Results for L27 Orthogonal Array Experiments [10].*

Run				Parameters				Thinning
	DR	PR	DT	BH	BS	CCF	DH	(%)
1	19.2	20	350	35	100	0.125	6	27.42
2	19.2	20	350	35	110	0.250	8	22.89
3	19.2	20	350	35	120	0.375	4	--
4	20.2	20	300	40	100	0.125	6	20.18
5	20.2	20	300	40	110	0.250	8	17.65
6	20.2	20	300	40	120	0.375	4	22.13
7	18.2	20	325	45	100	0.125	6	20.27
8	18.2	20	325	45	110	0.250	8	20.74
9	18.2	20	325	45	120	0.375	4	25.22
10	19.2	22	325	40	100	0.375	8	18.06
11	19.2	22	325	40	110	0.125	4	18.54
12	19.2	22	325	40	120	0.250	6	--
13	20.2	22	350	45	100	0.375	8	24.69
14	20.2	22	350	45	110	0.125	4	18.16
15	20.2	22	350	45	120	0.250	6	19.86
16	18.2	22	300	35	100	0.375	8	20.63
17	18.2	22	300	35	110	0.125	4	22.10
18	18.2	22	300	35	120	0.250	6	17.00
19	19.2	18	300	45	100	0.250	4	15.35
20	19.2	18	300	45	110	0.375	6	22.27
21	19.2	18	300	45	120	0.125	8	19.74
22	20.2	18	325	35	100	0.250	4	25.18
23	20.2	18	325	35	110	0.375	6	28.87
24	20.2	18	325	35	120	0.125	8	30.35
25	18.2	18	350	40	100	0.250	4	26.14
26	18.2	18	350	40	110	0.375	6	27.94
27	18.2	18	350	40	120	0.125	8	25.31

3.1. Mathematical Modelling

The modelling of the problem was made by using multiple non-linear regression analysis method on Wolfram Mathematica.

Firstly, the Design Variables were introduced to the program as 'x1, x2, x3, x4, x5, x6, x7' correspond to the 'DR, PR, DT, BH, BS, CCF, DH' respectively. The output variable which is Thinning was introduced as ' t' and for the missing two output variables values were added as the mean value of the output values which is '21.68'. As 1st trial linear regression model had tried and the genaral expression of the function is;

$$y = a_0 + \sum^{n} a_i x_i \qquad (1)$$

The objective function with respect to linear regression model was defined as by using 'FindFit' command on Mathematica;

t = 26.3348 - 1.1525 x1 + 0.0955556 x2 -0.319556 x3 + 0.0799556 x4 + 0.0162778 x5 + 0.183889 x6 + 3.71556 x7

$$(2)$$

But the R^2 value in according to this model was determined as 0.563326 which showed that the model is not appropriate for the problem, thus as trial 2nd order polinomial regression model had tried. The genaral expression of the function is;

$$y = a_0 + \sum_{i=1}^{n} a_i x_i + \sum_{i=1}^{n} a_{ii} x_i^2 + \sum_{i=1}^{n}\sum_{j<i}^{n} a_{ji} x_j x_i \quad (3)$$

The result show that the mathematical model is good. The mathematical model 'Objective Function' with respect to 2nd order polynomial multiple regression model was defined as by using 'FindFit' command on Mathematica;

t = 66.0439 + 2.42924 x1 + 0.060683 x1^2+ 0.457953 x2 - 0.195938 x1 x2 +0.159102 x2^2 - 4.19963 x3 + 0.0158941 x1 x3 - 0.247609 x2 x3 +0.0276474 x3^2 - 0.00185789 x4 - 0.0107405 x1 x4 +0.00896666 x2 x4 + 0.0106789 x3 x4 - 0.000306033 x4^2 +0.125582 x5 + 0.000599765 x1 x5 + 0.0483611 x2 x5 + 0.0191 x3 x5 -0.00202111 x4 x5 - 0.00302376 x5^2 + 3.02032 x6 + 0.197952 x1 x6 -0.032798 x2 x6 - 0.00301794 x3 x6 + 0.0135547 x4 x6 -0.0545488 x5 x6 - 0.288759 x6^2 - 78.96 x7 - 2.51938 x1 x7 -1.09745 x2 x7 + 2.52829 x3 x7 + 0.141346 x4 x7 -
0.545977 x5 x7 -3.65277 x6 x7 + 163.959 x7^2

$$(4)$$

According to this mathematical model, the R^2 value was determined as 0.944946.

Some graphs were created between the fitness function and DR in order to understand how the obtained model produces values by changing the system parameters (See Figs. 4-7).

Figure 4. *Variation of sistem output vs DR for different DH values.*

Figure 5. *Variation of sistem output vs DR for different BS values.*

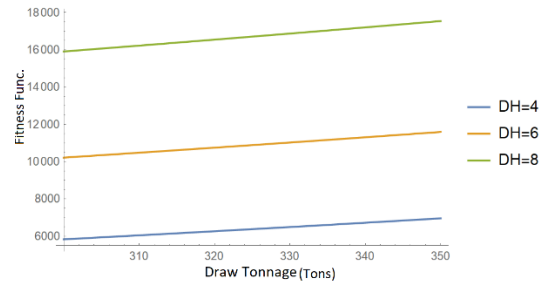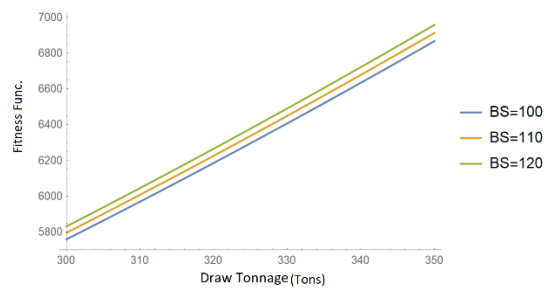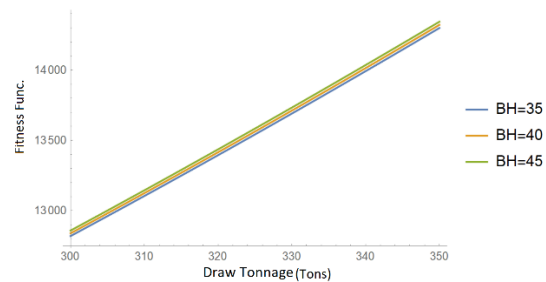***Figure 6.*** *Variation of sistem output vs DR for different BH values.*
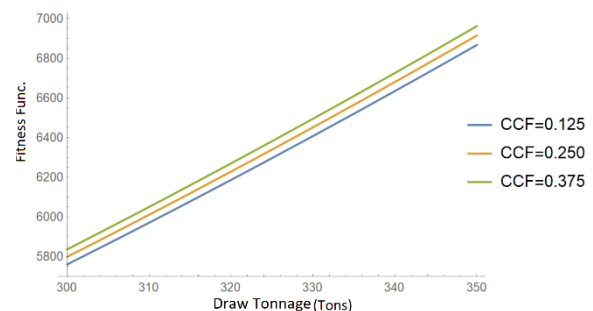

Figure 7. *Variation of sistem output vs DR for different CCF values.*

When the figures are examined, it is possible to see that the output increases linearly with the increase of DR for all cases. In addition, it is obvious that the effect due to the change of DH is much more than the other three parameters. Secondly, we can

say that the least effective parameter is the BH, besides, the effect value of CCF and BS difference is close to each other.

4. Results and Discussion

The goal of the study is setting the stamping process parameters for minimum thickness and the optimization study results for thinning problem of the reference article, were given as;

These results shows that the optimized design parameters setting as shown in table 3.

Table 3. Optimized Stamping Process Parameters of Ref.[10] and Present Study

	Ref. [10]	Present Study
Parameter	Value	Value
PR	22 mm	22 mm
DR	19.19 mm	20.2 mm
BHF	44.39 Ton	45 Ton
DT	300 Ton	300 Ton
CCF	0.208	0.2122
BS	-	100 mm
DH	-	4 mm

In reference study, the minimum thinning percentage was defined as 11.613 % which is corresponding to minimum thickness of component is 0.707 mm.

In the present study, optimized parameters of stamping process were defined according to the modified Differential Evolution method.

The minimized output (thinning percentage) was defined as 8.53 % with respect to the optimized parameters for minimum thickness. These results corresponding to the amount of thickness is 0.519 mm. If the optimized process parameters of the present and the reference study compared the results shows that even small amount of increasing of the die radius, blank holder force and contact coefficient of friction values provides quite decreasing in thickness of the product. When these two thinning results compare, it shows that the present optimization study is successful as further increase the thickness.

5. Conclusion

Linear and second order multiple polinomial regression models were tried to obtain the mathematical model of the relation between process parameters and the result. In present study, there are 7 design parameters which thinning percentage.

Firstly, linear regression model was tried and it was decided to be insufficient because the result of R^2 value is smaller than 0.85, and decided to set a mathematical model as second order polynomial. The R^2 value for second order polynomial model was determined as 0.944946 which represents that there exist 94.5 % relation between the mathematical model (Objective Function) and the experimental data. It is found that the the main effect due to the change of DH is much more than BH, CCF and BS. Secondly, least effective parameter is the BH, besides, the effect value of CCF and BS difference is close to each other.

In optimization stage of the present study, defining the minimum thinning percentage was aimed. As result, the thinning value was minimized and defined as 8,53 which was found in article as 11,61. When these results were compared, the current results show that the optimization study in the present study is succesfull. It is also noted that the obtained optimum results can be experimentally tested in a future study.

Author Statements:

References

[1] Application of FEA in B-Pıllar Reinforcement Forming Simulation. International Journal of Latest Engineering Research and Applications (IJLERA) ISSN: 2455-7137 Volume -02, Issue -06, June-2017, PP – 86 - 92

[2] https://www.engineering.com/Blogs/tabid/3207/Article ID/143/categoryId/11/Stamping.aspx

[3] Sala G. A numerical and experimental approach to optimise sheet stamping technologies: part II – aluminium alloys rubber-forming. Mater Des 2001; 22: 299 – 315

[4] Kim H, Sung JH, Sivakumar R, Altan T. Evaluation of stamping lubricants using the deep drawing test. Int J Mach Tools Manuf 2007; 47: 2120 – 32

[5] El Sherbiny M, Zein H, Abd-Rabou M, El shazly M. Thinning and residual stresses of sheet metal in the deep drawing process. Mater Des 2014; 55: 869 – 79

[6] Chen L, Yang JC, Zhang LW, Yuan SY. Finite element simulation and model optimization of blankholder gap and shell element type in the

stamping of a washing-trough. J Mater Process Technol 2007; 182: 637 – 43

[7] Ghouati O, Gelin J-C, Lenoir H. Process optimizati- on in deep drawing. Rev Eur Des Elem Finish 2000;9:129–49.

[8] https://www.esict.com/

[9] Badgujar T. Y., Wani V. P. Optimization of Stamp- ing Process Parameters for Material Thinning With Design of Experiment Approach. IV Int. Conf. Prod. Ind. Eng. CPIE-2016, 2016,p. 1–9.

[10] Tushar Y. Badgujara, Vijay P. Wani Stamping Process Parameter Optimization with Multiple Regression Analysis Approach Materials Today: Proceedings 2018; 5:4498 - 4507

[11] Kakandikar GM, Nandedkar VM. Prediction and optimization of thinning in automotive sealing cover using Genetic Algorithm. J. Comput Design Eng 2016; 3:63 -70

[12] Colgan M, Monaghan J. Deep drawing process: Analysis and experiment. J Mater Process Technol 2003;132:35–41.

[13] Gunnarsson L, Schedin E. Improving the properties of exterior body panels in automobiles using variable blank holder force. J Mater, Process Technol 2001;114:168–73.

[14] Jawad WK, Mohamed JH. Studying the Effect of Punch Nose Radius on Deep Drawing Operation. Eng Tech 2008;26:55–73.

[15] Thiruvarudchelvan, S., Lewis, W. G. Deep Drawing With Blank Holder Force Approximately Proportional to the Punch Force. J Eng Ind 1990;112:278.

[16] Wang Y, Huang G, Lıu D, Chen L, Han T, Peng J, et al. Influence of blank holder type on drawability of 5182-O aluminum sheet at room temperature. Trans Nonferrous Met Soc China 2016;26:1251–8.

[17] Candra S, Batan IML, Berata W, Pramono AS. Analytical Study and FEM Simulation of the Maximum Varying Blank Holder Force to Prevent Cracking on Cylindrical Cup Deep Drawing. Procedia CIRP 2015;26:548–53.

[18] Zein H, El-Sherbiny M, Abd-Rabou M, El Shazly M. Effect of Die Design Parameters on Thinning of Sheet Metal in the Deep Drawing Process. Am J Mech Eng 2013;1:20–9.

[19] Sun G, Li G, Gong Z, He G, Li Q. Radial basis functional model for multi-objective sheet metal forming optimization. Eng Optim 2011;43:1351– 66.

[20] http://www.businessdictionary.com/

[21] http://www.analyticsvidhya.com/blog/2015/08/com prehensive-guide-regression/

[22] https://reference.wolfram.com/webMathematica/tut orial/Overview.html

ResearchArticle

Comparison of Mechanical Properties of Gypsum with and without Polypropylene Fibers

Xheneta ZENGO[1], Bashkim ZIBERI[2], Naim SYLA[3]

[1]Faculty of Natural Sciences and Mathematics, University in Tetovo, Ilinden str. n.n., 1200 Tetovo, North Macedonia
zengoxh@gmail.com – **ORCID:** 0000-0001-6122-0929

[2]Faculty of Natural Sciences and Mathematics, University in Tetovo, Ilinden str. n.n., 1200 Tetovo, North Macedonia
bashkim.ziberi@unite.edu.mk – **ORCID:** 0000-0001-9786-2595

[3]University of Prishtina, Department of Physics, 10000 Prishtina-KOSOVO
* **Corresponding Author** : naim.syla@uni-pr.edu -- **ORCID:** 0000-0003-0857-4685

Abstract:

Gypsum is a mineral belonging to the group of sulfates, i.e., sulfuric acid, which is often found in Earth's crust. In this paper, two main types of gypsum, gypsum α and gypsum β, with different water content were prepared. Samples with and without polypropylene fibers, with different fiber content and different fiber lengths during preparation, produced in a gypsum factory located in the Debar region, North Macedonia, were studied. Physical properties such as density, porosity, water absorption capability and their kinetics, packing factor, hardening and others were examined using different methods. The main goal of this paper was the determination of mechanical properties of gypsum such as the compressive and flexure strength and the module of elasticity of the gypsum prisms. For the determination of elastic properties, the nondestructive method of ultrasound testing was used. In this test, the strength and quality of a prism is assessed by measuring the velocity of an ultrasonic pulse passing through a gypsum structure. This test is conducted by passing a pulse of ultrasonic wave through a prism and by measuring the time taken by the pulse to get through the structure. Higher velocities indicate good quality and continuity of the material, while slower velocities may indicate gypsum with many cracks or voids. The comparison of the obtained results from these two types of gypsum shows different mechanical and other physical properties.

1. Introduction

Gypsum is a mineral belonging to the group of sulfates, i.e., sulfuric acid, which is often found in the earth's crust. The gypsum chemical name is calcium sulfate dihydrate ($CaSO_4 \times 2H_2O$). In this paper, two main types hemihydrates, hemihydrate α and β, with three different water contents during preparation, were prepared and studied in the shape of prisms. The hemihydrate (HH) is a crystalline hydrate containing one molecule of water for every two molecules of the compound in question.

These hemihydrates are reinforced to see if the properties of the gypsum change, aiming to obtain a much stronger material than gypsum itself. The polypropylene fibers used to reinforce the gypsum were 4,6,8 mm long and 18 micrometers thick. The mass of fibers used is 0.5 %, 1 % and 1.5 % fibers of the mass of gypsum.[1][2][3]

Gypsum panels and blocks represent a good economical method for the manufacture' of partitions and walls, since the raw material cost as well as the labor cost are cheap, besides the ease of decoration. Their main drawbacks are the high-water permeability and their poor mechanical strength. In the present paper, polypropylene (PP) fibers were blended with plaster in an attempt to improve the properties of these products. It was found that the addition of PP fibers reduces the

porosity, decreases the setting time and enhances the mechanical strength.

2. Method

Measurements were performed with prisms whose dimensions were 40 mm × 40 mm × 160 mm. The prisms without fibers are constructed by mixing grinded gypsum who is calcined and turned into a hemihydrate, the grinded gypsum and a percentage of water, 40% for α and 60% for β hemihydrate, are mixed together to form a homogeneous mass. For the samples that are reinforced with polypropylene fibers, the same mass if formed, with the same water factor, but now a percentage of fibers is going to be mixed into the mass. The percentage used is 0.5, 1 and 1.5% fibers of the mass of the gypsum. After the homogeneous mass is formed a mold in the same dimensions are filled with it, it is left to harden for 30 minutes, then the samples are ready to get out of the mold and to be left to dry for 24 hours in 40 °C.The samples dried for 24 hours are tested in flexure, compression, ultrasound pulse velocity test, porosity etc.

Flexing:the method of placing the prism on three supporting points distanced equally from the center of the prism and the bending is going to occur on the center of the prism by pressing it until the prism reaches the maximal breaking point. The speed used is 0.5 m/s. The unit of the force needed to break the prisms is in kN, while its tension in the scale of MPa or in N/mm^2.

Compression:presents the method of placing the prism between two parallel plates and pressing it with a force until it brakes. The unit of force for breaking the prism is in kN, and the tension needed for breaking the prisms has values in MPa or N/mm^2.

The porosity:done when the prisms are completely dry, they are placed in a container with water covering completely the prismsfor 60 minutes, after they are removed, the water from the surface gets dried. The mass of each prism is taken. With the masses of the dry and the wet prisms it can be determined the porosity by using equation 1

$$P = \frac{V_p}{V} \cdot 100\% = \frac{(m_d - m_w)/\rho}{V} \cdot 100\% \quad (1)$$

Ultrasound pulse velocity test: In this test, the strength and quality of a prism is assessed by measuring the velocity of anultrasonic pulse passing through a gypsum structure. This test is conducted by passing a pulse of ultrasonic wave through prism to be tested and measuring the time taken by pulse to get through the structure. Higher velocities indicate good quality and continuity of

the material, while slower velocities may indicate gypsum with many cracks or voids. Through this test the modulus of elasticity is determined using equation 2 [4][5]

$$E = v^2 \cdot \rho \quad (2)$$

3. Results

From the experiments that were performed, the results were quite unexpectable. The porosity results obtained with the samples that contain 0% and 1% fibres that are 8 mm long, tested in both hemihydrates (HH) with three different water factors for both of them.

Table 1. *Change in porosity for the samples with and without fibers*

HH	Wf	0% fibers	1% fibers
α	0.40	22.64	22.65
	0.425	24.02	24.03
	0.45	25.87	25.87
β	0.60	32.82	33.03
	0.625	33.29	33.24
	0.65	34.81	34.81

As it can be seen, the porosity doesn't change even though fibres are added in the mixture (Table 1). That means that the gypsum can be used again in the same places as before, without absorbing more water, without loosing its function and purpose.

By the results in Table 2, it can be said that the longitudinal module of elasticity changes as we add fibres, but not uniformly. As the fibre percentage increases, most of the sample modules decrease, except for β HH which marks 7.05 GPa when 1.5% fibers are added. It can be seen clearly that when we want to increase the module of elasticity, it is worth to use fibers that are 6 mm long. As for the mechanical behavior, when different percentage and different lengths of fibers are added into the mixture, the maximum breaking points change randomly, depending on what fiber works better in a certain HH, or what length resists better in flexure and compression. The maximum breaking point in flexure, it increases when 1.5% fibers 8 mm long are mixed in both α and β hemihydrates. In compression things change, because it is seen that for α HH, 4 mm fibers work better, as for β, 6 mm fibers create a better reinforcement, which mixture doesn't decrease the maximum breaking point. Even though, as it is seen in the tables 3 and 4, the maximum breaking point decreases when fibers are added into the mixture, the graph in Figure 1 shows that the sample gets destroyed after it reaches the maximum breaking point, as for the samples that

have fibers in their content (Figure 2), it cracks after it reaches the maximum breaking point, but it doesn't get destroyed, it needs for about 25 MPa more to detach the fiber connection. [6]

4. Conclusion

Based on the abovementioned results it can be concluded that even though the maximum breaking point decreases when fibres are added into the mixture, the gypsum get reinforced in a strong way even with a small amount of fibres in short lengths. These fibres can help to build much stronger constructions, by using gypsum, which is a very
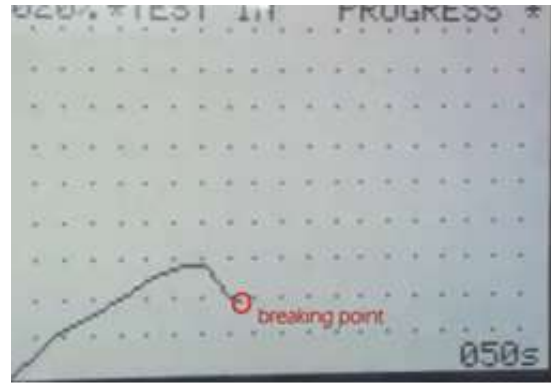
Figure 1. *The sample without fibbers*

economical and cheap solution. Adding fibres in the mixture won't even change the cost, because even PP fibres are cheap, it will cost $10 for preparing 1 ton of prefabricated reinforced gypsum.

Table 2. *Longitudinal module of elasticity for samples with and without fibres*

%of fibers	α HH, Wf=0.40 (GPa)			β HH, Wf=0.60 (GPa)		
	4 mm	6 mm	8 mm	4 mm	6 mm	8 mm
0% fibers	13.85	13.85	13.85	6.95	6.95	6.95
0.5% fibers	12.23	12.75	13.75	6.45	6.99	6.55
1% fibers	11.79	13.15	12.65	6.80	6.77	6.62
1.5% fibers	10.93	12.56	13.06	6.83	7.05	6.32

Table 3. *Maximum breaking point in flexure for samples with and without fibers*

% of fibers	α HH, Wf=0.40 (MPa)			β HH, Wf=0.60 (MPa)		
	4 mm	6 mm	8 mm	4 mm	6 mm	8 mm
0% fibers	9.31	9.31	9.31	5.36	5.36	5.36
0.5% fibers	1.68	7.77	5.26	3.56	0.95	4.23
1% fibers	1.67	6.96	6.49	3.76	0.97	5.51
1.5% fibers	1.95	7.27	10.38	2.92	1.16	6.95

Table 4. *Maximum breaking point in compression for samples with and without fibers*

% of fibers	α HH, Wf=0.40 (MPa)			β HH, Wf=0.60 (MPa)		
	4 mm	6 mm	8 mm	4 mm	6 mm	8 mm
0% fibers	30.33	30.33	30.33	13.63	13.63	13.63
0.5% fibers	29.67	26.48	27.35	11.29	12.97	12.01
1% fibers	27.71	26.22	23.01	10.79	12.77	10.79
1.5% fibers	24.76	23.91	24.10	9.12	12.80	9.95

***Figure 2.** The sample with fibers*

Author Statements:

- The authors declare that they have equal right on this paper.
- The authors declare that they have no known competing financial interests or personal relationships that could have appeared to influence the work reported in this paper
- The authors declare that they have nobody or no-company to acknowledge.

References

[1]. F. E. S. S. L. L. P. J. Nilsson M, "Characterization of a novel calcium phosphate/sulphate bone cement," Journal of biomedical materials research , 2002

[2]. J. A. D. M. Gladis Camarini, "Gypsum hemihydrate-cement lends to improve renderings durability," Construction and Building Materials 25, 2011.

[3]. D. POWELL, "The α- and β-Forms of Calcium Sulphate Hemihydrate," Nature , pp. 185, 375–376, 1960.

[4]. D. Ensiminger, Ultrasonic: fundamentals, technology, application, New York: Marcel Dekker, INC., 1988

[5]. K. Krautkramer, "Ultrasonic Testing of Materials," Springer-Verlag, 1969.

[6]. J. S. a. C. A. K.K. Kelley, Thermodynamic Properties of Gypsum and its Dehydration Products, Washington: Pp. iv. 73, 1941

Research Article

On the Mechanical Behavior of Distinct Auto Wheel Materials Under Static and Dynamic In-service Loading Cycle

Aniekan Essienubong IKPE[1*], Emem Okon IKPE[2], Ekom Mike ETUK[3]

[1]Department of Mechanical Engineering, University of Benin, PMB. 1154 Benin City, Nigeria
* **Corresponding Author** : aniekan.ikpe@eng.uniben.edu --**ORCID:** 0000-0001-9069-9676

[2]Department of Science Technology, Akwa Ibom State Polytechnic, Ikot Osurua, PMB 1200, Nigeria
ememohi83@yahoo.com --**ORCID:** 0000-0001-8093-9904

[3]Department of Production Engineering, University of Benin, PMB. 1154 Benin City, Nigeria
alwaysetuk@gmail.com --**ORCID:** 0000-0002-1866-9349

Abstract:

Automobile wheels serve as a primary means of support to a moving and stationary car while being subjected to static and dynamic loading in the process. The present study examines the mechanical behavior of different auto wheel materials under the aforementioned loading conditions using Finite Element Method (FEM). The wheel component was modlled and simulated with SOLIDWORKS 2018 version using different materials including carbon fibre (T300), cast alloy steel, aluminium (2014-T6) and magnesium alloy. Considering the simulation constraints of lowest static stress (von-mises), lowest resultant strain, lowest displacement (static and raidal) and lowest bending, cast alloy steel met all the requirements except for static strain where carbon fibre was the lowest followed by cast alloy steel. Carbon fibre (T300) among all the materials had the highest static stress (von-mises), highest displacement (static and raidal) and highest bending. Static stress for aluminium (2014-T6) was lower than that of magnesium alloy while resultant strain, static and radial displacement as well as bending were lower for aluminium (2014-T6) than magnesium alloy. Von-mises stresses for all wheel materials where below their yield strength, indicating that they can perform optimally under the above mentioned loading constraints. The main disadvantage with steel wheel is the high density while low density of the other three materials offer a distinctive advantage to auto performance, but steel wheel is inexpensive, strong, tough and more durable compared to the other materials.

1. Introduction

A wheel is a circular-shaped structure designed with extreme toughness and high strength to withstand radial, tangential and axial forces it is exposed to when subjected to rotational motion. The centre of the wheel is bored of a circular hole were an axle bearing is tightened about to enable the wheel rotate when a moment generated by the auto engine is applied to the vehicle axle about its axis and the wheel [1]. In other words, the wheel is one of the most important rotating circular member of a vehicle, upon which the tyre is installed in between the flange at a pressure (35-40 Psi) different from the ambient pressure [2, 3]. Automobile wheel assembly is one of the most important aspects that determine mobility in automotive applications and its failure can be hazardous if not properly engineered to bring out the best performance, strength, durability and reliability. The design of a wheel assembly is critical

due to the forces acting on it during acceleration, braking, cornering and tilting [4]. Weight, manufacturability, performance and aestetics are the four essential technical factors considered in the design of auto wheel. It is usually designed to possess adequate strength to enable it perform the desired functions, should be balanced statically and dynamically as well, and should be produced from very light materials to reduce unsprung weight. Steel wheels are comparably stronger than wire and alloy wheels, but it is heavier than alloy wheels which increases the vehicle unsprung weight. On the other hand, alloy wheels are recommended for automobile applications because they reduce unsprung weight of the vehicle [5, 6]. Bisht and Awasthi [7] reported the percentage weight of different wheel types as follows: Steel wheel (100%), Wire wheel (85%), alloy wheel (75%) and composite wheel (60%). Nomenclature of a wheel-rim profile consist of the wheel (rim and disc forms wheel), Rim (a section of wheel that the tyre is installed), disc (a section of the wheel attached to the axle hub of the vehicle) as well as the bead seat (a section of the rim that holds the tyre in a radial direction and in contact with the bead face) [8, 9]. Depending on the purpose of design, loading conditions and material capacity to withstand severe loading conditions, automobile wheels can be classified. For example, heavy loading may require steel wheels (density: 7.8 g/cc) due to their strength while medium and low load condition may require aluminium alloys (density: 2.7 g/cc) and magnesium alloys (Density: 1.54 g/cc) [10]. Prasad et al. [11] employed CATIA 5R17 software in the modelling of aluminium alloy and forged steel wheel rims which were further imported to ANSYS software to simulate the forces, pressure (21.3kpa was applied along the circumference of each wheel rim) acting on them and their effects on the wheel rim. Static displacement, Von-mises stress, stress intensity and dynamic displacement were 4.1168e-6mm, 9.748e5 Mpa, 1.0611e6 Mpa and 0.71537 mm as well as 4.077e-6 mm, 3.2348e6 Mpa, 3.3759e6 Mpa and 0.43427 mm for aluminium alloy and forged steel wheel rims, making forged steel a better material for wheel design over aluminium alloy. Venkateswarlu and Sharma [12] designed and analysed three different alloy wheel materials including aluminium alloy, magnesium alloy and titanium alloy. The wheel was modelled with CATIA V5 R20 while simulation of the model was carried out with ANSYS workbench. Total deformation values obtained from the static analysis were 0.13156, 0.13505 and 0.16258 for aluminium alloy, magnesium alloy and titanium alloy. This indicates that aluminium alloy among the three materials will exhibit the least level of deformation under static condition. Kumar et al. [13] carried out similar study on different alloy wheel materials (aluminium alloy, steel and magnesium alloy) using CATIA V5 for the modelling and ANSYS software for the simulation. Steel wheel exhibited the least level of deformation (0.00029 mm), followed by magnesium alloy (0.00072 mm) and aluminium alloy (0.001287 mm). Using ANSYS software, Burande and Kazi [14] modelled and simulated two aluminium alloy wheels (Aluminium A356.2 and Aluminium 7075-T6) for passenger car under radial load. Finite Element Analysis (FEA) was used in the simulation to determine the stress and displacement factors in service condition. Aluminium A356.2 yielded Von-mises stress of 43.95 MPa and displacement of 32.33 mm while Aluminium 7075-T6 yielded Von-mises stress of 35.75 MPa and displacement of 23.81 mm. The analysis indicated that Aluminium 7075-T6 has a higher fatigue life ($1x10^6$ cycles.) than aluminium A356.2 ($7.9985x10^5$ cycles). Sekhar and Mouli [15] examined the application of Finite Element Technique (FET) for analysing the stress and displacement distribution in AL2024-T351 and Al 2064-T6 alloy wheels under conjoint influence of inflation pressure and radial load. The deflection for AL2024-T351 alloy wheel was found to be 0.164 mm which is much lower than that of aluminum (Al 2064-T6) alloy wheel which was 0.285mm, indicating that AL2024-T351 is much stiffer than aluminum (Al 2064-T6) alloy wheel. Results from the static analysis revealed that maximum normal stress obtained from Al 2064-T6 alloy wheel was 78.6% higher than that of Al2024-T351 alloy wheel while the Von-mises stress obtained for Al 2064-T6 alloy wheel was 50% higher than that of Al2024-T351 alloy wheel. It was observed that the stress and displacement increased while the in-service life of the wheel decreased as the operational speed increased. In actual case scenario, determining the mechanical behaviour of auto wheels (as per the ISO 7141-Road Vehicles-Wheels-Impact Test Procedure, and SAE J175-Impact Test Procedure Standards) is important. However, testing and inspection procedure during development process of auto wheels are time consuming and expensive. Moreover, it is difficult to estimate the stress behaviour through theoretical approaches and elementary mechanical approximations. For these reasons, a 3D static analysis of any given auto wheel which involves complicated geometries and assumptions can be employed. The present study therefore involves determination of stresses, strains, displacements as well as bending induced on different auto wheel materials (designed with different materials) due to static and dynamic loads. The study involves Finite Element Modelling (FEM) of the auto wheel using SOLIDWORKS 2018 version and simulation of the

modelled component as well, in order to determine the mechanical behaviour of each material for auto wheel applications. For economic reasons, this can reduce the time, energy and resources involved in the development of prototype designs and testing phase of auto wheel.

2. Research Methodology

A given automotive wheel in motion is subjected to the following forces and moments: longitudinal force, lateral force (cornering force), vertical force (load), roll moment (overturning moment), pitch moment, yaw moment [16]. A given rotating vehicle wheel is subjected to radial loading due to pressure distribution which acts directly in the circumferential direction along the bead seat [17]. The pressure distribution is given by Equation 1. From Equation 1, radial load acting on a given car wheel can be determined using Equation 2:

$$W_r = W_0 * cos\left(\frac{\pi}{2} * \frac{\theta}{\theta_0}\right) \tag{1a}$$

$$W_0 = \frac{W\pi}{b r_b 4\theta_0} \tag{1b}$$

$$F_r = 2b\int_{-\theta_0}^{\theta_0} W_n * r_b d\theta = 8*b*r_b*\theta_0*\frac{W_n}{\pi} \tag{2}$$

Where W_n is the natural frequency, W denotes the radial load, θ is the angle of loading, θ_0 is the angle at maximum load, F_r is the radial force, b is the width of the bead seat, r_b is the radius of the bead seat and W_r represents the pressure distribution. The wheel rolling radius can be determined as expressed in Equation 3 based on the relationship between the wheelset, wheel rotation and the formation of the traction force [18, 19]. On the other hand, Jazar [20] proposed the wheel rolling radius as expressed in Equation 4 while Wilson et al. [21] proposed the wheel rolling radius based on the function of drive torque, load, and pressure as given in Equation 5.

$$R_D = R_u - \rho_o\left[D arctan\left(B\frac{\rho}{\rho_o}\right) + E\frac{\rho}{\rho_o}\right] \tag{3}$$

$$R_D = \frac{2}{3}R_u + \frac{1}{2}R_l \tag{4}$$

$$R_D = R_u - \lambda^*\left[1 - \left(1 - \frac{w}{W^*}\right)P/P^*\right]T \tag{5}$$

Were R_D is the actual rolling radius of the wheel, R_u is the radius of the wheel without load, R_l is the radius of the loaded wheel, ρ is the actual deflection of the tire, ρ_o is the deflection of the tire at rated load, B, D, E are the design parameters of the tire, W is the vertical load on the wheel, T is the torque applied to the wheel, λ^*, W^* and P^* are the empirical factors of the tire longitudinal elasticity, load, and pressure. Studies have shown that wheel deformation contributes immensely to wheel slipping which is a

measure of the difference between rotational speed of the wheel and the translational velocity of the wheel centre as expressed in Equation 6 [22] or determined as the difference between the arc lengths in Equation 7. The actual radius (R_A) of a deformed wheel is determined using Equation 8 while the relation for coefficient of slippage [23] is given by Equation 9.

$$S = -\frac{(V-R_e w)}{V} \tag{6}$$

$$\delta_G = \frac{2\pi}{\alpha}\left(\frac{\left(\alpha R - 2R\,sin\frac{\alpha}{2}\right)}{\alpha R}\right) = \left(1 - \frac{2}{\alpha}sin\frac{\alpha}{2}\right) = \left(1 - \frac{L}{\alpha R}\right) = \left(1 - \frac{R_D}{R}\right) \tag{7}$$

$$R_A = \frac{L}{\alpha} = \frac{L}{2\,arc\,sin\frac{L}{2R}} \tag{8}$$

$$\delta = \frac{\omega R_K - V_D}{\omega R_K} = \frac{2\pi R_K n - S_D}{2\pi R_K n} \tag{9}$$

Where V is the longitudinal speed of the wheel centre, w is the angular speed of the tire and Re is the effective tire radius, δ is the coefficient slipping, V_D is the actual speed, ω is the angular velocity of the drive wheel, R_K is the driving wheel rolling radius, n is the number of turns made by the wheel per unit of time, S_D is the actual distance covered by the wheel for a certain number of the wheel turns, δ_G is the wheel slipping, R is the initial radius of the wheel rolling, α is the central angle limiting the chord of the wheel tire deflection, L is the length of the chord formed by the deflection of the wheel. Initial radius of the wheel is given by Equation 10 while the change in radius of the wheel caused by the load of its own weight is given by Equation 11. The stiffness of the wheel material (Equation 12) if optimum can resist changes in the radius of the wheel [24].

$$R = R_C - \Delta r = \frac{l_C}{2\pi} - \frac{(l_C - l_K)k_{DP}}{2\pi} = \frac{l_C(1 - k_{DP}) + l_K k_{DP}}{2\pi} \tag{10}$$

$$\Delta r = \frac{(l_C - l_K)k_{DP}}{2\pi} \tag{11}$$

$$k_{wheel} = (2*\pi*f_2)^2\left[M_T - M_T\left(\frac{f_2^2}{f_1^2}\right)\right] \tag{12}$$

Where f_1 is the Maximum frequency in harmonic response, f_1 is the minimum frequency in harmonic response, M_T is the mass of the wheel, R_C is the radius of the middle of the wheel tread in the Free State. Axial load (F_p) resulting from tire inflation pressure (P_o) is given by Equation 13 while the load on a unit length of the circumference of the rim flange of the rotating wheel is given by Equation 14.

$$F_p = \pi(a^2 - r_f^2)P_o \tag{13}$$

$$T_f = \frac{F_P}{4\pi * r_f} = (a^2 - r_f^2)\frac{P_o}{4*r_f} \tag{14}$$

where *a* is the design radius of the tire and r_f is the radius of the loading point on the rim flange. When the vehicle is in motion, causing the wheels to undergo a rotary motion (O) at angular velocity (Ω_Z), the velocities at the axial centre of the right front wheel (O_l) are given by Equations 15a-b [25]. The slip velocities of the projection point (O_l) on the wheel-ground contact surface is given by Equations 16a-b.

$$V_{o1} = R^{"}\Omega_z = \sqrt{\left(R^{"} + \frac{B}{2}\right)^2 + \left(\frac{L}{2} - S_o + C_y\right)^2}\,\Omega_z \quad (15a)$$

$$V_{o1x1} = R^{"}\Omega_z \sin\alpha = \left(\frac{L}{2} - S_o + C_y\right) \quad (15b)$$

$$V_{t_1x_1} = \left(R^{"} + \frac{B}{2}\right)\Omega_z - r\omega_o \quad (16a)$$

$$V_{t_1x_1} = \left(\frac{L}{2} - S_o + C_y\right)\Omega_z \quad (16b)$$

Were the rotational angular velocity of the right wheel denoted as ω_o. The expression describing the dynamics of the angular deformation of the wheel is given by Equation 17.

$$H_\alpha \frac{d\Delta\alpha}{dt} + C_\alpha \Delta\alpha = M(\lambda) \quad (17)$$

where H_α is the energy dissipation rate of the angular deformational motion in a wheel, C_a is the angular rigidity of the wheel in the direction of the angular deformation movement therein. The angular speed of rotation and speed of translational movement of the centre of wheel mass is given by Equation 18 while The change of moment $M(\omega,V)$ of the traction point is given by Equation 19 [26]. Furthermore, the stress induced on auto wheel due to bending is given by Equation 20.

$$\Delta\alpha = \int_{t-\Delta t}^{t}[\omega(r_o - x_1) - V]dt \quad (18)$$

$$M(\omega,V) = C_\alpha \int_{t-\Delta t}^{t}\left\{\omega - V/\left[r_o - \frac{P}{\left(C_o + C_\omega\left(1 - e^{-K\omega\omega}\right)\right)}\right]\right\}dt \quad (19)$$

$$\sigma_b = \frac{M_y}{I_c} \quad (20)$$

where C_o is the value of the radial stiffness of the wheel in rest, $C\omega$ is the coefficient characterizing the impact of centripetal force on radial stiffness of the wheel, $K\omega$ is the coefficient characterizing the nonlinear effect of the angular speed of the wheel on its radial stiffness, P is weight of the vehicle and the wheel which influence the contact patch, V is the velocity of translational motion of the centre of the wheel mass and ω_o is the angular velocity of the wheel, M is the bending moment, y is the distance between the centroidal axis and the outer surface of

the wheel and I_c is the centroidal moment of inertia of the of the cross section about the appropriate axis.

SOLIDWORKS software, 2018 version was employed in modelling and simulating the auto wheel component presented in Figure 1. SOLIDWORKS is a solid modelling Computer Aided Design (CAD) software as well as Computer Aided Engineering (CAE) tool that runs mainly on Microsoft windows. Modelling procedure of the auto wheel commenced with 2D sketch, consisting of geometries such as arcs, points, conics, lines, splines and so on. Dimensions were added to the sketch to define the size and configuration of the geometry. Relations in the tool bar were used to define features such as parallelism, tangency, concentricity, perpendicularity among others. In the part assembly, sketches of individual parts were assembled together to form the intended solid model of the auto wheel. Views were automatically generated from the solid model; and dimensions and tolerances were added to the drawing as required. SOLIDWORKS software have been successfully employed in modelling of reciprocating piston [27], remotely controlled hydraulic Bottle Jack [28], vehicle compression springs [29], two stroke internal combustion engine [30], High Density Polyethylene Liner HDPL [31] etc. The wheel was analysed for static and dynamic loads. In the case, pressure loading, centrifugal/radial loading and vertical loading were considered. Von-mises stress, equivalent strain, resultant displacement and bending obtained from the analysis shows the maximum and minimum values induced on the auto wheel operating under the aforementioned loading conditions. The wheel was constrained appropriately and the loads were calculated based on the specifications and applied to appropriate nodes. The wheel was analysed for the calculated loading conditions and plots were obtained for each analysis performed. To fully initiate the auto wheel simulation process, the following conditions were taken cognizance of:

i. There was a fixed support on the six bolt/stud holes, as wheels are normally installed by bolt via stud holes in vehicle axle.
ii. A total of 7769.5 N bearing load was applied to the hub centre at Y-axis, as the hub is fixed at the central hole of the rim.
iii. A pressure of 0.241 Mpa was considered on the tyre allocation area which acts normally at the circumferential tread and flange portion of the wheel.
iv. Considering a tyre diameter of 550 mm, velocity of car rim was taken as 100 kmph, i.e. 965 RPM.

v.   From annexure of AIS-073 (part 2), the moment taken was 5.0969e+5 N-mm.

Figure 1 represents the auto wheel model while Figure 2 represents the mesh visualization for each material of the auto wheel model. Material properties of the auto wheel are presented in Table 1, load details for the auto wheel analysis in Table 2, fixture details for the auto wheel analysis in Table 3 and mesh information in Table 4.

3. Results and Discussion

3.1. Carbon Fibre (T300)

Carbon fibre is a fibre material of about 5-10 micrometres in diameter and is composed primarily of carbon atoms. Carbon fibre is manufactured through the process of high bonding of carbon atoms together in crystals which are more aligned to the long axis which gives the fibre a high strength to volume ratio. It has numerous advantages such as high tensile strength, high temperature tolerance, low weight, high stiffness, low thermal expansion etc. which makes carbon fibre an essential material

in the manufacturing of automotive wheel. However, it is very expensive, brittle and prone to the risk of catastrophic failure that cannot be experienced with metallic wheels. The T300 carbon fibre is a thermoset polymer matrix composite reinforced with 68% carbon fibre, and formed by laminating hot-pressed carbon fibre prepreg. Having developed the auto wheel model presented earlier in Figure 1, T300 carbon fibre was applied as the wheel material and simulated to obtain multiple profiles as shown in Figure 3a-f.
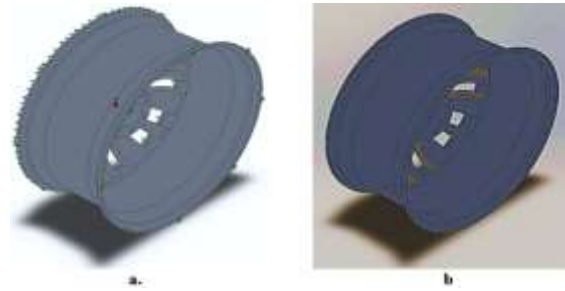
Figure 1. *Auto wheel model analysed in this study*

Table 1. *Material properties of auto wheel (model)*

Name	Carbon fiber (T300)	Cast Alloy Steel	Aluminium (2014-T6)	Magnesium Alloy
Model type	Linear Elastic Isotropic	Linear Elastic Isotropic	Linear Elastic Isotropic	Linear Elastic Isotropic
Yield strength	3.44e+008 N/m²	4.41e+008 N/m²	4.15e+008 N/m²	6.24+008 N/m²
Tensile strength	1.86e+009 N/m²	4.48e+008 N/m²	4.7e+008 N/m²	4.48e+008 N/m²
Elastic modulus	1.35e+011 N/m²	1.9e+011 N/m²	7.24e+010 N/m²	4.5e+010 N/m²
Poisson's ratio	0.3	0.26	0.33	0.35
Mass density	1700 kg/m³	7300 kg/m³	2800 kg/m³	1760 kg/m³
Shear modulus	9.8e+007 N/m²	7.8e+010 N/m²	2.8e+010 N/m²	1.7e+010 N/m²
Thermal expansion coefficient	1.5e-005 /Kelvin	1.5e-005 /Kelvin	2.3e-005 /Kelvin	2.5e-005 /Kelvin

Table 2. *Load details for the auto wheel analysis*

Load name	Load Image	Load Details	
Pressure-1		Entities	9 face(s)
		Type	Normal to selected face
		Value	255.692
		Units	N/m²
		Phase Angle	0
		Units	deg
Gravity-1		Reference	Top Plane
		Values	0 0 -9.81
		Units	m/s²

***Table 3.** Fixture details for the auto wheel analysis*

Fixture name	Fixture Image	Fixture Details		
Fixed Hinge-2		Entities	6 face(s)	
		Type	Fixed Hinge	
		Resultant Forces		
Components		X	Y	Z	Resultant
Reaction force(N)		2.88696	22.2569	0.028139	22.4434
Reaction Moment (N.m)		0	0	0	0
Fixed-1		Entities	2 face(s)	
		Type	Fixed Geometry	
		Resultant Forces		
Components		X	Y	Z	Resultant
Reaction force (N)		-2.88833	42.2323	-0.0292426	42.331
Reaction Moment (N.m)		0	0	0	0

***Table 4.** Mesh information for the auto wheel analysis*

Mesh details for the wheel rim analysis		Specification of proposed car wheel rim	
Mesh type	Solid Mesh	Specification	Value
Mesher Used	Blended curvature-based mesh	Bolt circle diameter	68 mm
Jacobian points	4 Points	Width of the rim	140 mm
Maximum element size	26.4766 mm	Diameter of the rim	355 mm
Minimum element size	5.29532 mm	Offset	57 mm
Mesh Quality Plot	High	Central hole diameter	40 mm
Total Nodes	56016	Rim thickness	7 mm
Total Elements	31880	Hole circle diameter	15 mm
Maximum Aspect Ratio	421.11	Number of stud hole	5 No's
% of elements with Aspect Ratio < 3	83		
% of elements with Aspect Ratio > 10	2.58		
% of distorted elements (Jacobian)	0		
Time to complete mesh (hh;mm;ss):	00:02:28		

Carbon fibre (T300)   Cast alloy steel   Aluminium (2014-T6)   Magnesium alloy
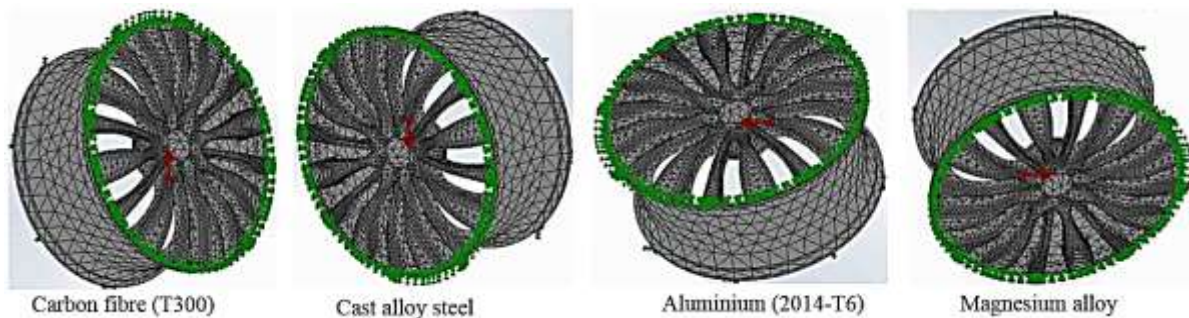
***Figure 2.** Mesh visualization for each material of the auto wheel model*

3.2. Cast alloy steel

Cast steel is a ferrous alloy with maximum carbon content of approximately 0.75% and other elements including silicon, manganese, iron, aluminium, zirconium etc. It has high resistance to impact cracks, high strength, toughness, can withstand abrasion and high loading deformation due to high carbon content and inexpensive compared to carbon fibre, aluminium and magnesium alloy. The aforementioned properties makes it suitable for auto
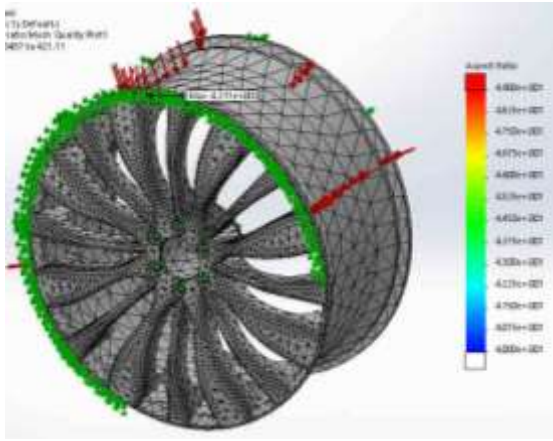
Figure 3a. *Aspect ratio*

Figure 3b. *Static nodal stress*
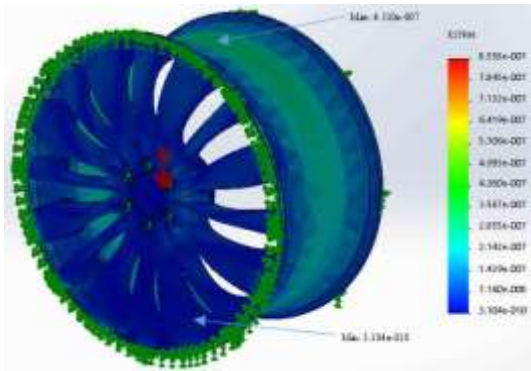
Figure 3c. *Equivalent Static strain*
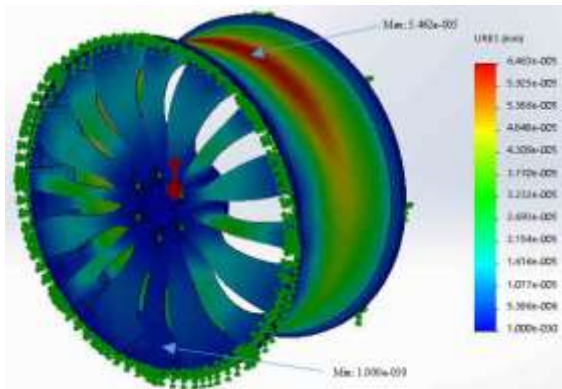
Figure 3d. *Static displacement*

Figure 3e. *Radial displacement*

Figure 3f. *Bending*

Figure 4a. *Aspect ratio*
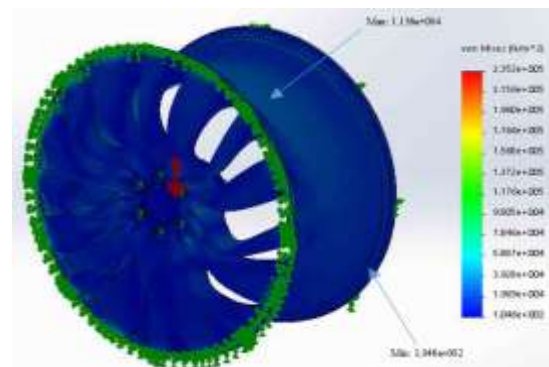
Figure 4b. *Static nodal stress*

67
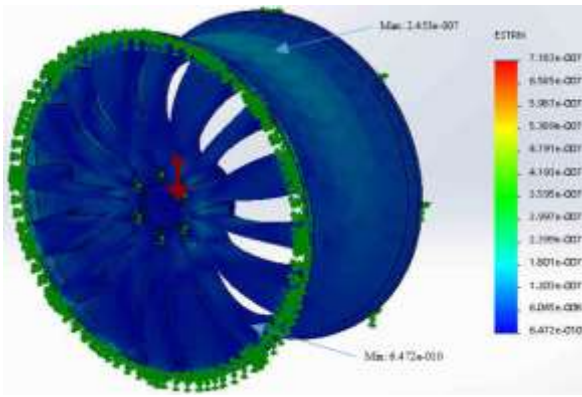
Figure 4c. *Equivalent static strain*
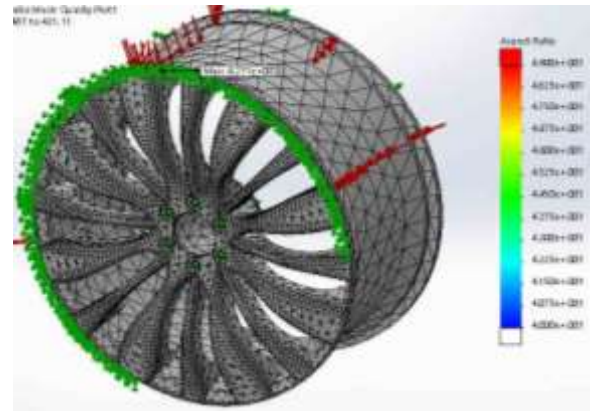
Figure 5a. *Aspect ratio*
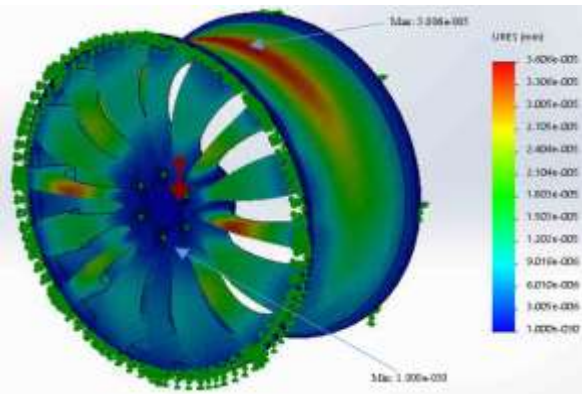
Figure 4d. *Static displacement*
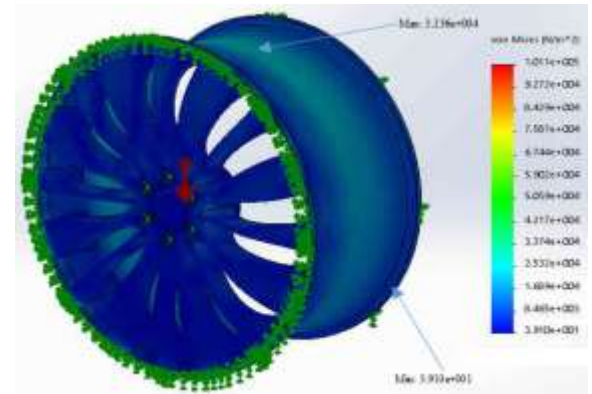
Figure 5b *Static nodal stress*
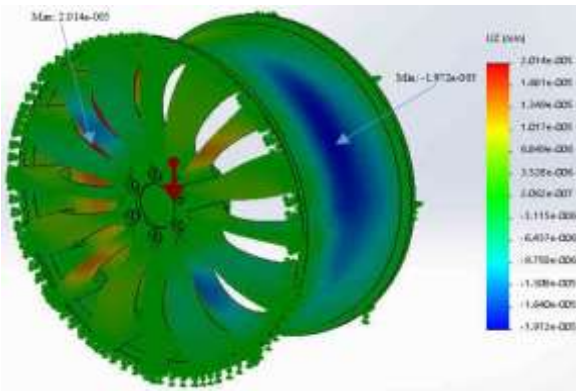
Figure 4e. *Radial displacement*
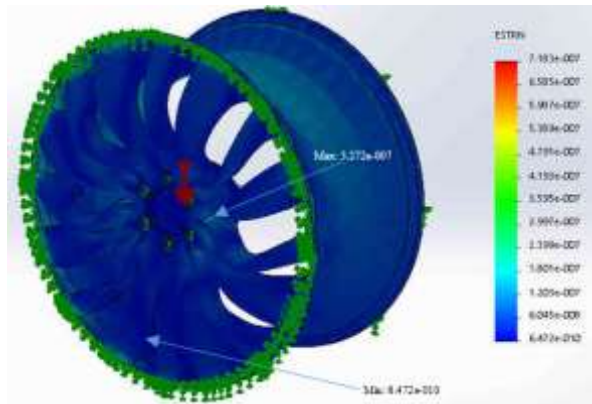
Figure 5c. *Equivalent static strain*
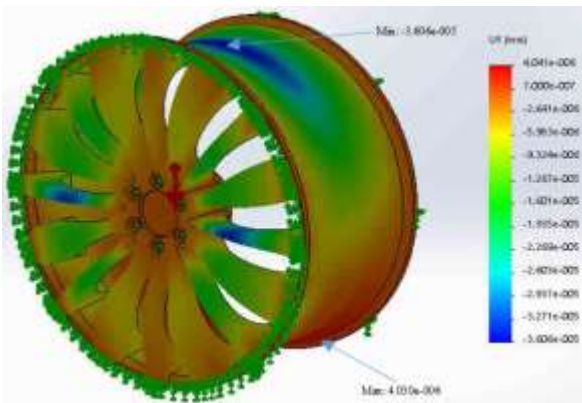
Figure 4f. *Bending*
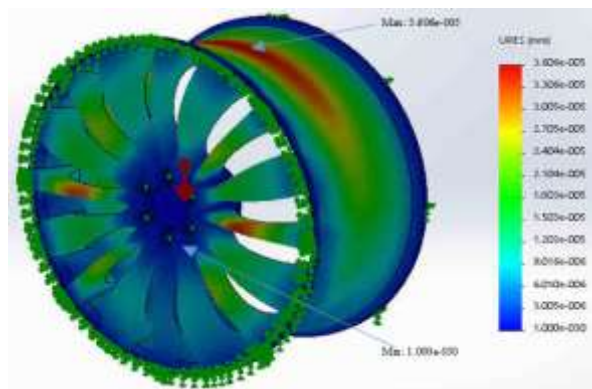
Figure 5d. *Static displacement*
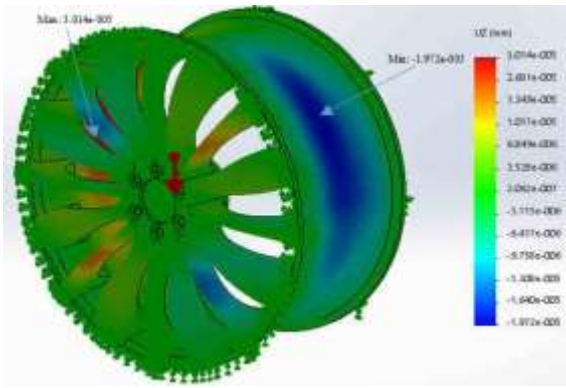
Figure 5e. *Radial displacement*
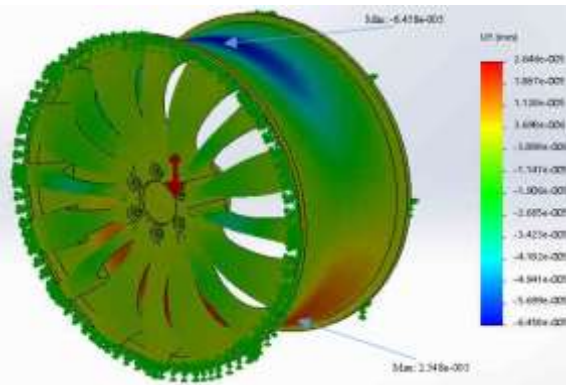
Figure 5f. *Bending*

wheel application but it has a major disadvantage which is the unit weight. Having developed the auto wheel model presented earlier in Figure 1, cast alloy steel was applied as the wheel material and simulated to obtain multiple profiles as shown in Figure 4a-f.

3.3. Aluminium 2014-T6

2014-T6 aluminium is 2014 aluminium in the T6 temper which is achieved by solution heat-treatment and artificial age-hardening treatment to obtain the standard mechanical required. As one of the strongest aluminium alloy, aluminium 2014-T6 is a precipitation hardening alloy with high electrical conductivity, low density, ductile, excellent machinability, cost effective and fair corrosion resistant property. It is used in applications that require high strength/hardness as well as elevated temperature such as auto wheel, heavy duty forgings, tangs, automotive frame etc. However, it contains high amount of copper, making it less corrosion-resistance. Therefore, requires anti-corrosion treatment if exposed to corrosive environment. Having developed the auto wheel model presented earlier in Figure 1, 2014-T6

aluminium was applied as the wheel material and simulated to obtain multiple profiles as shown in Figure 5a-f.

3.4. Magnesium Alloy

Magnesium alloy is known for being the lightest structural alloy. It is formed from a mixture of magnesium (the lightest structural metal) and other metals elements (known as alloying elements) usually manganese, zinc, aluminium, copper, silicon etc. to improve the mechanical properties [32]. Magnesium alloy has a number of merits such as low specific gravity with satisfactory strength, higher specific modulus, withstand greater loading per unit weight, low density which makes it suitable for wheel-rims in automobiles. The strength of magnesium alloy however depreciates at elevated temperature. Therefore, temperature as low as 200 ^{o}F (93 ^{o}C) yields considerable reduction in the yield strength of magnesium alloy [33]. Having developed the auto wheel model presented earlier in Figure 1, magnesium alloy was applied as the wheel material and simulated
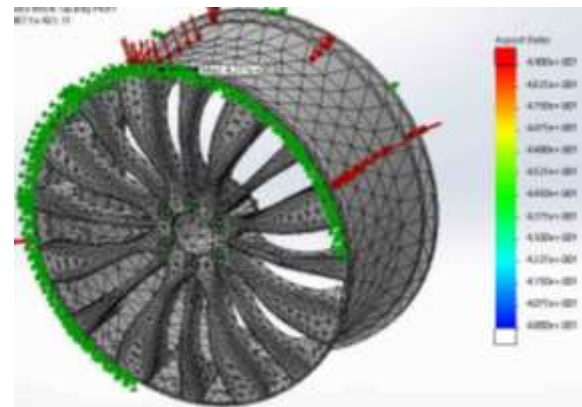
Figure 6a. *Aspect ratio*
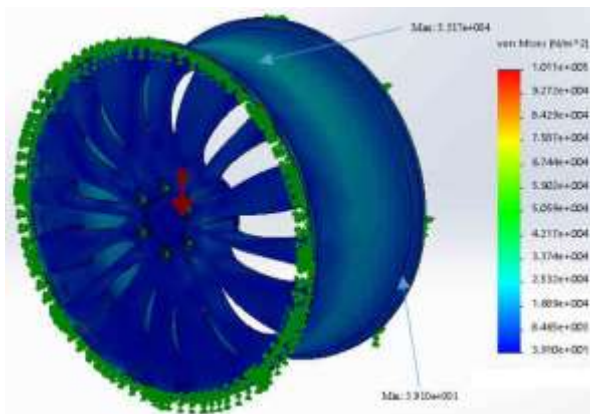
Figure 6b. *Static nodal stress*
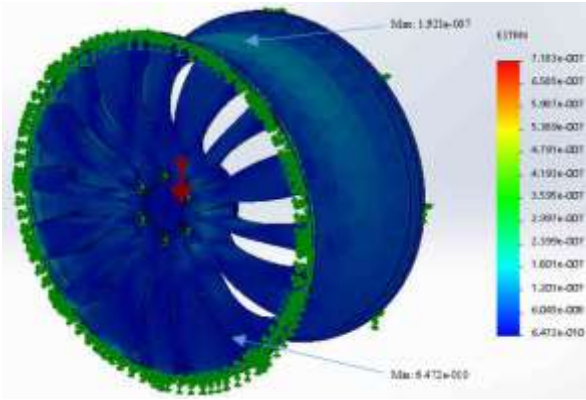
Figure 6c. *Equivalent static strain*
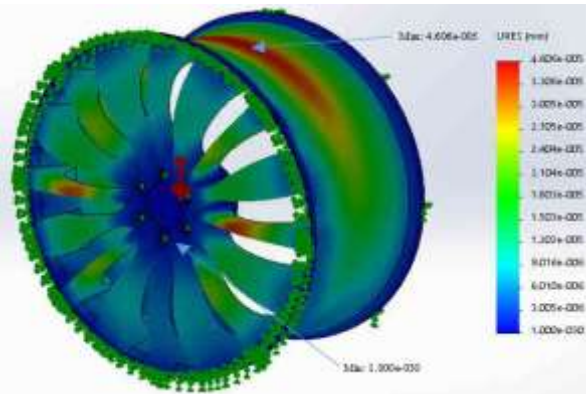
Figure 6d. *Static displacement*
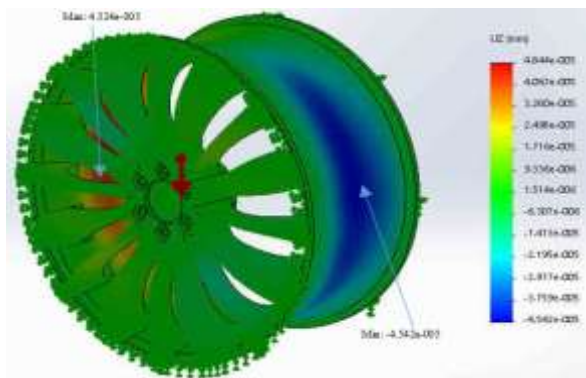
Figure 6e. *Radial displacement*
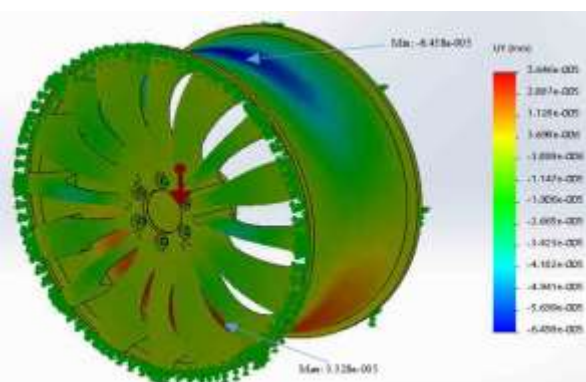
Figure 6f. *Bending*

to obtain multiple profiles as shown in Figure 6a-f. The deflected auto wheel models obtained from the finite element simulation profiles are characterized by different colors corresponding with the simulation results shown on the color bands. Areas with high stress concentration, high resultant displacement, high equivalent strain as well as high bending stress indicates unsafe zones which are prone to high level deformation and vice versa [34, 35], and can be identified using the color band or legend on the simulated plots presented in Figures 3-6. Red color which is at the top of the color band indicates the area with maximum stress, resultant displacement, equivalent strain and bending stress concentration on the auto wheel component. This is followed by orange color, light green color, green color and so on. On the other hand, royal blue which is at the bottom of the color band indicates safe zones as well as the areas with minimum stress concertation on the wheel component. Sky blue indicates the stress level at which the shaft material begins to respond to the applied load, aqua (SVG) blue indicates further stress level from sky blue color [36, 37]. Figure 7 shows the maximum Von-mises stress derived from each of the auto wheel material employed in this study.Results shown on the plot in Figure 7 reveals that carbon fibre (T300) had the highest static nodal stress (5.35E+04 N/m^2), followed by magnesium alloy (4.22E+04 N/m^2), 2014-T6 aluminium alloy (3.14E+04 N/m^2 and then cast alloy steel as the least (1.14E+04 N/m^2). This implies that auto wheel material with maximum static nodal stress will fail first before the one with minimum static nodal stress. Considering von-Mises failure theory, material component is said to be in a state of failure if the von-Mises stress exceeds the material yield strength, but if the von-Mises stress value is lower than the material's yield strength, the material is considered to be safe [38, 39]. Considering the maximum von-Mises stresses and yield strength obtained from each auto wheel simulated profile, it can be observed that the maximum von-mises stress values for the four (4) wheel materials were below their yield strength, indicating that all the for materials in this study considered are good choice of materials that can withstand the in-service loading condition of an auto wheel application without untimely failure. Figure 8 shows the maximum resultant static strain derived from each of the auto wheel material employed in this study.

Results shown on the plots in Figure 8 reveals that magnesium alloy had the highest resultant static strain (3.31E-07), followed by 2014-T6 aluminium alloy (3.17E-07), cast alloy steel (2.45E-07) and then carbon fibre (T300) as the least (1.92E-07). From the

maximum strain obtained from each profile, the values are insignificant, implying that the rate of strain elongation on the auto wheel component due to static and dynamic loads is within tolerable level that will not result in catastrophic failure. The low static resultant strain exhibited by carbon fibre is due to the high stiffness and high tensile strength of the material. Strain is the ratio of change in deformation undergone by an object in response to the applied load or force to its original length [40]. The static or dynamic loads may take the form of compression or stretching which incite stresses within the molecular bonding of the material, causing the atomic bonding to detach from one another. Strain elongation on the wheel can also occur due to thermal expansion coefficient which is the equivalent strain divided by the change in temperature of the wheel in motion. This can cause increase in strain along the bonded area within the atoms in the metal lattice as the auto wheel temperature increases during service condition. Figure 9 shows the maximum static displacement derived from each of the auto wheel material employed in this study.

Results shown on the plot in Figure 9 reveals that carbon fibre (T300) had the highest static displacement (5.46E-05 mm), followed by magnesium alloy (4.61E-05 mm), 2014-T6 aluminium alloy (3.61E-05 mm) and then cast alloy steel as the least (3.01E-05). Figure 10 shows the maximum radial displacement derived from each of the auto wheel material employed in this study. Results shown on the plots reveal that carbon fibre (T300) had the highest static displacement (5.71E-05 mm), followed by magnesium alloy (4.32E-05

mm), 2014-T6 aluminium alloy (3.01E-05 mm) and then cast alloy steel as the least (2.01E-05). Displacement is a vector quantity that refers to the extent at which a body deviates from its original place or length. It is also the overall change in position of an object due to external forces or loads acting on them, which in this case is the static and dynamic loads acting on the auto wheel component. The change in position or deviation from the original length is a property that relates to the geometric distortion or structural deformation of the wheel from its original geometry. Hence, the static and dynamic loads acting on the auto wheel component are responsible for the static and radial displacements discussed in this paper.

Figure 11 shows the maximum bending deformation derived from each of the auto wheel material employed in this study. Results shown on the plot in Figure 11 reveals that carbon fibre (T300) had the highest bending deformation (5.03E-05 mm), followed by magnesium alloy (3.33E-05 mm), 2014-T6 aluminium alloy (2.55E-05 mm) and then cast alloy steel as the least (4.03E-06). Bending deformation also known as flexural stress is a more specific form of normal stress induced on a structurally loaded member like the auto wheel subjected to tensile or compressive forces. In other words, normal stress is a result of an external load acting perpendicularly to longitudinal axis of the wheel component. The exact value of the normal force (curb weight of the car) acting on the wheel component which eventually results in bending deformation is simply the force divided by the cross sectional area of the auto wheel.
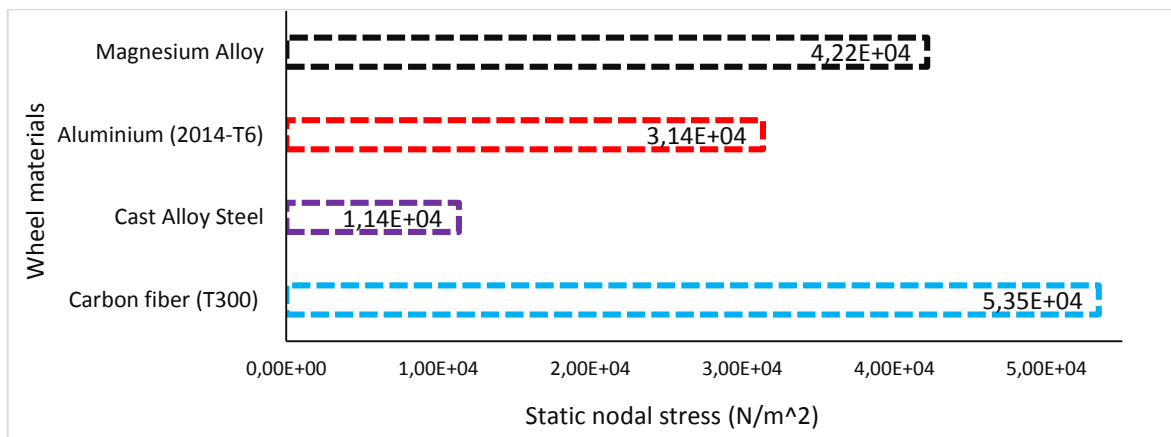
***Figure 7.** Maximum static nodal stress (von-mises) derived from each wheel material*
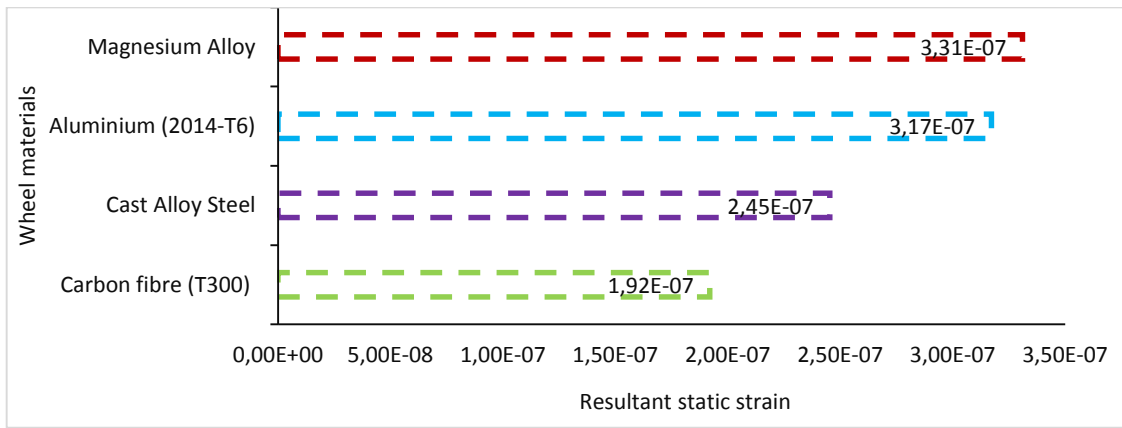
Figure 8. *Maximum resultant static strain derived from each wheel material*
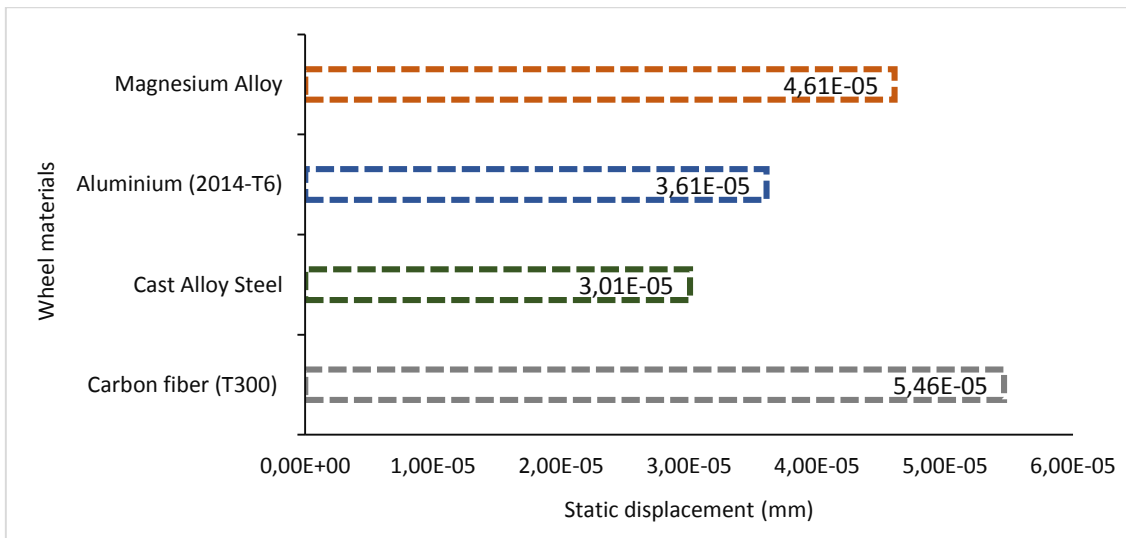
Figure 9. *Maximum static displacement derived from each wheel material*
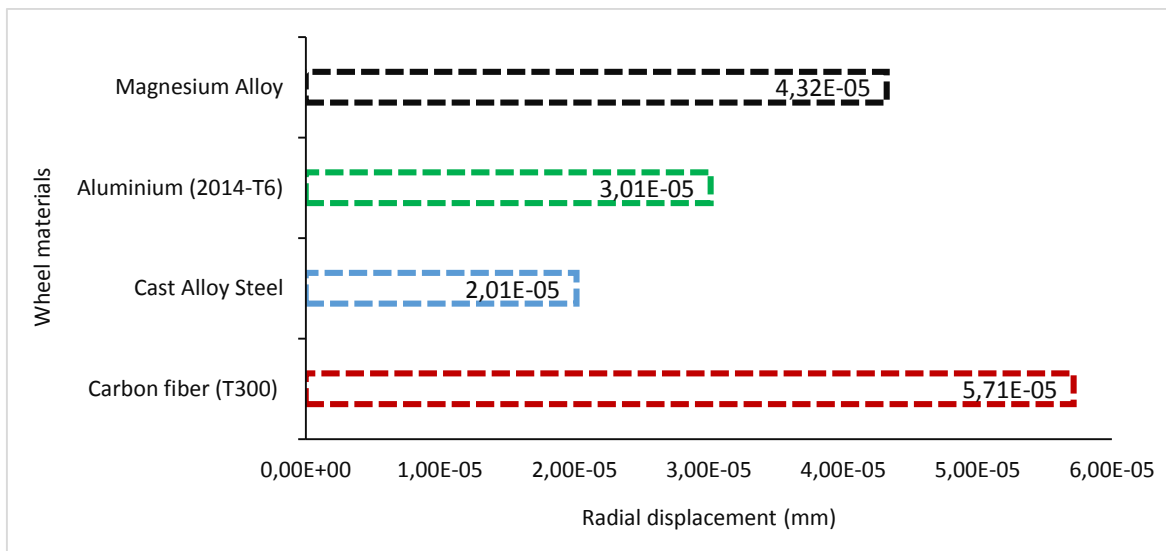
Figure 10. *Maximum radial displacement derived from each wheel material*
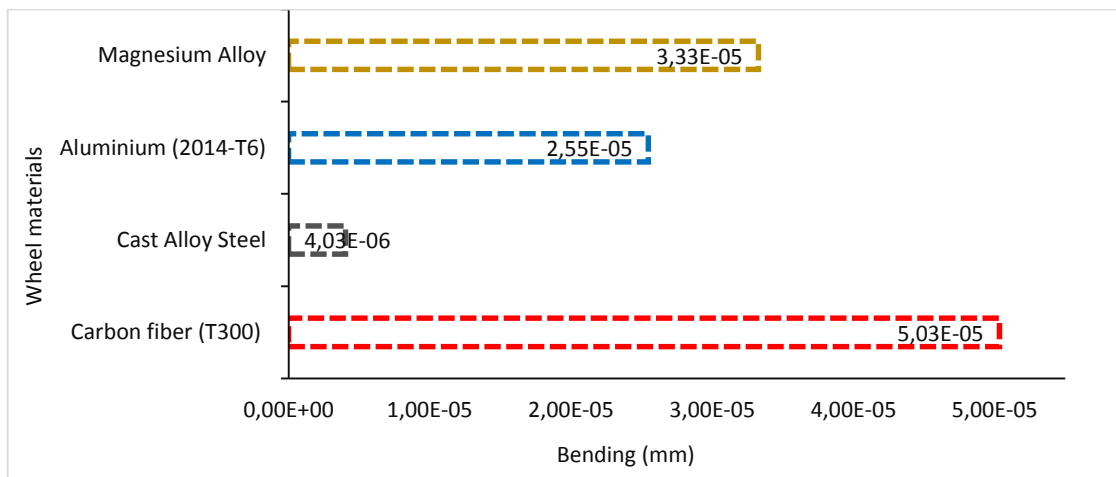
Figure 11. Maximum bending derived from each wheel material

4. Conclusion

The study reveals that Steel wheels (cast alloy steel) in terms of mass are heavier than aluminium (2014-T6), magnesium (alloy) and carbon fibre (T300) based wheels while wheels produced from carbon fibre are the lightest and aluminium wheels are slightly heavier than magnesium wheels. Weight of the wheel can be referred to unsprung weight particularly when it is denser which is not being cushioned by the suspension springs, and cast alloy steel is a clear example in this case. Acceleration and agility of the car is dampened by the excess weight of the wheel, lowers the vehicle's centre of gravity and causes it to drive sluggishly while also consuming more fuel. However, while wheels designed with carbon fibre are very expensive, steel wheels in terms of cost are the cheapest and inexpensive to replace if extremely damaged while wheels produced from magnesium alloy are cheaper than their aluminium counterpart. In terms of strength and resistance against in-service defects like bending, stress-strain deformation as well as static displacement, steel wheels are better choices followed by aluminium wheels and magnesium wheels. However, carbon fibre (T300) wheels tend to be brittle, cracks more easily and cannot withstand roads with pot holes and rough patches, whereas, steel, aluminium and magnesium wheels tend to bend at extremely high impact force and hardly cracks when impacted by road (particularly steel wheels) due to their toughness and somewhat ductile nature. In terms of thermal expansion, magnesium wheel is not a good choice of material when high temperature or long distance drive that will end up raising the auto wheel temperature is involved. In this case, carbon fibre is the best choice of auto wheel material among the four auto wheel materials reported in this study. This is seconded by steel

wheel and then aluminium wheel. When considering availability, the wide range of steel and aluminium wheels available for different purposes are easy to find irrespective of the size or style. In terms of rust/corrosion, wheels produced from carbon fibre are better choices followed by aluminium and the magnesium, but as long as the paint layer in steel wheels remain intact, steel wheel can hardly rust. Hence, the choice of auto wheel depends on the user's requirement. For example, steel wheel is the right choice when an inexpensive, strong, tough and rugged wheel is required (particularly in rough terrains) and vice versa.

Author Statements:

- The authors declare that they have equal right on this paper.
- The authors declare that they have no known competing financial interests or personal relationships that could have appeared to influence the work reported in this paper
- The authors declare that they have nobody or no-company to acknowledge.

References

[1] Thakare, R. B. "Stress analysis in wheel rim by using dynamic cornering fatigue test under different conditions". International journal of Advance Research and Innovative Ideas in Education, 3, 2(2017), 4863-4868.

[2] Nirala, S. K., Shankar, S., Sathishkumar, D., Kavivalluvan, V., Sivakumar, P. "Carbon fiber composites: A solution for light weight dynamic components of AFVs". Defence Science Journal, 67, 4(2017), 420-427.

[3] Natrayan, L., Santhakumar, P., Kumar, P. D., Raj, R. M., Mohandass, R. (2016) "Design and Comparative Analysis of Old and New Model Car Wheel Rims

with Various Materials." IETE Journal for Research, 2, 2(2016), 69-73.

[4] Nair, A., Kawade, S., Dias, B., George, I., Bhandarkar, D. K. "Performance Enhancement and Analysis By Reducing Weight of Unsprung Mass of Formula Student Racing Car". International Journal of Mechanical and Production Engineering, 6, 6(2018), 38-42.

[5] Dinesh K. M., Narendra M. P., Purna C. S. B., Touseef, A. M. "Static analysis of wheel rim using CATIA and ANSYS16.0. International Research Journal of Engineering and Technology, 3, 7(2016), 2256-2261.

[6] Bao,Y., Zhao, X. "Research of lightweight composite automobile wheel". World Journal of Engineering Technology, 5(2017) 675-683.

[7] Bisht, P. S., Awasthi, A. "Design and Analysis of Composite and Al Alloy Wheel Rim". Advances in Materials Engineering and Manufacturing Processes, 5(2020), 15-29.

[8] Blasco, J., Valero, F., Besa, A. and Rubio, F. "Design of a Dynamometric Wheel Rim". Mechanisms and Machine Science, 17(2014), 243-250.

[9] Babu, M., Hariharan, V. S. "Modelling and analysis of automotive wheel rim". International Journal of Innovative Research in Science, Engineering and Technology, 5, 4(2016), 6192-99.

[10] Panda, S. S., Gurung, J., Chatterjee, U. K., Sahoo S. "Modelling-and-Fatigue-Analysis-of- Automotive-Wheel-Rim". International Journal of Engineering Sciences and Research Technology, 5, 4(2016), 428-435.

[11] Prasad, T. D., Krishnaiah, T., Iliyas, J. M., Reddy, M. J. "A Review on Modelling and Analysis of Car Wheel Rim using CATIA and ANSYS". International Journal of Innovative Science and Modern Engineering, 2, 6(2014), 1-5.

[12] Venkateswarlu, G., Sharma, M. "Design and Analysis of Alloy Wheel with Different Alloys". International Journal of Advance Research in Science and Engineering, 6, 10(2017), 2488-2495.

[13] Kumar, D. S., Jayakumar. V., Majeed, S. "Modal Analysis and Design Optimization of Automotive Wheel Rim". Journal of Chemical and Pharmaceutical Sciences, 10, 1(2017), 667-669.

[14] Burande, D. H., Kazi, T. N. "Fatigue Analysis of Alloy Wheel for Passenger Car under Radial Load". International Journal of Engineering Research and General Science 4, 2(2016), 26-36.

[15] Sekhar, V., Mouli, A. C. "Design and Performance Analysis of Alloy Wheels using CATIA ANSYS Modelling Tool". International Journal of Scientific Engineering and Technology Research, 3, 43(2014), 8789-8793.

[16] Ikpe, A. E., Owunna, I., Ebunilo, P. O. "Comparison of Aluminium Wheel to Steel Wheel in Relation to Weight and Fuel Consumption (Energy) in Automobiles". Industrial and Systems Engineering, 1, 1(2016), 1-9.

[17] Stearns J., Srivatsan T., Gao, X., Lam, P. "Understanding the Influence of Pressure and Radial Loads on Stress and Displacement Response of a Rotating Body: The Automobile Wheel". International Journal of Rotating Machinery, 60193(2006), 1-8.

[18] Golub G. A., Chuba V. V., Marus O. A. "Determination of Rolling Radius of Self-Propelled Machines' Wheels". INMATEH-Agricultural Engineering, 57, 1(2019), 81-90.

[19] Pauwelussen, J. P., Dalhuijsen, W., Merts, M. "Tyre dynamics, tyre as a vehicle component Part 1: Tyre Handling Performance." Virtual Education in Rubber Technology, HAN University, Netherlands, 2007.

[20] Jazar R. N. "Vehicle dynamics: Theory and application, 3rd Edition." Switzerland, Springer, 2017.

[21] Wilson T., Siero M., Kopchick C., Vantsevich V. "Terrain Truck: Control of Wheel Rotational Velocities and Tire Slippages". SAE Technical Paper 2011-01-2157, 2011.

[22] Miller, S. L., Youngberg, B., Millie, A., Schweizer, P., Gerdes, J. C. "Calculating Longitudinal Wheel Slip and Tire Parameters Using GPS Velocity". Proceedings of the American Control Conference, Arlington, VA, June 25-27, (2001), 1800-1805.

[23] Smieszek, M., Dobrzanska, M., Dobrzanski, P. "The impact of load on the wheel rolling radius and slip in a small mobile platform". Autonomous Robots, 43(2019), 2095-2109.

[24] Undru, S., Reddy, P. P. "Design and Analysis of Aluminium Alloy Wheel". International Journal of Engineering Research and Application, 7, 3(2017), 57-65.

[25] Ren, F., Li, L., Jiang, Z., Song, T., Gong, Z., Shi, Y., Liu, B. "Analysis on Wheel-Ground Contact Load Characteristics of Unmanned Off-road Vehicles". Journal of Engineering Science and Technology Review 10, 3(2017), 97-103.

[26] Lapshin, V. P., Turkin, I. A. "Modelling Tractive Effort Torque of Wheel in Deformation Movements of Pneumatic Tire Wheel". Procedia Engineering, 206(2017), 594-599.

[27] Owunna, I. B., Ikpe, A. E. "Design Analysis of Reciprocating Piston for Single Cylinder Internal Combustion Engine". International Journal of Automotive Science and Technology, 4, 2(2020), 30-39.

[28] Ikpe, A. E., Owunna, I. B. "Design of Remotely Controlled Hydraulic Bottle Jack for Automobile Applications". International Journal of Engineering Research and Development, 11, 1(2019), 124-134.

[29] Ikpe, A. E., Owunna, I. "Design of Vehicle Compression Springs for Optimum Performance in their Service Condition". International Journal of Engineering Research in Africa, 33(2017), 22-34.

[30] Ikpe, A. E., Owunna, I. B. "A 3D Modelling of the In-Cylinder Combustion Dynamics of Two Stroke Internal Combustion Engine in its Service Condition". Nigerian Journal of Technology, 39, 1(2020), 161-172.

[31] Ikpe, A. E., Ndon, A. E., Adoh, A. U. "Modelling and Simulation of High Density Polyethylene Liner

Installation in Engineered Landfill for Optimum Performance. Journal of Applied Science and Environmental Management, 23, 3(2019), 449-456.

[32] Trang, T. T., Zhang, J. H., Kim, J. H., Zargaran, A., Hwang, J. H., Suh, B., Kim, N. J. "Designing a Magnesium Alloy with High Strength and High Formability". Nature Communication, 9(2018), 1-6.

[33] Mo, J. "Current Development of Creep-resistant Magnesium Cast Alloy: A Review". Materials and Design, 155(2018), 422-442.

[34] Ikpe, A. E., Orhorhoro, E. K., Gobir, A. "Design and Reinforcement of a B-Pillar for Occupants Safety in Conventional Vehicle Applications". International Journal of Mathematical, Engineering and Management Sciences, 2, 1(2017), 37-52.

[35] Ikpe, A. E., Owunna, I. B., Satope, P. "Design optimization of a B-pillar for crashworthiness of vehicle side impact". Journal of Mechanical Engineering and Sciences, 11, 2(2017), 2693-2710.

[36] Ikpe, A. E., Owunna, I. "Design of Vehicle Compression Springs for Optimum Performance in their Service Condition". International Journal of Engineering Research in Africa, 33(2017), 22-34.

[37] Ikpe, A. E., Efe-Ononeme, O. E., Ariavie, G. O. "Thermo-Structural Analysis of First Stage Gas Turbine Rotor Blade Materials for Optimum Service Performance". International Journal of Engineering and Applied Sciences, 10, 2(2018), 118-130.

[38] Ikpe, A. E., Owunna, I. B. "Design of Remotely Controlled Hydraulic Bottle Jack for Automobile Applications". International Journal of Engineering Research and Development, 11, 1(2019), 124-134.

[39] Owunna, I. B., Ikpe, A. E. "Design Analysis of Reciprocating Piston for Single Cylinder Internal Combustion Engine". International Journal of Automotive Science and Technology, 4, 2(2020), 30-39.

[40] Ikpe, A. E., Owunna, I., Ebunilo, P. O. "Determining the Accuracy of Finite Element Analysis when Compared to Experimental Approach for Measuring Stress and Strain on a Connecting Rod Subjected to Variable Loads". Journal of Robotics, Computer Vision and Graphics, 1, 1(2016), 12-20.

Research Article

Changes in Interaction Between Accessory Protein 8 and *IL17RA* in UK Isolates Caused by Mutations in the SARS-CoV-2 Open Reading Frame 8

Ekrem AKBULUT*

Malatya Turgut Özal University, Engineering and Natural Sciences Faculty, Bioengineering Department, 44200, Malatya-Turkey

* **Corresponding Author** : ekremakbulut@gmail.com **ORCID:** 0000-0002-7526-9835

Abstract:

SARS-CoV-2 is the infectous agent of COVID-19, one of the most important health problems of the twenty-first century. *IL17RA* is an crucial receptor in the generation of the host immune response. ORF8 is the viral accessory protein of SARS-CoV-2 that suppresses the host immune response. Mutations can alter the viral properties and clinical course of SARS-CoV-2. In this study, we investigated the changes that SARS-CoV-2 ORF8 mutations may cause in the interaction of *IL17RA* with ORF8. The study was carried out using 825 complete genome sequences from UK isolates. Mutation analyzes were performed using RDP4 and MEGAX. The protein model was created using the Swiss Model. Protein protein interaction was analyzed by Haddock ver 2.4. Analysis of changes in protein stability was performed using SDM2, mCSM stability and DUET tools. The change in ORF8 - *IL17RA* binding affinity before and after the mutation was evaluated using mCSM-PPI2. We detected P30S, R52I, Y73C and L118V mutations in SARS-CoV-2 ORF8. Mutations have been shown to reduce protein stability and affinity. After the mutation, the binding dynamics of ORF8 to *IL17RA* were changed. Molecular attachment scores were -78.0±3.4 kcal.mol^{-1} and -76.3±11.9 kcal.mol^{-1}, for wild type and mutant, respectively. After the mutations, the hydrogen bond number and position between ORF8 and *IL17RA* changed. While establishing ten hydrogen bonds between the wild type and *IL17RA*, four hydrogen bonds were established between the mutant ORF8 and *IL17RA*. The decreased affinity between ORF8 and *IL17RA* can be seen as a stronger immune response and a milder clinical course. Although our results contain important data for understanding ORF8, which is an important drug target, it needs to be repeated with in-vivo and crystallgraphy studies.

1. Introduction

Severe acute respiratory syndrome coronavirus 2 (SARS-CoV-2) has killed 3.27 million people since December 2019. SARS-CoV-2, which revealed the third largest coronavirus epidemic in the last 20 years, infected 160 million people [1,2]. The molecular basis of the severity and rapid spread of COVID-19 disease caused by SARS-CoV-2 is largely unknown [3]. Although prophylactic vaccine development studies have recently been successful in COVID-19 disease, the high mutation capacity and progressive evolutionary change of the virus genome pose the risk of overriding existing treatments [4]. SARS-CoV-2, which is of zoonotic

origin such as severe acute respiratory syndrome coronavirus (SARS) and Middle East respiratory syndrome (MERS), may be a sign that members of this family may cause serious health problems in the future, and even epidemics with transition between species [5,6].
The SARS-CoV-2 genome consists of 16 non-structural proteins, 4 structural proteins (S, M, E, N) and 5 accessory proteins [7]. Although the SARS-CoV-2 genome is known as the genetic code, the functional role of many accessory proteins is not clearly [8,9]. Open Reading Frame-8 (ORF8) from SARS-CoV-2 is an accessory protein consisting of 366 nucleotides. Its evolutionary distance from other beta coronaviruses makes SARS-CoV-2 ORF8 an

important research target [8]. ORF8 from SARS CoV-2 is a rapidly evolving accessory protein that has been proposed to interfere with immune responses [3]. ORF8 from SARS-CoV-2 disrupts antigen presentation and reduces the recognition and elimination of virus-infected cells [10]. ORF8 suppresses the immune response by reducing the expression of MHC I (*HLA-A2*) molecules. The major pathway for ORF8-mediated MHC-I downregulation is the lysosomal degradation. The proteins that ORF8 from SARS-CoV-2 interacts with in the host are localized in the endoplasmic reticulum [11]. This may result in the rearrangement of the ER traffic of host-ORF8 interactions during infection.

ORF8 from SARS-CoV-2 was shown to inhibit type I interferon (*IFN-β*) activation and NF-kappa-B pathway [12]. Cytokine binding triggers the homotypic interaction of the *IL17RA* and *IL-17RC* chains with the *TRAF3IP2* adapter, leading to *TRAF6*-mediated activation of the NF-kappa-B and MAP kinase pathways, resulting in the activation of cytokines, chemokines, antimicrobial peptides and matrix metallocationproteinases that will ultimately generate strong immune inflammation [13–15].
IL17RA involved in antiviral host defense through various mechanisms. *IL17RA* plays a role in the maintenance of the integrity of epithelial barriers during pathogen infection. It stimulates the production of antimicrobial beta-defensins *DEFB1*, *DEFB103A*, and *DEFB104A* by mucosal epithelial cells, limiting the entry of microbes through the epithelial barriers [16,17]. It contributes to virus clearance by driving the differentiation of B1a-B cells, providing for production of virüs specific IgM antibodies at first line of host defense [18]. *IL17RA* interaction with ORF8 from SARS-CoV-2 is one of the most important stages of viral infection that suppresses the immune response [4].
The discovery of effective treatments against SARS-CoV-2 requires full elucidation of the functional properties of the virus genome and proteome. Functional properties of many viral proteins, which are the target of treatment, can be achieved by in silico approaches in a shorter time and with less funds than conventional methods [19]. In this study, changes in ORF8 - *IL17RA* interaction caused by mutations in SARS-CoV-2 ORF8, which play a role in the suppression of the immune response, were analyzed using in-silico approaches.

2. Materials and Methods

2.1. Sequence and Mutation Data

This study was carried out using genome data of 825 SARS CoV-2 isolates from United Kingdom (UK). Genome data of the isolates were taken from GISAID EpiCoV database [20]. Reference ORF8 accesion code is YP_009724396.1. Protein sequence information of 825 isolates were aligned with the MAFFT (v7.475) multiple sequence alignment program FFT-NS-i algorithm [21,22]. The scoring matrix BLOSUM 80 and 1 PAM was chosen for the amino acid sequences and nucleotide, respectively [23,24]. Gap opening penalty was used as 2.0. The mutated residues were analyzed with RDP4 and MegaX tools [25,26].

2.2. Homology Model of Mutant Protein

Three-dimensional model of mutant ORF8 protein was generated by the method of homology modeling using Swiss-Model [27]. 7JTL (RCSB protein data bank code) was selected as template. ProSA and MolProbity tools were used for structural validation and model of wild type and mutant ORF8 proteins [28,29]. Secondary structure components (random coils, beta strands alpha helices) of ORF8 protein were defined by using PSIPRED [30]. Superimpose and conformational analysis of wild type and mutant proteins were performed with PyMOL (ver2.4.1). Topological differences of wild type and mutant ORF8 proteins were calculated with the i-Tasser TM-Score and root mean square deviation (RMSD) algorithm [31,32].

2.3. Docking

The wild type and mutant ORF8 proteins were used as ligands and *IL17RA* (pdb code 4HSA) was used as target for molecular docking with Haddock version 2.4. The contact points for the *IL17RA* were residues number 25, 26, 31, 87, 88, 89, 90, 91, 92, 261, 262 and 265. The contact points for the ORF8 were residues number 49, 56, 58, 71, 72, 73, 74, 75,76, 83, 84, 85 and 95. Number of structures for rigid body docking was set to 1000. Number of trials for rigid body minimisation was set to 5. Number of structures for semi-flexible refinement was set to 200. Refined with short molecular dynamics in open solvent using water. Clustering method was selected Fraction of Common Contacts (FCC). RMSD cutoff for clustering was set to 0.6 Å. Kyte-Doolittle hydrophobicity scale method was used for solvating. Cutoff distance (proton-acceptor) to define an hydrogen bond was set to 2.5 Å. Cutoff distance (carbon-carbon) to define an hydrophobic contact was set to 3.9 Å. Docking parameters were performed as blind docking with default values [33]. Docking results were visualized with Discovery SV (ver20.1, DDS Biovia) and PyMOL.

2.4. Protein Stability and Protein-Protein Affinity Analysis

Analysis of changes in protein stability was performed using SDM2 [34], mCSM stability and DUET tools [35]. The change in ORF8 - *IL17RA* binding affinity before and after the mutation was evaluated using the mCSM-PPI2 tool [36].

3. Results and Discussions

In this study, mutation analysis of UK isolates revealed Pro30Ser, Arg52Ile, Tyr73Cys and Leu118Val mutations. The homology model of the mutant ORF8 was created with the Swiss Model. The quality scores of the mutant model were -0.94, 0.67 and -3.83 for QMEAN, Molprobity, and ProSA, respectively. It was determined that the generated mutant ORF8 model was within the NMR quality limits (Figure 1). After docking, the TM-score (0.73) between the wild type ORF8 – *IL17RA* and the mutant ORF8- *IL17RA* complexes were observed to be topologically similar, although not high rate. The RMSD in supersposition was 0.28 Å. The change in the topological structure after the mutation can alter the protein-protein interaction [37].
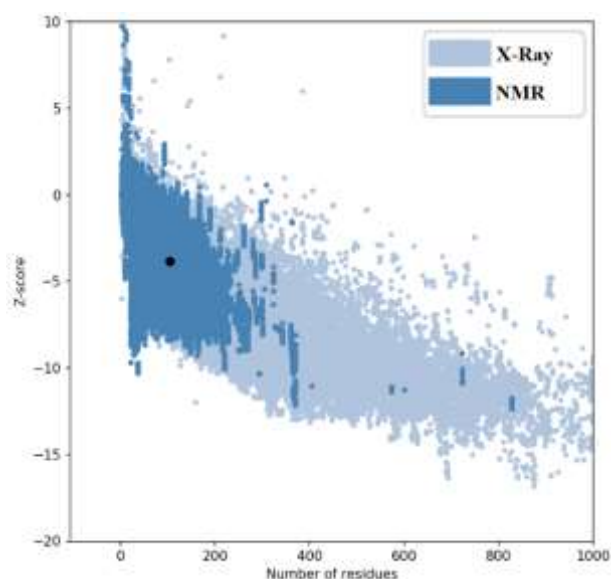
Figure 1. *Quality analysis of mutant ORF8 homology model.*

The docking analysis consolidated 132 structural models for the wild type ORF8 into 18 clusters, which represents 66 % of the water-refined models generated. The docking analysis consolidated 129 structural models for the mutant ORF8 into 17 clusters, which represents 64 % of the water-refined models generated. Docking analysis revealed the top 10 models with the lowest binding energy with *IL17RA* for wild type and mutant ORF8. The

docking score was -78.0 ± 3.4 kcal.mol^{-1} and -76.3 ± 11.9 kcal.mol^{-1} for wild type and mutant ORF8, respectively (Table 1). Molecular docking results showed that; the ten hydrogen bonds were established between the wild type ORF8 and *IL17RA*, while four hydrogen bonds were established between the mutant ORF8 and *IL17RA* (Table 2). The wild type ORF8 made contact with *IL17RA* on five locations, while between the mutant ORF8 and *IL17RA*, contact was made on three locations (Figure 2). The decrease in the number of hydrogen bonds and contact points established before mutation between ORF8 from SARS-CoV-2 and *IL17RA* explains the decreased affinity after the mutations.
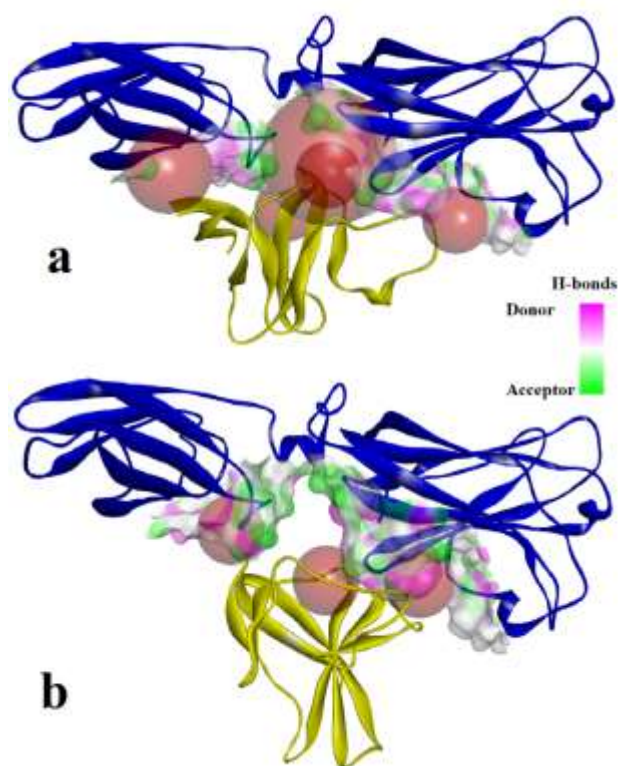
Figure 2. *Bonding motif of ORF8 and IL17RA with solid ribbon presentation. a) wild type ORF8-Il17RA complex, b) mutant ORF8-IL17RA complex (red spheres represent binding sites, solid surface represents the hydrogen bond interaction surface).*

Protein dynamic analysis showed that mutations in Tyr73 and Leu188 residues impair protein stability (Table 3). The ΔΔG values were -0.389 kcal.mol^{-1} and -0.85 kcal.mol^{-1}, respectively. However, the vibrational entropy energies between wild type and mutant showed that mutations in the Pro30, Tyr73 and Leu118 residues of the ORF8 increased protein flexibility, while the mutation at the Arg52 residue decreased flexibility (Table 3). The interaction data for ORF8 and *IL17RA* showed decreased affinity after mutation (ΔΔG^{affinity} -0.070, -0.201, -0.924 and -1.224 for P30S, R52I, Y73C and L118V, respectively). Unlike SARS and MERS, the physical

interaction of ORF8 from SARS-CoV-2 with *IL17RA* may be associated with the high virulence effect of SARS-CoV-2 and the severe clinical course of the disease [38–41].

Although ORF8 is known to modulate the systemic *IL17* signaling pathway in SARS-CoV-2 infections, its mechanism has not been fully elucidated. *IL17*, a pleitropic cytokine, is likely to play different roles in the immune system during SARS-CoV-2 infection. This makes solving the molecular mechanism of *IL17A* and SARS-CoV-2 ORF8 interaction more difficult [42]. Inactivation of *IL17RA* showed that it resulted in a significant reduction in SARS-CoV-2 viral replication in ACE2 cell lines. In this study, it was shown that the region where ORF8 from SARS-CoV-2 binds with the lowest binding energy on *IL17RA* is the binding site of *IL17F* [13]. The regulatory effect of unique signaling properties of *IL17RA* on innate and adaptive immune systems is a result of its interaction with *IL17F* [43,44]. Disruption of the interaction between *IL17RA* and *IL17F* by the ORF8 linkage may be one of the main mechanisms explaining the process of suppressing the immune response. Engaging the binding site of *IL17RA*, a common receptor for the *IL17* family, with ORF8 may suppress the cytokine signaling process. One of regions of sequence unique to SARS-CoV-2 begins after Cys61 and extends until before the Cys83-Leu84-Pro85 conserved motif. SARS-CoV-2-specific [73]YIDI[76] motif occurs at the center of this region. The YIDI motif is responsible for stabilizing an extensive non-covalent dimer interface [3]. The combination of Leu95, Ile58, Val49, and Pro56 form a hydrophobic interaction with Tyr73 of the YIDI motif. In this study, it was shown that the Tyr73Cys mutation caused an increase in flexibility and a decrease in stabilization. It appears that the occurring mutation of Tyr73 may adversely affect the stabilization of the dimer interface. This may affect the functional properties of ORF8 from SARS-CoV-2. Mutations can alter virulence characteristics of SARS-CoV-2 and affect the clinical course of the disease. The clinical effect of deletions in ORF8 may be a milder infection with less systemic release of proinflammatory cytokines and a more efficient immune response to SARS-CoV-2 [42,45].

In conclusion, it was shown in this study that 4 mutations identified in ORF8 from SARS-CoV-2 caused changes in the dynamic properties of the protein and this may result in a decrease in *IL17RA* affinity. These data will contribute to elucidating the functional properties of ORF8, which is an important therapeutic target. More studies are needed to fully elucidate how ORF8 from SARS-CoV-2 suppresses the host immune system.

Author Statements:

Table 1. Docking scores of wild and mutant ORF8 with IL17RA

		DocSc	i-RMSD	Evdw	Eelec	Edesolv	Eair	Z-Score
1	W	-78.0 ± 3.4	2.4 ± 0.4	-40.9 ± 5.1	-220.6 ± 34.4	-1.3 ± 3.4	83.5 ± 25.7	-2.1
	M	-76.3 ± 11.9	11.9 ± 0.1	-48.2 ± 4.1	-164.5 ± 25.7	-1.2 ± 3.0	60.4 ± 40.1	-1.8
2	W	-71.8 ± 6.5	14.0 ± 0.4	-35.0 ± 7.0	-255.8 ± 26.1	0.4 ± 3.1	139.1 ± 41.0	-1.2
	M	-74.8 ± 10.8	0.7 ± 0.4	-49.0 ± 7.4	-191.9 ± 7.3	-0.1 ± 3.7	125.8 ± 81.5	-1.6
3	W	-66.5 ± 8.0	8.3 ± 0.6	-35.8 ± 3.3	-186.5 ± 29.5	1.5 ± 1.7	51.3 ± 38.9	-0.4
	M	-65.8 ± 11.8	11.4 ± 0.7	-37.1 ± 5.9	-189.3 ± 73.7	1.5 ± 2.3	76.0 ± 43.8	-0.4
4	W	-66.4 ± 3.6	6.7 ± 1.2	-47.5 ± 10.9	-160.2 ± 43.6	5.4 ± 2.4	76.9 ± 14.0	-0.4
	M	-64.4 ± 5.3	13.6 ± 0.3	-41.1 ± 2.8	-165.3 ± 24.1	2.5 ± 2.6	72.9 ± 31.3	-0.2

5	W	-63.4 ± 2.4	13.1 ± 0.1	-32.1 ± 5.9	-198.1 ± 14.5	8.0 ± 1.8	3.5 ± 3.2	-0.0
	M	-61.2 ± 4.5	10.9 ± 0.0	-31.6 ± 9.1	-253.9 ± 23.1	12.2 ± 2.1	90.1 ± 21.0	0.2
6	W	-60.3 ± 8.2	14.1 ± 0.3	-33.3 ± 4.7	-179.6 ± 24.9	-2.7 ± 4.6	116.7 ± 55.7	0.4
	M	-60.0 ± 7.8	5.1 ± 0.4	-32.1 ± 3.2	-214.9 ± 50.4	9.0 ± 3.1	61.1 ± 28.6	0.3
7	W	-58.8 ± 6.3	11.3 ± 0.0	-42.0 ± 8.2	-112.3 ± 32.6	0.8 ± 2.2	48.1 ± 20.1	0.6
	M	-59.9 ± 5.4	13.8 ± 0.1	-31.8 ± 1.7	-220.6 ± 25.5	3.4 ± 1.3	125.5 ± 39.0	0.4
8	W	-57.8 ± 5.4	12.5 ± 0.7	-32.8 ± 3.8	-180.0 ± 52.8	4.4 ± 4.8	66.8 ± 60.1	0.8
	M	-58.2 ± 1.7	8.1 ± 0.7	-41.5 ± 4.9	-120.8 ± 11.6	2.5 ± 1.4	49.9 ± 23.9	0.6
9	W	-56.8 ± 5.9	13.3 ± 0.3	-38.5 ± 3.9	-155.9 ± 10.5	-1.1 ± 0.3	139.7 ± 63.1	0.9
	M	-53.4 ± 10.5	7.4 ± 0.5	-35.3 ± 7.1	-176.7 ± 22.2	-1.7 ± 0.6	188.8 ± 10.7	1.2
10	W	-53.5 ± 1.7	10.5 ± 0.2	-39.7 ± 3.5	-164.0 ± 42.1	10.3 ± 2.9	86.8 ± 14.9	1.4
	M	-52.1 ± 3.8	11.2 ± 0.2	-36.2 ± 3.8	-136.4 ± 33.7	4.6 ± 4.0	67.7 ± 32.3	1.4

DocSc: docking score, i-RMSD: interface RMSD (from the overall lowest-energy structure), Evdw: Van der Waals energy, Eelec: electrostatic energy, Edesolv: desolvation energy, Eair:restraints violation energy.

Table 2. *Hydrogen bond interaction for ORF8-IL17RA complexes*

Hydrogen bond	*IL17RA*	ORF8
wild type	Asn91:HN	Gln72:O
	Asn91:O	Gln72:HN
	Arg93:HH21	Ser69:O
	Asp123:OD2	Lys94:HZ3
	Asp123:O	Lys94:HZ1
	Gln124: OE1	Lys94:HZ1
	Gln200:HE22	Asp119:OD2
	Asn261:OD1	Glu92:HN
	Asp262:OD1	Gln27:HE22
	Asp262:OD2	Gln91:HE22
mutant	Asn89:O	Ile74:HN
	Asp121:OD2	Lys94:HZ2
	Asp121:OD2	Lys94:HZ3
	Ser257:O	His28:HE2

Table 3. *Effects of mutant residues on protein dynamics.*

wild	position	mutant	ΔΔG (kcal.mol⁻¹)					ΔΔS (kcal.mol⁻¹.K⁻¹)	Flex.
			ENCoM	DynaMut	mCSM	SDM	DUET	ENCoM	
Pro	30	Ser	-0.144	0.146	-1.000	0.810	-0.372	0.180	Inc
Arg	52	Ile	0.124	0.436	0.206	0.910	0.414	-0.155	Dec
Tyr	73	Cys	-0.525	-0.389	-0.526	-0.040	-0.290	0.656	Inc
Leu	118	Val	-0.248	-0.850	-1.593	-1.580	-1.712	0.310	Inc

Flex.: Flexibility

References

[1] Worldometer, "Coronavirus Cases" Worldometer (2020) 1–22. https://doi.org/10.1101/2020.01.23.20018549V2.

[2] P. Zhou, X. Lou Yang, X.G. Wang, B. Hu, L. Zhang, W. Zhang, H.R. Si, Y. Zhu, B. Li, C.L. Huang, H.D. Chen, J. Chen, Y. Luo, H. Guo, R. Di Jiang, M.Q. Liu, Y. Chen, X.R. Shen, X. Wang, X.S. Zheng, K. Zhao, Q.J. Chen, F. Deng, L.L. Liu, B. Yan, F.X. Zhan, Y.Y. Wang, G.F. Xiao, Z.L. Shi, "A pneumonia outbreak associated with a new coronavirus of probable bat origin" Nature 579 (2020) 270–273. https://doi.org/10.1038/s41586-020-2012-7.

[3] T.G. Flower, C.Z. Buffalo, R.M. Hooy, M. Allaire, X. Ren, J.H. Hurley, "Structure of SARS-CoV-2 ORF8, a rapidly evolving coronavirus protein implicated in immune evasion" Proceedings of the National Academy of Sciences 118 (2020) 1–6. https://doi.org/10.1101/2020.08.27.270637.

[4] D.E. Gordon, D.E. Gordon, J. Hiatt, M. Bouhaddou, V. V Rezelj, S. Ulferts, "Comparative host-coronavirus protein interaction networks reveal pan-viral disease mechanisms" Science 9403 (2020) 1–38.

[5] A. Fontanet, B. Autran, B. Lina, M.P. Kieny, S.S.A. Karim, D. Sridhar, "SARS-CoV-2 variants and ending the COVID-19 pandemic" The Lancet 397 (2021) 952–954. https://doi.org/10.1016/S0140-6736(21)00370-6.

[6] M. Miao, E. De Clercq, G. Li, "Genetic Diversity of SARS-CoV-2 over a One-Year Period of the COVID-19 Pandemic: A Global Perspective" Biomedicines 9 (2021) 412. https://doi.org/10.3390/biomedicines9040412.

[7] F. Wu, S. Zhao, B. Yu, Y.M. Chen, W. Wang, Z.G. Song, Y. Hu, Z.W. Tao, J.H. Tian, Y.Y. Pei, M.L. Yuan, Y.L. Zhang, F.H. Dai, Y. Liu, Q.M. Wang, J.J. Zheng, L. Xu, E.C. Holmes, Y.Z. Zhang, "A new coronavirus associated with human respiratory disease in China" Nature 579 (2020) 265–269. https://doi.org/10.1038/s41586-020-2008-3.

[8] F. Pereira, "Evolutionary dynamics of the SARS-CoV-2 ORF8 accessory gene" Infection, Genetics and Evolution 85 (2020) 1–10. https://doi.org/10.1016/j.meegid.2020.104525.

[9] C. Baruah, P. Devi, D.K. Sharma, "Sequence analysis and structure prediction of SARS-CoV-2 accessory proteins 9b and ORF14: Evolutionary analysis indicates close relatedness to bat coronavirus" BioMed Research International 2020 (2020) 1–13. https://doi.org/10.1155/2020/7234961.

[10] Y. Zhang, J. Zhang, Y. Chen, B. Luo, Y. Yuan, F. Huang, T. Yang, F. Yu, J. Liu, B. Liu, Z. Song, J. Chen, T. Pan, X. Zhang, Y. Li, R. Li, W. Huang, F. Xiao, H. Zhang, "The ORF8 protein of SARS-CoV-2 mediates immune evasion through potently downregulating MHC-I" BioRxiv (2020) 1–41. https://doi.org/10.1101/2020.05.24.111823.

[11] et al. Gordon DE, Jang GM, Bouhaddou M, "A SARS-CoV-2 protein interaction map reveals targets for drug repurposing" Nature 583 (2020) 1–13.

[12] J.Y. Li, C.H. Liao, Q. Wang, Y.J. Tan, R. Luo, Y. Qiu, X.Y. Ge, "The ORF6, ORF8 and nucleocapsid proteins of SARS-CoV-2 inhibit type I interferon signaling pathway" Virus Research 286 (2020) 198074. https://doi.org/10.1016/j.virusres.2020.198074.

[13] L.K. Ely, S. Fischer, K.C. Garcia, "Structural basis of receptor sharing by interleukin 17 cytokines" Nature Immunology 10 (2009) 1245–1251. https://doi.org/10.1038/ni.1813.

[14] D. Toy, D. Kugler, M. Wolfson, T. Vanden Bos, J. Gurgel, J. Derry, J. Tocker, J. Peschon, "Cutting Edge: Interleukin 17 Signals through a Heteromeric Receptor Complex" The Journal of Immunology 177 (2006) 36–39. https://doi.org/10.4049/jimmunol.177.1.36.

[15] M. Kurte, P. Luz-Crawford, A.M. Vega-Letter, R.A. Contreras, G. Tejedor, R. Elizondo-Vega, L. Martinez-Viola, C. Fernández-O'Ryan, F.E. Figueroa, C. Jorgensen, F. Djouad, F. Carrión, "IL17/IL17RA as a novel signaling axis driving mesenchymal stem cell therapeutic function in experimental autoimmune encephalomyelitis" Frontiers in Immunology 9 (2018) 802. https://doi.org/10.3389/fimmu.2018.00802.

[16] V. Ramirez-Carrozzi, A. Sambandam, E. Luis, Z. Lin, S. Jeet, J. Lesch, J. Hackney, J. Kim, M. Zhou, J. Lai, Z. Modrusan, T. Sai, W. Lee, M. Xu, P. Caplazi, L. Diehl, J. De Voss, M. Balazs, L. Gonzalez, H. Singh, W. Ouyang, R. Pappu, "IL-17C regulates the innate immune function of epithelial cells in an autocrine manner" Nature Immunology 12 (2011) 1159–1166. https://doi.org/10.1038/ni.2156.

[17] B. Neupane, D. Acharya, F. Nazneen, G. Gonzalez-Fernandez, A.S. Flynt, F. Bai, "Interleukin-17A Facilitates Chikungunya Virus Infection by Inhibiting IFN-α2 Expression" Frontiers in Immunology 11 (2020) 2955. https://doi.org/10.3389/fimmu.2020.588382.

[18] W.T. Ma, X.T. Yao, Q. Peng, D.K. Chen, "The protective and pathogenic roles of IL-17 in viral infections: Friend or foe?" Open Biology 9 (2019) 190109. https://doi.org/10.1098/rsob.190109.

[19] V.K. Bhardwaj, R. Singh, P. Das, R. Purohit, "Evaluation of acridinedione analogs as potential SARS-CoV-2 main protease inhibitors and their comparison with repurposed anti-viral drugs" Computers in Biology and Medicine 128 (2021) 1–13. https://doi.org/10.1016/j.compbiomed.2020.104117 .

[20] GISAID, "GISAID - Next hCoV-19 App" Genomic Epidemiology of HCoV-19 (2020). https://www.gisaid.org (accessed April 1, 2021).

[21] K. Katoh, "MAFFT: a novel method for rapid multiple sequence alignment based on fast Fourier transform" Nucleic Acids Research 30 (2002) 3059–3066. https://doi.org/10.1093/nar/gkf436.

[22] K. Katoh, J. Rozewicki, K.D. Yamada, "MAFFT online service: Multiple sequence alignment, interactive sequence choice and visualization" Briefings in Bioinformatics 20 (2018) 1160–1166. https://doi.org/10.1093/bib/bbx108.

[23] D.W. Mount, "Using BLOSUM in sequence alignments" Cold Spring Harbor Protocols 3 (2008) pdb-top39. https://doi.org/10.1101/pdb.top39.

[24] D.W. Mount, "Using PAM matrices in sequence alignments" Cold Spring Harbor Protocols 3 (2008) 1–9. https://doi.org/10.1101/pdb.top38.

[25] D.P. Martin, B. Murrell, M. Golden, A. Khoosal, B. Muhire, "RDP4: Detection and analysis of recombination patterns in virus genomes" Virus Evolution 1 (2015). https://doi.org/10.1093/ve/vev003.

[26] S. Kumar, G. Stecher, M. Li, C. Knyaz, K. Tamura, "MEGA X: Molecular evolutionary genetics analysis across computing platforms" Molecular Biology and Evolution 35 (2018) 1547–1549. https://doi.org/10.1093/molbev/msy096.

[27] A. Waterhouse, M. Bertoni, S. Bienert, G. Studer, G. Tauriello, R. Gumienny, F.T. Heer, T.A.P. De Beer, C. Rempfer, L. Bordoli, R. Lepore, T. Schwede, "Swiss-Model: Homology modelling of protein structures and complexes" Nucleic Acids Research 46 (2018) W296–W303. https://doi.org/10.1093/nar/gky427.

[28] M. Wiederstein, M.J. Sippl, "ProSA-web: Interactive web service for the recognition of errors in three-dimensional structures of proteins" Nucleic Acids Research (2007). https://doi.org/10.1093/nar/gkm290.

[29] V.B. Chen, W.B. Arendall, J.J. Headd, D.A. Keedy, R.M. Immormino, G.J. Kapral, L.W. Murray, J.S. Richardson, D.C. Richardson, "MolProbity: All-atom structure validation for macromolecular crystallography" Acta Crystallographica Section D: Biological Crystallography 66 (2010) 12–21. https://doi.org/10.1107/S0907444909042073.

[30] D.W.A. Buchan, F. Minneci, T.C.O. Nugent, K. Bryson, D.T. Jones, "Scalable web services for the PSIPRED Protein Analysis Workbench." Nucleic Acids Research 41 (2013) W349–W357. https://doi.org/10.1093/nar/gkt381.

[31] Y. Zhang, J. Skolnick, "Scoring function for automated assessment of protein structure template quality" Proteins: Structure, Function and Genetics 57 (2004) 702–710. https://doi.org/10.1002/prot.20264.

[32] J. Xu, Y. Zhang, "How significant is a protein structure similarity with TM-score = 0.5?" Bioinformatics 26 (2010) 889–895. https://doi.org/10.1093/bioinformatics/btq066.

[33] G.C.P. Van Zundert, J.P.G.L.M. Rodrigues, M. Trellet, C. Schmitz, P.L. Kastritis, E. Karaca, A.S.J. Melquiond, M. Van Dijk, S.J. De Vries, A.M.J.J. Bonvin, "The HADDOCK2.2 Web Server: User-Friendly Integrative Modeling of Biomolecular Complexes" Journal of Molecular Biology 428 (2016) 720–725. https://doi.org/10.1016/j.jmb.2015.09.014.

[34] A.P. Pandurangan, B. Ochoa-Montaño, D.B. Ascher, T.L. Blundell, "SDM: A server for predicting effects of mutations on protein stability" Nucleic Acids Research 45 (2017) W229–W235. https://doi.org/10.1093/nar/gkx439.

[35] D.E. V Pires, D.B. Ascher, T.L. Blundell, "DUET: a server for predicting effects of mutations on protein stability using an integrated computational approach" Nucleic Acids Research 42 (2014) W314–W319.

[36] C.H.M. Rodrigues, Y. Myung, D.E.V. Pires, D.B. Ascher, "MCSM-PPI2: predicting the effects of mutations on protein-protein interactions" Nucleic Acids Research 47 (2019) W338–W344. https://doi.org/10.1093/nar/gkz383.

[37] D. Davis, Ö.N. Yaveroılu, N. Malod-Dognin, A. Stojmirovic, N. Pržulj, "Topology-function conservation in protein-protein interaction networks" Bioinformatics 31 (2015) 1632–1639. https://doi.org/10.1093/bioinformatics/btv026.

[38] Y. Liu, C. Zhang, F. Huang, Y. Yang, F. Wang, J. Yuan, Z. Zhang, Y. Qin, X. Li, D. Zhao, S. Li, S. Tan, Z. Wang, J. Li, C. Shen, J. Li, L. Peng, W. Wu, M. Cao, L. Xing, Z. Xu, L. Chen, C. Zhou, W.J. Liu, L. Liu, C. Jiang, "Elevated plasma levels of selective cytokines in COVID-19 patients reflect viral load and lung injury" National Science Review 7 (2020) 1003–1011. https://doi.org/10.1093/nsr/nwaa037.

[39] C. Huang, Y. Wang, X. Li, L. Ren, J. Zhao, Y. Hu, L. Zhang, G. Fan, J. Xu, X. Gu, Z. Cheng, T. Yu, J. Xia, Y. Wei, W. Wu, X. Xie, W. Yin, H. Li, M. Liu, Y. Xiao, H. Gao, L. Guo, J. Xie, G. Wang, R. Jiang, Z. Gao, Q. Jin, J. Wang, B. Cao, "Clinical features of patients infected with 2019 novel coronavirus in Wuhan, China" The Lancet 395 (2020) 497–506. https://doi.org/10.1016/S0140-6736(20)30183-5.

[40] C. Qin, L. Zhou, Z. Hu, S. Zhang, S. Yang, Y. Tao, C. Xie, K. Ma, K. Shang, W. Wang, D.S. Tian, "Dysregulation of immune response in patients with coronavirus 2019 (COVID-19) in Wuhan, China" Clinical Infectious Diseases 71 (2020) 762–768. https://doi.org/10.1093/cid/ciaa248.

[41] G. Chen, D. Wu, W. Guo, Y. Cao, D. Huang, H. Wang, T. Wang, X. Zhang, H. Chen, H. Yu, X. Zhang, M. Zhang, S. Wu, J. Song, T. Chen, M. Han, S. Li, X. Luo, J. Zhao, Q. Ning, "Clinical and immunological features of severe and moderate coronavirus disease 2019" Journal of Clinical Investigation 130 (2020) 2620–2629. https://doi.org/10.1172/JCI137244.

[42] B.E. Young, S.W. Fong, Y.H. Chan, T.M. Mak, L.W. Ang, D.E. Anderson, C.Y.P. Lee, S.N. Amrun, B. Lee, Y.S. Goh, Y.C.F. Su, W.E. Wei, S. Kalimuddin, L.Y.A. Chai, S. Pada, S.Y. Tan, L. Sun, P. Parthasarathy, Y.Y.C. Chen, T. Barkham, R.T.P. Lin, S. Maurer-Stroh, Y.S. Leo, L.F. Wang, L. Renia, V.J. Lee, G.J.D. Smith, D.C. Lye, L.F.P. Ng, "Effects of a major deletion in the SARS-CoV-2 genome on the severity of infection and the inflammatory response: an observational cohort study" The Lancet 396 (2020) 603–611. https://doi.org/10.1016/S0140-6736(20)31757-8.

[43] A. Goepfert, S. Lehmann, J. Blank, F. Kolbinger, J.M. Rondeau, "Structural Analysis Reveals that the

Cytokine IL-17F Forms a Homodimeric Complex with Receptor IL-17RC to Drive *IL17RA*-Independent Signaling" Immunity 52 (2020) 499-512.e5.
https://doi.org/10.1016/j.immuni.2020.02.004.

[44] M. Veldhoen, "Interleukin 17 is a chief orchestrator of immunity" Nature Immunology 18 (2017) 612–621. https://doi.org/10.1038/ni.3742.

[45] L. Zinzula, "Lost in deletion: The enigmatic ORF8 protein of SARS-CoV-2" Biochemical and Biophysical Research Communications 538 (2021) 116–124.
https://doi.org/10.1016/j.bbrc.2020.10.045.

Research Article

Comprehensive Analysis of Forest Fire Detection using Deep Learning Models and Conventional Machine Learning Algorithms

Süha Berk KUKUK[1], Zeynep Hilal KİLİMCİ[2, *]

[1]Gedik University, Engineering Faculty, Department of Mechatronic Engineering, 34876, İstanbul-Turkey
shbkukuk@gmail.com-- **ORCID:** 0000-0003-1651-2417--

[2]Kocaeli University, Technology Faculty, Department of Information Systems Engineering, 41001, Kocaeli-Turkey
* **Corresponding Author**: zeynep.kilimci@kocaeli.edu.tr -- **ORCID:** 0000-0003-1497-305X

Abstract:

Forest fire detection is a very challenging problem in the field of object detection. Fire detection-based image analysis have advantages such as usage on wide open areas, the possibility for operator to visually confirm presence, intensity and the size of the hazards, lower cost for installation and further exploitation. To overcome the problem of fire detection in outdoors, deep learning and conventional machine learning based computer vision techniques are employed to determine the fire detection when indoor fire detection systems are not capable. In this work, we propose a comprehensive analysis of forest fire detection using conventional machine learning algorithms, object detection techniques, deep and hybrid deep learning models. The contribution of this work to the literature is to analyze different classification and object detection techniques in more details that is not addressed before in order to detect forest fire. Experiment results demonstrate that convolutional neural networks outperform other methods with 99.32% of accuracy result.

1. Introduction

Forest fire is unplanned, uncontrolled, unwanted fire what start natural or people cause. Forest fire results in a huge number of global disasters, causing endless economic and ecological losses as well as endangering living population. Every year, after all, millions of hectares of forest are destroyed by forest fire, which seriously just lost source oxygen and rise carbon dioxide cause change earth climate. In order to guard living population and preserve natural resource fire detection and fighting with fire have been seen as one of the most important solution. Traditional fire detect systems are heat detectors, smoke detectors, carbon monoxide detectors and manual call points. All of fire detect systems don't successfully work outdoors because they because are designed to work indoors.

Forest fire detection is a very challenging problem computer vision in the field of object detection. Fire detection-based image analysis have advantages such as usage on wide open areas, the possibility for operator to visually confirm presence, intensity and the size of the hazards, lower cost for installation and further exploitation. To overcome the problem of fire detection in outdoors, deep learning and conventional machine learning based computer vision techniques are employed to determine the fire detection when indoor fire detection systems are not capable. [1-3].

In addition to traditional machine learning methods, the application of deep learning algorithms has become very popular in recent years in different research areas such as image processing [2], natural language processing [4], speech recognition [5], and machine translation [6], computer vision [7], etc. Deep learning models are opted by scientists and researchers since they present better forecasts when compared to conventional machine learning techniques. Deep learning models are employed for the purpose of ensuring automatic feature extraction by training complex features to acquire more informative demonstration of data. In addition to this, deep learning methods are also utilized employed for the classification tasks in many areas

[8-10]. Convolutional neural networks (CNNs), recurrent neural networks (RNNs), long short-term memory networks (LSTMs), generative adversarial Networks (GANs), radial basis function networks (RBFs), and deep belief networks (DBNs) are widely used and well-known architectures. Both traditional machine learning techniques and deep learning methodologies are employed to detect fire indoors and outdoors [11-15].

In this paper, we propose an efficient forest fire detection model by using traditional machine learning algorithms, deep learning models, hybrid deep learning methodologies and object detection techniques (OD) in order to demonstrate the most successful system by comparing the performance of them. For this purpose, support vector machines (SVMs) and random forest (RF) models are evaluated as conventional machine learning techniques. CNN as deep learning model, convolutional neural network-gated recurrent unit (CNN-GRU) and convolutional neural network-long short-term memory (CNN-LSTM) as hybrid deep learning techniques, and Single Shot Detector (SSD), faster region based convolutional neural network (Faster R-CNN) as OD methodology are assessed. In order to demonstrate the efficiency of proposed model, two different the data sets are collected from two different sources. DL techniques have changeable hyper parameters that are the better get result for models. We also attempt model's different version used that disparate hyperparameters to acquire the best performance by evaluating eight different combination every model of hyper parameters. The results of extensive experiment indicate that CNN model exhibits superior classification performance in order to detect forest fire compared to all other techniques. To the best of our knowledge, this is the very first attempt in terms of utilizing and comparing the performance of various models such as traditional machine learning algorithms, deep learning models, hybrid deep learning methodologies, object detection techniques.

The rest of this article is arranged as follows: Section 2 provides a summary of studies on fire detection. Section 3 includes methods used in this work, including machine learning techniques deep learning, hybrid deep learning and object detection models. Section 4 introduces proposed framework. The experiment results, discussion and conclusion parts are given in Sections 5 and 6, respectively.

2. Related Work

This section provides a brief summary of the state-of-the-art studies on fire detection. In [7], Rafiee et al. investigate which object was smoke and fire by taking all objects in an image. Authors perform detection of smoke using color, mobility and tissue disorder characteristics. In [8], Ren et al. present performance of support vector machine (SVM) algorithm as a machine learning algorithm for fire classification in open space using color channels. They report that it is possible to calculate which color channel is outweighed in the image and whether it contains fire in the image according to the four main rules set in the color channels special. Data sets consisting of video images are labelled. F-measure is employed as an evaluation metric to demonstrate the success of support vector machine technique. They conclude the paper that the usage of SVM ensures 93.52% classification success.

In [9], Sadewa et al. propose to reduce the time elapsed from the start of the fire to the shortest time so that smoke sensors can test smoke indoors. For this purpose, the data received by the web cam placed at a corner point of the room instead of the smoke sensor is gathered. The data is first preprocessed by image processing techniques and then model training is carried out using evolutionary neural network. Inception-v3 model that is a convolutional neural network architecture from the Inception family and bottleneck features to classify class of fire. In [10], a real time fire detector is developed using faster region-based convolutional neural networks (Faster R-CNN). For fire detection system process of the machine learning, 1,000 images which are comprise fire and forest scenes are splitted into training (80%) and validation sets (20%). Experiment results demonstrate that Faster R-CNN is capable to detect fire and forest scene with 99% of accuracy. In [11], Mwedzi et al. introduce an intelligent fire detection system procedure with the use of computer vision and convolutional neural network to analyze the performance of the fire detection system under various setup scenarios. CNN and VGG-net models are used for fire detection system. The data set is constructed by using Google image search. The efficiency of the trained neural network data set of images are classified based on the precise images at the test stage. The experiment results are demonstrated that the proposed intelligent fire detection system presents significant improvement as compared to non-intelligent mechanisms. Through the application of CNN and VGGNet models, the system performs better result with 85% of accuracy and minimizes false alarm. In [13], Xu et al, propose to detect forest fire by employing deep learning methodology. Yolov5 and EfficientDet are utilized for fire detection process. The paper was created a single integrated forest fire dataset containing 10,581 images, with 2976 forest fire images and 7605 non-fire images. Experiments on the dataset

show that the proposed method improves detection performance by 2.5% to 10.9%, and decreases false positives by 51.3%, without any extra latency. In [14], Pourghasemi et al. assess forest fire detection sensitivities in Fars Province, Iran. Three geographic information system-based machine learning techniques are utilized, namely regression tree, general linear model and compound discriminant test. Data set is composed of satellite images on forest. 358 sites in the data set are divided into two sets for training (70%) and validation (30%). The BRT model is got access of accuracy is 83%. They conclude the paper that resulting maps can enhance the effectiveness of planning and management of forest resources and ecological balances in this province area. In [15], Maksymiv et al. focus on fire detection by combining some advantages of the AdaBoost, local binary pattern (LBP) and convolutional neural network for the purpose of both accelerating the processing time and providing better performance. Execution time is in the millisecond range, thus verifying that the developed system can operate in real time at video rates. In addition, the utilization of CNN technique exhibits more accurate classification success. The performance of CNN is validated on the data set with five hundred images, which contain such category as smoke, fire, others. The empirical results show that the method achieves more than 95% correct detection rate.

Our study differs in literature studies aforementioned in that it enables to evaluate various machine learning algorithms, deep and hybrid learning algorithms, and object detection model. To our knowledge, it is the first study to evaluate forest fire in such a comprehensive way in terms of six different techniques and two different size data sets.

3. Models

In this section, methods used in this work, including machine learning techniques, deep and hybrid deep learning and object detection models are briefly presented.

3.1. Support Vector Machine (SVM)

The support vector machine (SVM) classifier, which is supervised learning, one of the most accurate and robust algorithms in data collection and analyze data for classification and regression analysis. The SVM algorithm was developed by Cortes and Vapnik in 1995 [16] to classify data that were linearly separable and later generalized to nonlinear states. When using SVM training, data are categorized into two phases of train and test sets. and to validate the data, cross-validation techniques such as k-fold, holdout, or leave-n-out training methods are applied.

In addition to performing linear classification, SVMs can efficiently occur a non-linear classification using what is called the kernel trick, implicitly mapping their inputs into high-dimensional feature spaces [17].

3.2. Random Forest (RF)

Random forest (RF) or random decision forests are an ensemble learning technique for classification and regression. The general machine learning method of random decision forests was first proposed by Ho in 1995 [18]. Random Forest is a supervised learning algorithm. It is used in classification and regression problems with random decision forests. The forest network structure he established is a collection of decision trees, often trained by the bagging method. The Bagging method is that a combination of learning models increases the overall result. The random forest forms multiple land trees and combines these trees for a more accurate and stable prediction. Random Forest adds additional randomness to the model as it grows trees. Instead of looking for the most important property when breaking a node apart, it looks for the best property among a random subset of properties. This results in a wide variety, which usually results in a better model. Thus, in a random forest, only a random subset of properties is considered by the algorithm for the division of a node. Instead of finding the best possible thresholds, the model creates decision trees using random thresholds for each individual property.

3.3. Convolution Neural Network. (CNN)

CNNs are a particular kind of deep learning algorithm [19] for most commonly applied to analyze visual imagery that give a better consequence than many other machine learning algorithms. CNNs are regularized versions of multilayer perceptron. A CNN include input layer, hidden layer and output layer. Hidden layer is provided that the better learning capability of CNN and can learn from the data. CNN is also a feedforward Neural Network with more hidden layers. Hidden layers comprise convolutional layers combined with pooling layers. CNN has the most important block that is convolutional layer. The input is a tensor. After passing through a convolutional layer, the data becomes abstracted to a feature map. Multilayer filters are applied for the output is given to batch of feature map that becomes the final output of the convolutional layer.

Convolution layer catch information about local dependencies or semantics in the regions of original data. Data and final output are masked by the

activation function. After the convolution process, a pooling layer transform the number of samples in each feature map and take the most important information. Pooling layers transform the size of data by compound the outputs of neuron bunch at one layer into a single neuron in the next layer. There are two common types of pooling in popular use: max and average. Max pooling uses the maximum value of each local cluster of neurons in the feature map, while average pooling takes the average value.

3.4 Convolution Neural Network-Gated Recurrent Unit (CNN-GRU)

Gated recurrent unit (GRU) is improved for that are solved the vanishing gradient problem which come from with standard recurrent neural networks (RNNs) by Cho et al. [19]. GRU is a variation of long short-term memory networks (LSTMs). The GRU is simpler than the LSTM since it has only two gates, which are reset gate and update gate. These gates are utilized for the purpose of evaluating which information is beneficial or not. GRU has two gates that are update and reset aforementioned before. The useful information is stored with the usage of update gate while useless information is forgotten by reset gate.

The hybrid CNN-GRU model contains the best advantages of the GRU model which can be processed time sequence data and the advantages of the CNN model which is ideal for handling high dimensional data and feature extraction process. The architecture of the proposed GRU-CNN hybrid neural networks consists of structured GRU module and a CNN module. The inputs are fire and forest images data collected from web scraping while the outputs are the prediction of the is fire or non-fire. The CNN module uses local connection and shared weights to directly extract local features from the images matrixes data and obtain effective representation through the convolution layer and pooling layer. On the other hand, the purpose of the GRU module is to prevent the long-term dependency. In this way, the GRU module learns useful information in the historical data for a long period through the memory cell, and the useless information is forgotten by the forget gate. The inputs of GRU module are time sequence data; the GRU module includes many gated recurrent units, and the outputs of all these gated recurrent units are connected with the fully connected layer. Finally, the load predicting results can be obtained by calculating the mean value of all neurons in the fully connected layers.

3.5. Convolutional Neural Network-Long Shor-Term Memory (CNN-LSTM)

Long short-term memory networks (LSTMs) is an extended version of the recurrent neural networks (RNNs) architecture [17]. Unlike forward-fed neural networks, LSTM has feedback connections. These connections can flow information to the next neuron with the help of gates, or this information can be considered unnecessary and forgotten. An ordinary LSTM unit consists of a cell, an entrance gate, an exit gate and a forget gate. The cell remembers values at arbitrary intervals of time, and these three gates regulate the flow of information entering and exiting the cell. The performance of LSTMs is very poor compared to other deep learning algorithms such as CNNs in computer vision or image classification problems [20]. For this reason, hybrid models of LSTMs are evaluated to enhance the classification success in these fields [21]. Due to the characteristics of CNN and LSTM, the combination of advantages of CNN and LSTM is presented as a hybrid model. In this study, we also employ a hybrid deep learning methodology by integrating CNN and LSTM techniques. Two layers of CNN are utilized to ensure the correlation and effective extraction of multidimensional data. The feature sequence from the CNN layer is considered as the input for LSTM. Finally, the time dependencies are also extracted in the LSTM layer.

3.6. Faster Recurrent-Convolutional Neural Network (Faster R-CNN)

Faster R-CNN is model of R-CNN technology. The model is improved by Girshick et al [22]. A Faster R-CNN object detection network is composed of a feature extraction network which is typically a pretrained CNN. This is then followed by two subnetworks which are trainable. The first is a Region Proposal Network (RPN), which is, as its name suggests, used to generate object proposals and the second is used to predict the actual class of the object. So, the primary differentiator for Faster R-CNN is the RPN which is inserted after the last convolutional layer. This is trained to produce region proposals directly without the need for any external mechanism like selective search. Then, region of interest (ROI) pooling and an upstream classifier and bounding box regressor similar to Fast R-CNN are employed for the purpose of detecting fire at outdoor. We also use ROI pooling and an upstream classifier and bounding box regressor similar to Fast R-CNN.

3.6. Single Shot Detector (SSD)

The SSD model is a model used in object detection, such as the Faster R-CNN model. In contrast to the R-CNN architecture, the SSD model performs these

operations at the same time, while the region specified in the networks and these regions are connected to the networks respectively. This feature allows you to achieve faster results than the Faster R-CNN model of the SSD model. The input image is to the SSD model as in other models. It passes through convolutional nerve layers. The dimensions of these layers are different. In this way, different feature maps of the image are extracted. A certain number of rectangles are obtained using a 3x3 convolutional filter on maps. SSD divides the image as grids, and each grid cell responsible for detecting objects in that region of the image [23].

4. Proposed Framework

In this work, the comprehensive analysis of forest fire detection is proposed by employing deep and hybrid deep learning models, conventional machine learning algorithms, and object detection algorithms. For this purpose, data collection procedure is performed as a first step. The fire image data used in this study is gathered from Google images, Shutterstock, Getty Images websites by data scraping method. The pages of these websites are created with text-based markup languages. The markup language helps to define the structure of arguments that a web page contains. Because there are universal components and tags for embedded data on the website, it allows us to get the information that web breakers need into the program. In this work, a bot is constructed for the purpose of finding the image data addresses inside the website, and taking a screenshot of each image using Selenium library written in Python programming language. In this way, by opening a web browser with the help of a driver that will be installed on the computer, all operations that can be performed in a web browser are performed with the help of a program that conducts Python codes. Another method of scraping data is the usage of Beautiful Soup library, is a powerful and fast library built for processing HTML or XML files. On the web page that hosts the image data, the keyword that will allow to find the image cluster data to search is entered into the program. By parsing the HTML codes in the source with this module, it downloads only the source addresses of the target specified fields. As a result of scraping data, two datasets are gathered. The first one (DS1) covers 2,360 forest fire and 2,400 forest images. Second one (DS2) contains two categories 5,000 forest fire and 5,000 only forest images. After data collection, images are preprocessed by using grayscale and resize methods for both datasets. After that, dataset is ready to model for the purpose of detecting forest fire. For this purpose, support vector machines (SVMs) and

random forest (RF) are evaluated as conventional machine learning algorithms while Convolutional Neural Networks (CNNs), Convolutional Gated Recurrent Unit (CNN-GRU), and Convolutional Neural Network-Long Shor-Term Memory (CNN-LSTM) are assessed as deep end hybrid deep learning techniques. In addition, the effect of object detection techniques is also observed by employing Faster Recurrent-Convolutional Neural Network (Faster R-CNN) and Single Shot Detector (SSD) methods. As a result of extensive experiments, the final decision of the forest fire detection is determined among all techniques. The flowchart of the proposed framework is presented in Figure 1. As seen in in Figure 1, data collection step is carried out by gathering images from Google images, Shutterstock, Getty Images websites as a first step. Then, images are classified as forest, and forest fire. After applying grayscale and resizing preprocessing stages, classification task is performed using SVM, RF, CNN, CNN-GRU, CNN-LSTM techniques. In addition to classification models, SSD and Faster R-CNN are employed as object detection models. As a final decision, CNN outperforms others among classification techniques while SSD performs well when compared to the Faster R-CNN.

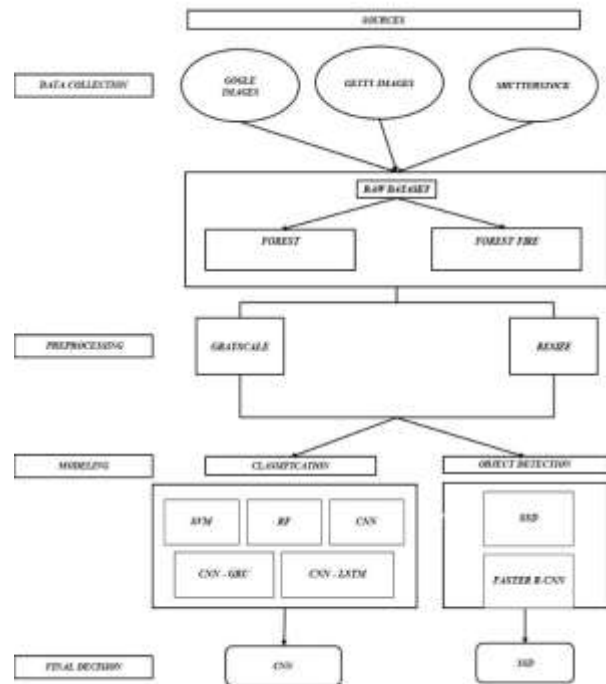***Figure 1****. The flowchart of the proposed framework*

In this part, parameter details of models are explained. Support vector machines (SVMs) that are machine algorithm, are used kernel function parameters, that represents the similarity of vectors (training samples) in a feature space over polynomials of the original variables, allowing learning of non-linear models [24]. Our model is

non-linear models that is so we are used polynomial kernel in SVM model. Other parameter is probability. One standard way to obtain a "probability" out of an SVM is to use Platt scaling, which is available in many decent SVM implementations. In the binary case, the probabilities are calibrated using Platt scaling: logistic regression on the SVM's scores, fit by an additional cross-validation on the training data. Random forest is a meta estimator that fits a number of decision tree classifiers on various sub-samples of the dataset and uses averaging to improve the predictive accuracy and control over-fitting. The sub-sample size is controlled with the max_samples parameter, otherwise the whole dataset is used to build each tree. Our model is used default value. Convolution neural network (CNN) model is deep learning algorithm that contains many parameters of learning models. The convolution layer is the core building block of a convolutional network that does most of the computational heavy lifting. The convolution layer's parameters consist of a set of learnable filters. Every filter is small spatially (along width and height), but extends through the full depth of the input volume. During the forward pass, we slide (more precisely, convolve) each filter across the width and height of the input volume and compute dot products between the entries of the filter and the input at any position. As we slide the filter over the width and height of the input volume, we will produce a 2-dimensional activation map that gives the responses of that filter at every spatial position.

Intuitively, the network will learn filters that activate when they see some type of visual feature such as an edge of some orientation or a blotch of some color on the first layer, or eventually entire honeycomb or wheel-like patterns on higher layers of the network. Convolutional networks may include local and global pooling layers along with traditional convolutional layers. Pooling layers decrease the size of data by combining the outputs of neuron bunch at one layer into a single neuron in the next layer. Local pooling combines small bunches, tiling sizes such as 2 x 2 which is employed in this work, are commonly used. Global pooling actions on all the neurons of the feature map. There are two common types of pooling in popular use: max and average. Max pooling uses the maximum value of each local cluster of neurons in the feature map, while average pooling takes the average value. Our model is used max pooling layer. Flatten layers for are used, neural networks retrieve input data from a one-dimensional array. The data in this neural network is a one-dimensional array of matrices from the convolutional and pooling layer [20].

Until this part, parameters of convolutional neural networks are mentioned in hybrid models (CNN-LSTM, CNN-GRU), all the parameters mentioned at the top are used in common. From here on, the parameters used in all general models are mentioned. The batch size is a number of samples processed before the model is updated. Batch size are chosen 32 for CNN, 8 for hybrid deep learning algorithms and 4 for object detection models. The number of epochs is the number of complete passes through the training dataset. Activation functions are used to get the output of node. Epoch value is changeable for every models. Epoch size is set to 20 for CNN, 50 for hybrid deep models, and 20,000 for object detection models. The resulting values range between 0 to 1 or -1 to 1. We employed ReLU activation function. We use loss function is Binary cross entropy. Adam is used optimizer for method of machine learning. Parameters that are chosen above were first studied with two different data set sizes and their results were compared. In order to see which hyper parameter variable the model receives the best result, different combinations of the parameters convolution layer number, the number of neurons of the hidden layer and the number of dense layers were tried and the results of the model training criteria were obtained. The parameter values are selected because the best classification results are obtained. The result is argued section 5.

Python 3.7 version is employed in the experiments. Furthermore, pillow, lxml, Tensorboard, OpenCV, TensorFlow, NumPy and Scikit-Learn libraries are integrated into the system for use in the workspace through Anaconda. TensorFlow contains objects detection API (Faster R-CNN, SSD), machine learning tools (Dense, Layer, Sequential) that's so our models are used TensorFlow for machine learning applications. It is a library for the Python programming language, adding support for large, multidimensional arrays and matrices, as well as a large collection of high-level mathematical functions to work with in these arrays. It is used to translate images into tensors. Scikit-learn is a free software machine learning library for the Python programming language. It features various classification, regression and clustering algorithms including support vector machines, random forests and is designed to interoperate with the Python numerical and scientific libraries NumPy and SciPy. Scikit-learn is used for our models that SVM and random forest classifier. Python Imaging Library is a free and open-source additional library for the Python programming language that adds support for opening, manipulating, and saving many different image file formats. When data of images are downloaded, opened image and saved to repository for used Pillow library. Lxml is a Python library which allows for easy handling of XML and HTML files, and can also be used for web scraping. When

our dataset is collected with web scraping, the library is worked with collected images on websites. Tensorboard is part of the TensorFlow. Tensorboard is used to analyze model of machine learning algorithms. All experiments are performed on PyCharm version 2020.3.5, Python version 3.7.0 and PC requirements that have Intel (R) Core (TM) i5-7200U CPU @ 2.50GHz 2.71 GHz process unit and NVIDIA GeForce 940MX graphic card in Windows 10 operation system.

5. Experiment Results

In this section, comprehensive experiments are carried out in order to detect forest fire using conventional machine learning algorithms, object detection techniques, deep and hybrid deep learning models. Accuracy (AC), f-measure (FM), precision (PR), mean average precision (mAP), and recall (RC) are employed as evaluation metrics to demonstrate the performance of the models. To calculate evaluation metrics for each model, the number of true-positive (TP), true-negative (TN), false-positive (FP), and false-negative (FN) values are obtained using confusion matrix. The TP refers to the number of operations extracted from the result of the fire by the model for visual data that actually contains the fire in the sample space collected within the scope of the study. TN is the number of visual data that does not actually contain a fire image and is determined by the model to contain no fire. FP refers to the number of visual data that the model classifies as if it were containing fire, although it does not actually contain fire data. FN refers to the number of visual data that is classified as if it does not contain fire data on the model side, even though it actually contains fire data. The ratio of the number of data that a model can classify as false when false and true when true to the total number of data gives the accuracy value given in equation 1.

$$Accuracy = \frac{TP+TN}{TP+NP+TN+FN} \qquad (1)$$

Precision gives the ratio of correctly predicted positive observation results to total positive estimates, and the power of negative interpretation gives the ratio of correctly predicted negative observation results to total negative estimates. The formula should be given as in equation 2.

$$Precision = \frac{TP}{TP+NP} \qquad (2)$$

Recall is used to measure the precision of the model. It gives the ratio of correctly predicted positive estimates to the number of all images that are actually correct (containing fire) given in equation 3.

$$Recall = \frac{TP}{TP+FN} \qquad (3)$$

F-measure is a value obtained as a result of the weighted ratio of positive interpretive strength and sensitivity values. Both false-positive and false-negative values are taken into account when calculating the F-measure. When the distribution of classes is not balanced, it gives more realistic results compared to the total accuracy criterion when measuring the success of the model. The formula should be given as in equation 4.

$$F - measure = \frac{2*Recall*Precision}{Recall+Precision} \qquad (4)$$

Intersection over Union (IoU) is defined as the area of the intersection divided by the area of the union of a predicted bounding box (B_p) and a ground-truth box (B_{gt}). Formula is presented in equation 5.

$$IOU = \frac{area(B_p \cap B_{gt})}{area(B_p \cup B_{gt})} \qquad (5)$$

To observe how the hyperparameters effect the performance of the system, different combinations are tested such as the number of convolution layer, the number of neurons in the hidden layers and dense layer, The best performance result is determined to construct the proposed model. In the experiments, dataset is divided into 70% as training and remaining is test.

The following abbreviations are used in the tables: AC: Accuracy, FM: F-measure, PR: Precision, RC: Recall, SVM: Support vector machine, RF: Random Forest, CNN: Convolutional neural network, CNN-GRU: Convolution Neural Network-Gated Recurrent Unit, CNN-LSTM: Convolutional neural network-long short-term memory, SSD: Single shot detector, Faster R-CNN: Faster recurrent-convolutional neural network, Avg: Average. The best results are obtained for each dataset in the Table 1 and Table 2 after experiments of hyperparameter tuning. The best performance results are also demonstrated in boldface in all tables. In Table 1, the performance results of all classification models according to evaluation metrics in the first dataset (DS1) are demonstrated. As it is clearly seen that in Table 1, convolutional neural network model outperforms other models with 98.32% of accuracy result.

Table 1. *Classification performance results of each method in terms of evaluation metrics on DS1.*

DS1	Evaluation Metrics			
Models	AC	FM	PR	RC
SVM	72.75	75.86	78.22	83.26

RF	80.26	81.22	83.17	84.35
CNN	98.32	98.12	98.30	98.34
CNN-GRU	53.08	66.34	34.66	66.21
CNN-LSTM	53.45	30.15	15.24	24.68
Avg.	71.24	70.15	62.18	71.96

It is followed by RF with 80.26%, SVM with 72.24 %, CNN-GRU with 53.45%, and CNN-LSTM with 53.08% of accuracy results. Although the RF is the model with the second-best classification ability, it cannot be said to be competitive due to nearly an 18% accuracy difference between them compared to CNN. As another result of Table 1, hybrid deep learning models exhibit poor performance with approximately 53.08% of accuracy in the image classification task for DS1, both compared to traditional machine learning techniques and CNN as a deep learning model.

In Table 2, the performance results of all classification models according to evaluation metrics in the second dataset (DS2) are demonstrated.

Table 2. Classification performance results of each method in terms of evaluation metrics on DS2.

DS2	Evaluation Metrics			
Models	AC	FM	PR	RC
SVM	75.29	78.48	70.29	89.15
RF	81.45	83.08	78.49	88.66
CNN	99.32	99.32	99.22	99.42
CNN-GRU	55.11	52.26	46.48	57.78
CNN-LSTM	54.73	34.25	17.48	37.78
Avg	73.35	69.52	62.46	74.18

As it is obviously observed that in Table 2, convolutional neural network model outperforms other models with 99.32% of accuracy result. It is followed by RF with 81.45%, SVM with 75.29%, CNN-GRU with 55.11%, and CNN-LSTM with 54.15% of accuracy results. Although the RF is the second-best classification technique, RF is not competitive because of about an 18% accuracy decrement when compared to CNN method. As another result of Table 2, hybrid deep learning techniques present the poorest classification success with approximately 54.15% of accuracy for CNN-LSTM and 55.11% of accuracy for CNN-GRU in DS2, both compared to conventional machine learning techniques and CNN model. The classification performance of models is ordered as: CNN> RF> SVM> CNN-GRU> CNN-LSTM.

When we compare Table 1 and Table 2 in terms of datasets, there is no remarkable change in accuracy for the CNN model when the total number of data increases. On the other hand, the traditional machine learning models exhibit an enhancement in accuracy values of nearly 1% for the RF, about 3% for the

SVM model, and almost 2% and roughly 1 for the CNN-GRU and CNN-LSTM models when the number of data increases. In addition, when the average accuracy value is considered in Table 1 and Table 2, an increase of almost 2% is also noticeable. Experiment results demonstrate that the utilization of CNN model for detection of forest fire significantly contributes to classification success of the system. For this reason, experiments are carried out on detailed parameter settings of CNN model as a next step. Table 3 and Table 4 present detailed parameter experiments for DS1 and DS2, respectively. The parameters employed in the experiments are the number convolution layer, the number of neurons and dense layer. In order to ensure the best scores of CNN model, different combinations are tested by varying epoch sizes. Epoch size is arranged as 20 for CNN and 50 for hybrid deep models, 32 batch sizes for CNN and 8 batch sizes for hybrid deep models, the number of convolution layer, the number of neurons contained in each layer, and the number of dense layers. The following abbreviations are used in the Table 3 and Table 4: CNV: The number of convolution layer, ND: The number of neurons contained in each layer, DNS: the number of dense layers.

Table 3. Classification performance results of each parameter combination in terms of evaluation metrics on DS1.

CNN	Evaluation Metrics			
Parameters	AC	FM	PR	RC
2 CNV-32 ND-1 DNS	98.32	98.12	98.30	98.34
2 CONV-32 ND-2 DNS	97.26	90.79	90.79	90.79
2 CNV-64 ND-1 DNS	97.26	97.26	97.26	98.26
2 CNV-64 ND-2 DNS	95.29	85.89	80.45	92.28
3 CNV-32 ND-1 DNS	90.42	95.08	93.47	97.74
3 CNV-32 ND-2 DNS	93.13	94.10	94.15	94.13
3 CNV-64 ND-1 DNS	84.46	95.19	93.73	98.19
3 CNV-64 ND-2 DNS	93.54	95.46	98.31	94.46

In Table 3, the combination of 2 convolution layer, 32 nodes, and 1 dense layer exhibits the best classification success with 98.32% of accuracy. When the number of dense layers and convolution layers are set to 1, and 2, respectively, the only change is observed in number of nodes. When the number of nodes increases from 32 to 64, the

performance is decreased nearly 1%. If the number of node and dense layers are adjusted as 32 and, 1, the number of convolutions varies to 3 from 2, which causes approximately 8% decrement in classification accuracy. When the number convolution layers, nodes, and dense layers are set to 3, 64, and 1, the fire detection system exhibits the poorest classification success with 84.15% of accuracy. As a result of Table 3 and Table 4, the raise of number of convolution layer and nodes affect the classification performance of the system, negatively. Finally, CNN experiments are carried out by setting the number of convolution layer, nodes, and dense layer as 2, 32, and 1, respectively for DS1 and DS2. In Table 4, classification results of each parameter combination in terms of evaluation metrics on DS2 are presented. Similar to Table 3, the combination of 2 convolution layer, 32 nodes, and 2 dense layers exhibits the best classification success with 99.32 % of accuracy. Although there is a modification in the number of nodes and hidden layers, no significant increase or decrease in classification performance is observed. However, the increase in the number of convolution layers caused a decrease in classification performance of about 5%.

Table 4. *Classification performance results of each parameter combination in terms of evaluation metrics on DS2.*

CNN	Evaluation Metrics			
Parameters	AC	FM	PR	RC
2 CNV-32 ND-1 DNS	99.16	98.60	99.52	98.61
2 CNV-32 ND-2 DNS	99.32	99.32	99.22	99.42
2 CNV-64 ND-1 DNS	98.96	99.41	99.34	99.16
2 CNV-64 ND-2 DNS	99.46	99.42	99.49	99.83
3 CNV-32 ND-1 DNS	96.59	95.19	95.24	96.81
3 CNV-32 ND-2 DNS	94.26	94.49	94.34	93.28
3 CNV-64 ND-1 DNS	95.76	96.64	97.57	95.19
3 CNV-64 ND-2 DNS	97.78	96.15	97.42	97.26

In addition to classification task in order to detect forest fire, object detection techniques are also evaluated. For this purpose, SSD and Faster R-CNN models are performed in the experiments. In Table 5, performance results of object detection techniques are presented in terms of evaluation metrics. The mAP metric compares the ground-truth bounding box to the detected box and returns a score. The results demonstrated in Table 5 are ensured

employing 1,605 fire images with 300*300 size. Test data contains 232 fire images and train data has 1,379 fire images. Common Objects in Context dataset (MS COCO), which contains 80k training images ("2014 train") and 40k validation images ("2014 val") is released by Microsoft. There is an associated MS COCO challenge with an evaluation metric, that averages mAP when is used calculate object detection accuracy over different IoU thresholds, from 0.5 to 0.95. This emphasizes a significantly larger emphasis on localization compared to COCO metrics. Every model has a performance number for training dataset. When Faster R-CNN model is trained on the dataset, the result of mAP is lower than 28%. Actually, this means that the Faster R-CNN model gives result of mAP score 13.36% for 0.5 intersection on unit (IOU). The same dataset is also trained on other object model single shot detector (SSD). The experiment result shows that the usage of SSD technique outperforms Faster R-CNN with 22.2% of mAP. Furthermore, precision of SSD model performs better than Faster R-CNN method with 19.26%. Figure 2 demonstrates the fire detection results of SSD model on test images.

Table 5. *Performance results of object detection techniques in terms of evaluation metrics.*

Models	Evaluation Metrics		
	mAP	Precision	Recall
SSD	22.20	19.26	43.00
FasterR-CNN	13.36	14.22	43.22

Figure 2. *SSD fire detection model on test images.*

In [25], authors propose multi-scale prediction for fire detection utilizing convolutional neural network. 97.89% of F-measure score is reported while our study demonstrates 98.12% of F-score. In [26], convolutional neural network (CNN) is proposed to detect fire by classifying both fire and smoke in videos. The training procedure is performed with the videos including both fire and smoke. The experiment results indicate that the model used in the study is able to classify the fire, smoke and fire with smoke with a recognition rate of up to 94%, 95% and 93%, respectively. In [27], Saponara et. al present real-time video fire/smoke detection system

employing YOLOv2 convolutional neural network. Authors employ a large scale of fire/smoke and negative videos in different environments, both indoor (e.g., a railway carriage, container, bus wagon, or home/office) and outdoor (e.g., storage or parking area). They report that the achieved experimental results show that the proposed system is suitable real-time video-surveillance system for fire/smoke detection with 96.02% of accuracy that surpasses of our object detection models because of using different model and different experiment settings, and datasets.

6. Conclusion and Discussion

Forest fire detection is a very challenging task in the area of object detection. To overcome the problem of fire detection in outdoors, deep learning and conventional machine learning based computer vision techniques are utilized to determine the fire detection when indoor fire detection systems are not capable. In this work, we present a detailed analysis of forest fire detection employing conventional machine learning algorithms, object detection techniques, deep and hybrid deep learning methods. To the best of our knowledge, it is the very first attempt to assess forest fire in such a comprehensive way in terms of six different techniques and two different size data sets. In this aspect, this work contributes to the literature in terms of analyzing various classification and object detection methods in more details that is not addressed before to detect forest fire. Extensive experiments show that convolutional neural networks outperform other techniques with 99.32% of accuracy result. As a future work, we intend to analyze the effects of transfer learning methodology on forest fire detection with large volumed datasets.

Author Statements:

- The authors declare that they have equal right on this paper.
- The authors declare that they have no known competing financial interests or personal relationships that could have appeared to influence the work reported in this paper.
- The authors declare that they have nobody or no-company to acknowledge.

References

[1] Den Breejen, E., Breuers, M., Cremer, F., Kemp, R., Roos, M., Schutte, K., De Vries, J. S. Autonomous forest fire detection Coimbra, Portugal: ADAI-Associacao para o Desenvolvimento da Aerodinamica Industrial. pp. 2003-2012, 1998.

[2] Thengade, A., Mishra, P., Kshatriya, R., Mhaskar, R., & Bodhe, P. Fire Detection Using Image Processing Using Raspberry PI.

[3] Kilimci, Z. H., Ganiz, M. C. Evaluation of classification models for language processing. International Symposium on Innovations in Intelligent SysTems and Applications (INISTA) (pp. 1-8). IEEE. 2015

[4] Deng, L., Hinton, G., Kingsbury, B. New types of deep neural network learning for speech recognition and related applications: An overview. In 2013 IEEE international conference on acoustics, speech and signal processing (pp. 8599-8603). IEEE. 2013

[5] Singh, S. P., Kumar, A., Darbari, H., Singh, L., Rastogi, A., Jain, S. Machine translation using deep learning: An overview. In 2017 international conference on computer, communications and electronics (comptelix) (pp. 162-167). IEEE. 2017

[6] Khondaker, A., Khandaker, A., Uddin, J. Computer Vision-based Early Fire Detection Using Enhanced Chromatic Segmentation and Optical Flow Analysis Technique. International Arab Journal of Information Technology, 17(6), 947-953.2020

[7] A. Rafiee, R. Dianat, M. Jamshidi, R. Tavakoli, and S. Abbaspour, Fire and smoke detection using wavelet analysis and disorder characteristics, ICCRD 2011 - 2011 3rd Int. Conf. Comput. Res. Dev., 3 262–265. 2011

[8] Mahmoud, M. A. I., Ren, H. Forest fire detection and identification using image processing and SVM. Journal of Information Processing Systems, 15(1), 159-168. 2019

[9] Sadewa, R. P., Irawan, B., Setianingsih, C. Fire detection using image processing techniques with convolutional neural networks. In 2019 International Seminar on Research of Information Technology and Intelligent Systems (ISRITI) (pp. 290-295). IEEE. 2019

[10] Sucuoğlu, H. S., Böğrekçi, İ., Demircioğlu, P. Real Time Fire Detection Using Faster R-CNN Model. International Journal of 3D Printing Technologies and Digital Industry, 3(3), 220-226. 2019

[11] Mwedzi, N. A., Nwulu, N. I., Gbadamosi, S. L. Machine Learning Applications for Fire Detection in a Residential Building. In 2019 IEEE 6th International Conference on Engineering Technologies and Applied Sciences (ICETAS) (pp. 1-4). IEEE. 2019

[12] Abid, F. A Survey of Machine Learning Algorithms Based Forest Fires Prediction and Detection Systems. Fire Technology, 57(2), 559-590. 2021

[13] Xu, R., Lin, H., Lu, K., Cao, L., Liu, Y. A Forest Fire Detection System Based on Ensemble Learning. Forests, 12(2), 217. 2021

[14] Pourghasemi, H. R., Gayen, A., Lasaponara, R., & Tiefenbacher, J. P. Application of learning vector quantization and different machine learning techniques to assessing forest fire influence factors and spatial modelling. Environmental research, 184, 109321.7. 2020

[15] Maksymiv, O., Rak, T., Peleshko, D. Real-time fire detection method combining AdaBoost, LBP and

convolutional neural network in video sequence. In 2017 14th International Conference the Experience of Designing and Application of CAD Systems in Microelectronics (CADSM) (pp. 351-353). IEEE. 2017

[16] Cortes, C., Vapnik, V. Support-vector networks. Machine learning, 20(3), 273-297. 1995

[17] Azarmdel, H., Jahanbakhshi, A., Mohtasebi, S. S., & Muñoz, A. R. Evaluation of image processing technique as an expert system in mulberry fruit grading based on ripeness level using artificial neural networks (ANNs) and support vector machine (SVM). Postharvest Biology and Technology, 166, 111201. 2020

[18] Ho, T. K. Random decision forests. In Proceedings of 3rd international conference on document analysis and recognition (Vol. 1, pp. 278-282). IEEE. 1995

[19] Cho, K., Van Merriënboer, B., Gulcehre, C., Bahdanau, D., Bougares, F., Schwenk, H., Bengio, Y. Learning phrase representations using RNN encoder-decoder for statistical machine translation. arXiv preprint arXiv:1406.1078. 2014

[20] Shashua, A. Introduction to machine learning: Class notes 67577. arXiv preprint arXiv:0904.3664. 2009

[21] https://cs231n.github.io/convolutional-networks/

[22] Nagrath, P., Jain, R., Madan, A., Arora, R., Kataria, P., & Hemanth, J. SSDMNV2: A real time DNN-based face mask detection system using single shot multibox detector and MobileNetV2. Sustainable cities and society, 66, 102692. 2021

[23] Ren, S., He, K., Girshick, R., Sun, J. Faster r-cnn: Towards real-time object detection with region proposal networks. arXiv preprint arXiv:1506.01497. 2015

[24] Hochreiter, S., Schmidhuber, J. Long short-term memory. Neural computation, 9(8), 1735-1780.

[25] Jeon, M., Choi, H. S., Lee, J., & Kang, M. (2021). Multi-scale prediction for fire detection using convolutional neural network. Fire Technology, 2021, 1-19. 1997

[26] Singh, A. R., Athisayamani, S., Narayanan, S. S., & Dhanasekaran, S. Fire detection by parallel classification of fire and smoke using convolutional neural network. In Computational Vision and Bio-Inspired Computing (pp. 95-105). Springer, Singapore. 2021

[27] Saponara, S., Elhanashi, A., & Gagliardi, A. Real-time video fire/smoke detection based on CNN in antifire surveillance systems. Journal of Real-Time Image Processing, 18(3), 889-900. 2021
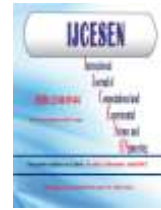
Investigation of Natural Occurring Radioactive Material Activity Level in Falluja-Anbar (Iraq)

Sabah FARHAN [1], Faez WAHEED[2*], Mohammed AL-DULAIMI [3]

[1]Renewable Energy Research Center/ University of ANBAR /Iraq
sabah.falahi@uoanbar.edu.iq **ORCID:** 0000-0001-8792-5695

[2] Iraqi Radioactive Sources Regulatory Authority (IRSRA)
***Corresponding Author Email** :faez_radiophysics@yahoo.com **ORCID:** 0000-0002-0003-0467

[3] Iraqi Radioactive Sources Regulatory Authority (IRSRA)
mjma1967@yahoo.com **ORCID:** 0000-0002-4611-3874

Abstract:

Radiation may be defined as the energy in the form of electromagnetic waves or particles that pass through space and even heavy dense materials. The radioactivity is a continuously decreasing quantity which is a function of the half-life of the responsible radionuclides. The natural sources of radiation came from terrestrial radionuclides which are widely distributed in the earth's crust.

Field radiological surveys were conducted by the GR-460 mobile detection system, the only mobile system in Iraq and the region. This system is dedicated to the radiological scanning process for large areas and in less time. The system is attached to a GPS satellite positioning device so that the measurement points are coupled with the spatial coordinates of the radiometric area.

In this study, the concentration of naturally occurring radioactive materials had been determined experimentally of AL-Falluja / Anbar Governorate- Iraq for (66) km^2 using GR-460 portable gamma spectrometer system. The results showed that the high level of uranium concentration (^{238}U) was 8.1 ppm in the industrial area, the low level was 0.1 ppm in most districts. The high level of Thorium (^{232}Th) concentration was 17.5 ppm and less than 0.1 ppm in most neighbourhoods are within Iraq's natural background.

1. Introduction

Radiation and radioactivity were discovered more than 100 years ago, this phenomenon of radioactivity occurs when energy from an atom is spontaneously released, ionizing radiation is part of nature and human activities in medicine, research, industry, energy production, and some special military applications [1 - 3].

The main source of radioactivity belongs to two classes; natural and man-made resources. The natural source of radiation comes from terrestrial radionuclides, terrestrial radionuclides are widely distributed in the earth's crust, and sources originate from cosmic rays. Other sources come from radiation and human activities related to the use of radioactive materials, where radionuclides can form in the environment [4 - 6].

Iraq needs to measure radioactivity and determine its rates on an ongoing basis due to the events of 2003, as well as the presence of many nuclear programs in the neighboring countries of Iraq. Therefore, radiological survey programs to determine the concentrations of radioactive isotopes such as uranium and thorium are important in normal cases because of the possibility of needing these results in emergency situations or when nuclear accidents happen [7].

Fallujah considered one of the districts that belong to the Anbar Governorate and is located near the capital, Baghdad, about 50 km from it. Radiological measurements had been done using the latest pertable spectroscopy systems to determine the concentration of ^{238}U and ^{232}Th in Fallujah.

2. Material and Methods

2.1. Material

The GR-460 detection system used is considered one of the advanced systems in the field of mobile radiological surveys. This system is characterized by high accuracy in conducting field measurements and recording data while specifying the coordinates of the measurement sites with extreme accuracy because it includes a GPS device [7, 8]. This system contains a gamma-ray detector kind NaI(Tl) and is characterized by its ability to measure radioactivity and radiation dose because it contains a spectra analyzer that contains 512 channels.

This system contains two NaI detectors with a size of (793 x 216 x 177 mm), this system capable of separating different energies and identifying the radioactive isotope [9, 10]. Figure 1 shows the layout of the measurement system. The system is installed inside a suitable car at a height of one meter above the ground, GR-460 detection system and the detectors attached to it are connected via dedicated cables. When starting to record field measurements, the wheel speed must be between (8 - 20 km/h) so that the detector can sense the signal and convert it into a reading known from the measuring device to the calculator attached to them. The detectors are calibrated to the radioactive source ^{137}Cs with radioactivity (0.25 μCi) before starting the field survey process [7, 11].

Figure 1. *Two sodium iodide detectors NaI (Tl) inside the radiological survey field vehicle*

2.2. Methods

Radiation investigation and measurements were made for areas belonging to Fallujah district (Table 1), whose area is estimated at 66 km^2, and the main roads and streets were chosen as paths for the implementation of these surveys, and the distance between two path is approximately 200m in some areas, and other areas the distance between one path and another is estimated at 80 - 250 m due to the

presence of some areas that are built in a random way and do not allow the organization of the path with equal distances, and the total paths that were conducted surveys were within 235 km as shown in the Figure 2.

3. Results and Discussions

Some areas were taken as main fixed points for measuring the concentrations of uranium and thorium as shown in Table 1, the results of the radiometric measurements were in ppm units for all the measurement points.
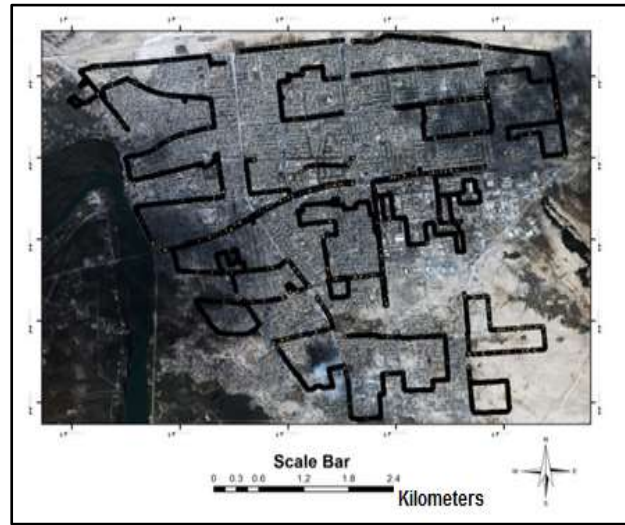

Figure 2. *The path of the measurements points in Faluja district*

Table 1. *The ^{238}U and ^{232}Th concentration in ppm unite of Fallujah district of Fallujah district*

Location (District)	^{238} U ppm					^{232}Th ppm		R/hμ	
	Average	Max	Min	Av	Max	Min	Av	Max	Min
Widows	2.6	7.2	0.1	5.7	12.5	0.2	4.0	5.4	3.1
Andalusia	2.4	5.9	0.1	4.8	14.7	0.1	3.3	4.3	2.7
Tamim	1.4	5.7	0.1	5.1	14.7	0.1	3.7	4.8	3.0
Golan	2.5	6.3	0.2	5.3	14.0	0.1	3.7	4.5	3.0
Green	2.6	6.2	0.1	5.6	14.8	0.2	3.9	5.3	3.2
Al-Resalla	2.8	7.9	0.1	5.4	16.7	0.1	4.0	5.8	2.7
Al-Salam	2.2	6.2	0.1	4.1	11.2	0.1	3.4	4.6	2.8
Police	2.2	6.1	0.1	4.2	12.1	0.1	3.4	4.4	2.6
Industrial	2.3	8.1	0.1	5.6	15.8	0.2	300	800	150
Officers	1.8	5.0	1.8	4.7	12.0	0.2	3.4	4.5	2.7
Qadisiyah	2.3	6.6	0.1	5.0	13.9	0.1	3.8	7.3	2.8
Al-Mu'tasim	2.7	6.5	0.1	5.5	17.5	0.1	3.9	6.7	2.9
Teachers	2.1	6.1	0.1	5.1	17.5	0.1	3.6	5.0	2.7
Mansour	2.6	6.4	0.2	5.3	16.6	0.2	3.8	5.5	2.7
Al Wahda	2.3	6.1	0.1	4.3	11.2	0.2	3.8	5.7	2.7
Yarmouk	2.6	6.4	0.2	5.8	14.8	0.1	3.9	5.2	2.9

The recorded data were fully analysed, the results of radiological measurements in Anbar Governorate\ Fallujah were as follows: The recorded natural

uranium ^{238}U concentration rates were (2.8 ppm) in Al-Resala neighbourhood and the lowest reading was 1.4 ppm in Al-Tameem neighborhood. The recorded natural thorium ^{232}Th concentration rates were the highest reading 5.8 ppm. In the Yarmouk neighbourhood and the lowest reading 4.1 ppm in the Al-Salam neighbourhood, all readings were within the limits of the rates of the natural radiation background of the environment of Iraq. See Figure 3 and Figure 4.
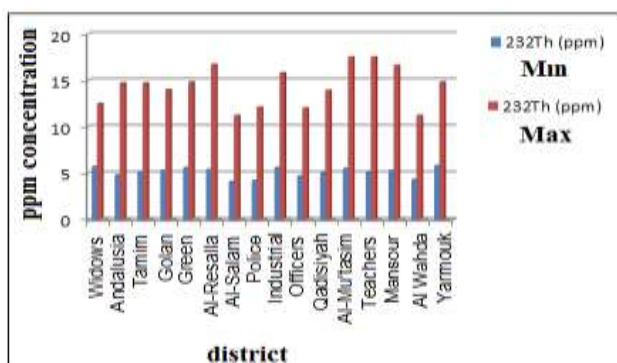

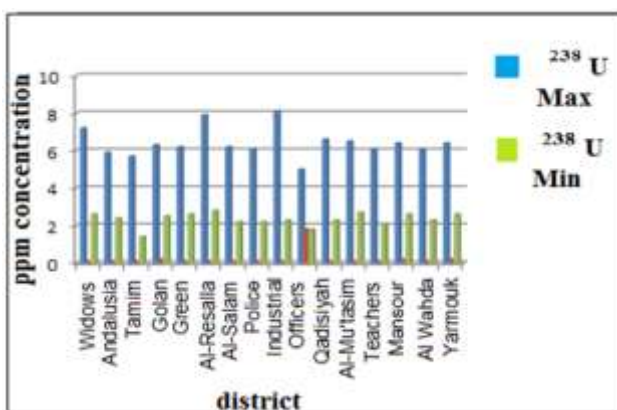***Figure 3.** The minimum and maximum concentration of ^{232}Th*

***Figure 4.** The minimum and maximum concentration of ^{238}U*

4. Conclusions

It is known that Iraq considered one with the normal natural radiological background as proven in the studies and investigations conducted in this field.

The results showed that all the radiological measurements of uranium and thorium were within the limits of the radioactive background of Iraq.

The radiation survey system kind GR-460 is considered one of the advanced systems for measuring radioactive isotope concentrations over large areas due to the ease of measurement and speed in analyzing and giving results.

Author Statements:

- The authors declare that they have equal right on this paper.
- The authors declare that they have no known competing financial interests or personal relationships that could have appeared to influence the work reported in this paper
- The authors acknowledge to "Iraqi radioactive sources regulatory authority" for support this work.

References

[1] Akyildirim, H., Waheed, F., Günoğlu, K., & Akkurt, İ. (2017). Investigation of Buildup Factor in Gamma-Ray Measurement. *Acta Physica Polonica A*, *132*(3), 1203-1206.

[2] Waheed, F., Q., Akyildirim, H., Günoğlu, K., Akkurt, İ., 2018. The Importance of the Buildup Factor for NaI(Tl) Detector System. 5[th]international Conference on Computational and Experimental Science and Engineering (ICCESEN-5), ISBN: 978-605-68728-0-8, 12-16 October 2018, Antalya-Turkey, 298-300. Available at: http://iccesen.org/uploads/2019/ICCESEN2019%20proceeding%20book%20V5.pdf

[3] Akkurt, I., & Tekin, H. O. (2020). Radiological parameters of bismuth oxide glasses using the Phy-X/PSD software. *Emerging Materials Research*, *9*(3), 1020-1027.

[4] Özseven, A., & Akkurt, İ. (2020). Evaluation of gross-alpha and gross-beta activity concentrations and assessment of excess lifetime cancer risk in waters of Eğirdir Lake, Turkey. *International Journal of Environmental Analytical Chemistry*, 1-13.

[5] WAHEED, F. Q. W. and AKKURT, İ., 2017. INVESTIGATION OF BUILDUP FACTOR IN γ–RAY MEASUREMENT. Available at: http://tez.sdu.edu.tr/Tezler/TF03802.pdf

[6] Eisenbud, M., & Gesell, T. F. (1997). *Environmental radioactivity from natural, industrial and military sources: from natural, industrial*.

[7] حيدر and محمد جاسم محمد, فائز قحطان وحيد, حسنين موسى جعفر يونس, 2015. معدل التعرض الاشعاعي في الهواء لمركز قضاء تكريت وناحية العلم محافظة صلاح الدين. *Journal of the college of basic education*.(علمي/89)*21* , Available at: https://www.iasj.net/iasj/article/101657

[8] Waheed, F. Q., AL-Kazzaz, H. H., AL-Aubaedy, S. D., & AL-Dulaimi, M. J. (2017). قياس التعرضات الاشعاعية لمنظومة الفحص بالاشعة المؤينة من نوع RapiScan-GaRDS. *Journal of Madenat Alelem University College*, *9*(1), 131-142. Available at: https://journal.mauc.edu.iq/index.php/JMAUC/article/view/103

[9] GR-460 Mobile Spectrometer System User Manual, part#31010-1 Rev 0, Software Version 1.0 (2005).

[10] Marouf, B. A., Mohamad, A. S., Taha, J. S., & Al-Haddad, I. K. (1992). Population doses from environmental gamma radiation in Iraq. *Health physics*, *62*(5), 443-444.

[11] عبير فنجان حدحود, محمد جاسم محمد, حسان شعبان خليل, & د. سلام طارق. (2018). معدل توزيع الجرعة الاشعاعية في محافظة الانبار قضاء القائم. Journal *of the college of basic education.*(علمي/101)*24*, Available at: https://www.iasj.net/iasj/article/151613

Research Article
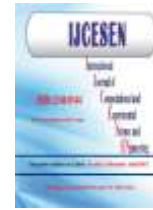
An Investigation on Radiation Shielding Properties of Borosilicate Glass Systems

Duygu Sen BAYKAL[1]*, Huseyin Ozan TEKIN[2], R. Burcu CAKIRLI[3]

[1]Istanbul University, Institute of Graduate Studies in Science and Engineering, Dep. of Physics, Istanbul-Turkey.
* **Corresponding Author** : duygu.sen@ogr.iu.edu.tr **ORCID:** 0000-0001-9833-9392

[2]Sharjah University, Department of Medical Diagnostic Imaging Program, 27272, United Arab Emirates (UAE).
tekin765@gmail.com **ORCID:**0000-0002-0997-3488

[3]Istanbul University, Department of Physics, 34134 Istanbul, Turkey.
rburcu@istanbul.edu.tr **ORCID:** 0000-0002-8400-1718

Abstract:

The aim of this research is to examine the radiation shielding properties of $5B_2O_3$-$40SiO_2$-$(55-x)Al_2O_3$-$xBaO$ (BSABa-x) (where x = 25, 28, 31 and, 34) lead-free glass systems, which are containing barium and aluminum oxide added to borosilicate glasses, with varying from 25 to 34 weight fractions. Shielding parameters, such as linear attenuation coefficients (LAC), mass attenuation coefficients (MAC), mean free path (MFP), effective atomic number (Z_{eff}), effective electron density (N_{eff}), half-value layer (HVL), tenth-value layer (TVL), effective atomic weight (A_{eff}), exposure buildup factors (EBF) and energy absorption buildup factors (EABF) enable us to obtain information about the radiation shielding power of composite glass material groups. Therefore, the mass attenuation coefficients (MAC), for the 0.015–15 MeV gamma-ray energies are obtained by using the Py-MLBUF online software to determine photon shielding parameters of BSABa-x glass systems. The results are shown that the glass system, which contains higher BaO concentration has higher mass attenuation coefficients. BSABa-34 glass has the highest MACs, ranging from 0.111 cm^2/g to 90.400 cm^2/g, while BSABa-25 glass has the lowest values, ranging from 0.099 cm^2/g to 69.000 cm^2/g. The BSABa-34 glass with the highest BaO contribution has the thinnest MFP and HVL values. In addition, photon buildup is minimized by adding BaO to the BSABa-x glasses. Accordingly, we can conclude that adding BaO to aluminum borosilicate glasses at increasing rates, improves nuclear radiation resistance properties.

1. Introduction

Radiation obtains benefit when used for diagnosis and treatment within certain dose limitations, but it can also cause to destructive biological effects. In addition to its natural level existing in nature, minimizing the harmful effects of radiation from artificial sources requires maximum protection. Shielding, one of the basic principles of protection, is defined as a material environment which radiation can absorb its energy as a result of the interaction. Radiation protection is provided by the use of materials which's shielding parameters are well known and pre-determined for this material

environment. Lead (Pb) is the material that has been widely used since ancient times for radiation protection due to the various advantages provided by its physical and chemical properties. With the developing technology, lead, which has been discovered to be a heavy metal by spectroscopic analysis, has a high density and therefore is in the heavy metals class. Thanks to this feature, it has been discovered that it is the best absorbent material environment when it interacts radiation energy, and it has been used for shielding and it continues to be widely used today [1-7] However, in addition to the advantages of lead, it also has important disadvantages such as the low material

strength, the difficulties it causes during its use, the cost, the lack of a transparent structure. Due to its widespread use, the structure of lead accumulated in the environment is not suitable for biodegradation, and therefore, with its increasing concentration, it causes a permanent threat to nature and living things by taking place in the environment. Almost all functions in human body can be affected by the toxic effects caused by lead through respiration, skin absorption, and digestion. These disadvantages of lead accelerated the search for materials that can be used as an alternative to traditional materials used for shielding [8-10]. Glass panes are important requirement where radiation is used, especially in nuclear facilities and hospitals. Glass materials used in these compartments must also have strong radiation attenuating features. Today, glass materials are doped with both lead and lighter heavy metals to increase their resistance to radiation. However, since these composite leaded glasses contain both toxic heavy metals and the level of transparency can not be achieved at the desired level. It has become an important need to develop lead-free glass materials that do not harm the environment and people, and also have more transparent structure [11-14]. Developing lead-free protective material is very important for the safe use of radiology rooms. The most important feature of the shielding material is the weakening of gamma photons which have very high ability to penetrate into the substance. This could only be accomplished by using materials that include elements with a high atomic number and hence a high density [15-20]. To determine the feasibility of using any glass sample as a photon shielding material, detailed studies are conducted to determine its physical properties, including linear attenuation coefficients (LAC), mass attenuation coefficients (MAC), mean free path (MFP), effective atomic number (Z_{eff}), effective electron density (Neff), half-value layer (HVL), tenth-value layer (TVL), effective atomic weight (Aeff), exposure buildup factors (EBF) and energy absorption buildup factors (EABF). When all of these parameters are established, we may recommend which materials or material classes can provide the best defense. The mass attenuation coefficient (μ_m) is one of these parameters; it indicates the amount of photons scattered or absorbed by the interacting material. The mass attenuation coefficient is regarded as a fundamental parameter that can be used to calculate additional shielding parameters [19-23]. Additionally, the effective atomic number (Z_{eff}) is a critical parameter for interpreting the attenuation efficiency

of gamma photons by a multi-element substance. Z_{eff} indicates the protective material's efficiency; a higher Z_{eff} value indicates that photons are more likely to be absorbed due to the presence of more electrons to communicate with. Additionally, since the mean free path (MFP) is an energy-dependent quantity, it allows the determination of the distance traveled by a photon in a sample prior to any interaction [23-26]. The mass attenuation coefficients (MAC) for 0.015–15 MeV gamma-ray energies are determined using the Py-MLBUF online software in order to determine the photon shielding parameters of the BSABa-x glass systems tested in this analysis. MAC values are used to calculate various shielding parameters for BSABa-x glasses, including the half value layer (HVL), energy buildup and energy absorption buildup factors (EBF and EABF), and mean free path (MFP). The Py-MLBUF software has been used extensively to investigate the photon and neutron shielding properties of glasses [27]. Numerous experiments have been conducted to determine the mass attenuation coefficient for various glass systems, including borosilicate and heavy metal oxide glasses [28-33]. While the majority of these studies analyze the radiation shielding parameters of various glasses at medium and high energy levels, there are very few studies that examine the gamma and neutron radiation shielding parameters of various glass systems at medical diagnostic energies [34-37]. Therefore, this study include radiation shielding parameters of the $5B_2O_3$ - $40SiO_2$ - $(55-x) Al_2O_3$ - $xBaO$ (BSABa-x), (where x = 25, 28, 31 and 34 (with these additive rates theoretical ρ range from 3.798 to 3.957 g/cm³)) glass systems, which are containing barium and aluminum oxide added to borosilicate glasses and theoretical density range from 3.798 to 3.957 g/cm³, in medical diagnosis energy scales.

2. Materials and Methods
2.1 Shielding Parameters

As a measure of the absorption of a photon by the material, the linear attenuation coefficients (LAC) of the materials are examined [25]. The LAC, which is a quantity that needs to be investigated in many materials to be effectively protected from radiation, gives the probability of any interaction per unit length of a photon, and it expresses the total probability of occurrence of photoelectric events, Compton scattering, pair formation events. The LAC is expressed as [36-38];

$$\mu = \frac{In[I/I_0]}{t} \tag{1}$$

(where I and I_0 show intensities of the incident and attenuated gamma rays, respectively, and t denotes the mass thickness of the sample.)

and the mass attenuation coefficient (MAC) is calculated by dividing the LAC by the specific gravity of the material. The MAC gives the rate of attenuation of the beam per unit mass and is expressed as [36-38];

$$\mu_m = \frac{\mu}{\rho} \qquad (2)$$

(where μ shows the linear attenuation coefficient (expressed in cm^{-1}) defines a measure of the possibility of photon interaction when radiation passes through a target material, depending on the thickness of the material, where μm shows mass attenuation coefficient, and ρ shows the density of the material.)

The appropriate material thickness that causes the intensity of radiation passing through a target to decrease to half intensity by interacting with the material is also called the half-value layer (HVL) and is expressed with the formula [36-38];

$$HVL = \frac{In2}{\mu} \qquad (3)$$

The tenth-value layer (TVL) is defined as the material depth value that allows the incoming radiation intensity to decrease to one-tenth value and is formulated in the form of [36-38];

$$TVL = \frac{In10}{\mu} \qquad (4)$$

The mean free path (MFP), another of the shielding parameters, is defined by the following formula as the distance traveled by a particle before possible collisions with other particles [36-38].

$$mfp = \frac{1}{\mu} \qquad (5)$$

The effective atomic number (Z_{eff}) is a parameter that has any real constant value for a given material, which gives the common behavior of electrons in the interaction of materials with radiation [36-38].

$$Z_{eff} = \frac{\sum_i f_i A_i (\mu_\rho)_i}{\sum_j f_j \frac{A_j}{Z_j}(\mu_\rho)_j} \qquad (6)$$

Also, there is a linear relationship between the effective atomic number (N_{eff}) and the electron density defined by the following expression [30-31].

$$N_{eff} = N_A \frac{Z_{eff}}{<A_{eff}>} \text{ (electrons/g)} \qquad (7)$$

(where N_A is Avogadro constant and A_{eff} is the effective atomic mass value, also known as the ratio of atomic weight to total atomic number [36-38].)

The buildup factor is a factor that includes the response of non-colliding photons to add the participation of scattered photons. Exposure Buildup factor (EBF) is a parameter related to the amount of absorption or stored energy in the air, and this parameter determines the extent of the interaction that may occur in the air, between the source and the detector. Energy absorption build up factor (EABF) is a parameter related to the amount of energy absorbed in the substance with which the radiation interacts in different substances [36-45].

2.2 Py-MLBUF

To investigate the gamma-ray shielding parameters of the materials, a thorough understanding of the various gamma-ray shielding parameters (GSP) is needed. By measuring gamma-ray shielding parameters, the computer plays an important role in this form of study. [46]. The storage and processing of useful radioactive materials in radiology establishments has become a critical issue as nuclear technology and safety requirements have advanced. A gamma-ray shielding enclosure (GSE) must be designed with suitable materials to protect the environment from harmful self-emitting ionizing radiations from radioactive materials. Shielding is one of the most effective ways to reduce the harmful effects of ionizing radiation on living tissues. Shield designers should investigate the suitability of materials using gamma-ray shielding parameters to choose a suitable material for the GSE. Py-MLBUF is the name of the platform's computer code, which is written in Python and calculates gamma-ray shielding parameters in the energy range of 0.015–15MeV [47-49].

Table 1. *The weight fractions and theoretical densities of* $5B_2O_3$-$40SiO_2$-$(55-x)Al_2O_3$-$xBaO$ (x=25, 28, 31 and 34) *glass systems.*

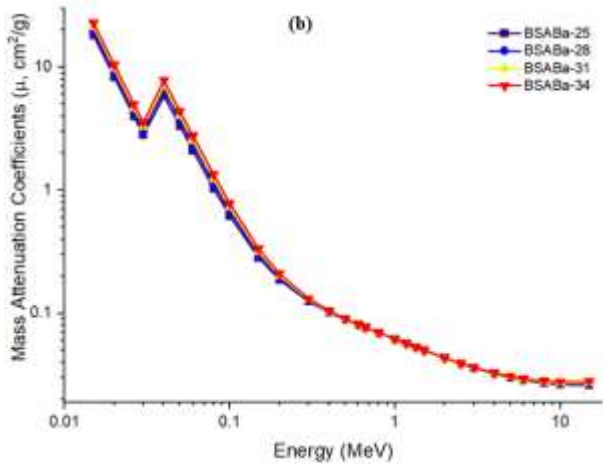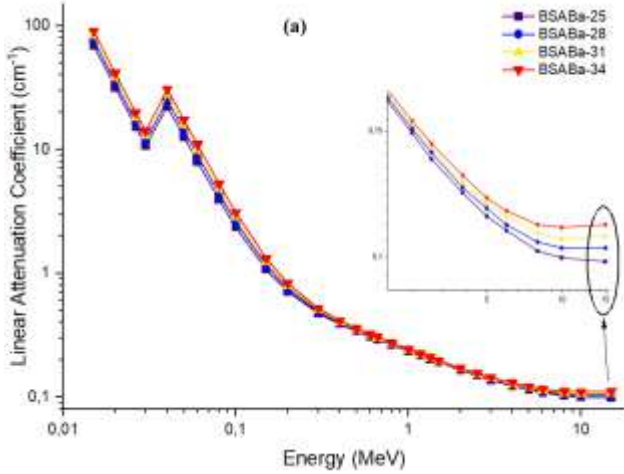| Sample Code	B	Si	Al	Ba	O	Density (g/cm³)
BSABa25	0.016	0.187	0.159	0.224	0.415	3.798
BSABa28	0.016	0.187	0.143	0.251	0.404	3.851
BSABa31	0.016	0.187	0.127	0.278	0.393	3.904
BSABa34	0.016	0.187	0.111	0.305	0.382	3.957

Figure 1. *(a) Variation of linear attenuation coefficients (LAC) (b) mass attenuation coefficients (MAC) versus photon energy for BSBa-x (x=25, 28, 31 and 34) glasses.*
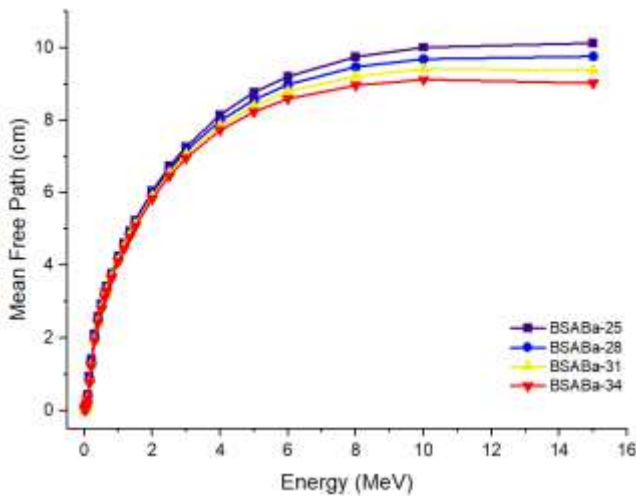

Figure 2. *Variations of mean free path (MFP) with photon energy for for BSBa-x (x=25, 28, 31, 34) glasses.*
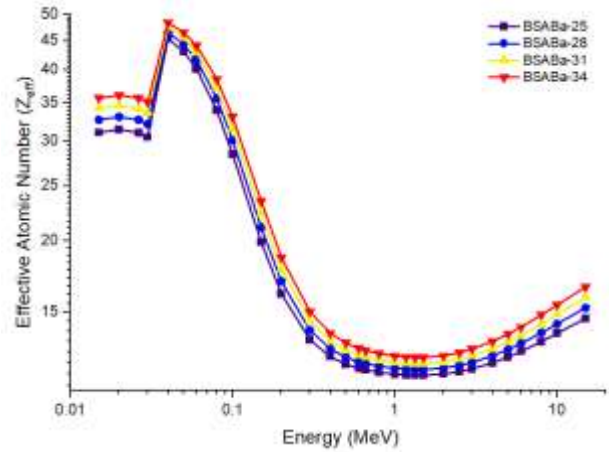

Figure 3. *Effective atomic number (Z_{eff}) with photon energy for BSBa-x (x=25, 28, 31 and 34) glasses.*
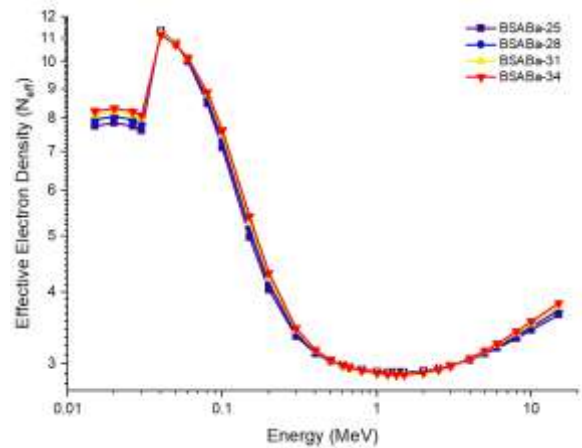

Figure 4. *Effective electron density (N_{eff}) with photon energy for energy for BSBa-x (x=25, 28, 31 and 34) glasses.*

3. Results and Discussion

Table 1 shows theoretical density, which range from 3.798 to 3.957 g/cm^3, and weight fractions of each glasses. The samples with the lowest density are BSABa-25. When density is examined in general, increase in concentration of BaO is found to have a major effect on the density of BSABa-x glasses. As can be seen in Figure 1, when the density increases LAC (μ) values, which are determined between 0.015-15 MeV photon energy range (Fig. 1 (a)), and MAC (Fig. 1 (b)) values are getting higher value than those with low density. To begin with, we can see that the LAC has distinct behavior in three different photon energy zones. In the collision phase, the photoelectric effect becomes more dominant (at 0.04 MeV) as LAC values decrease and gamma energy increases in the low energy field. The decay rates slowed as the energy level increased.
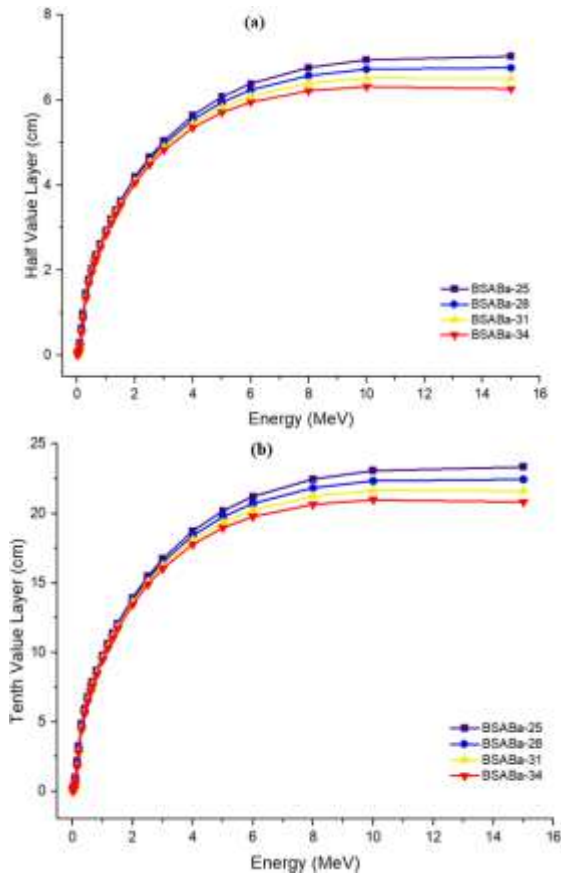
Figure 5. (a) *Variation of half-value layer (HVL)* ***(b)*** *tenth-value layer (TVL) versus photon energy for BSBa-x (x=25, 28, 31 and 34) glasses.*
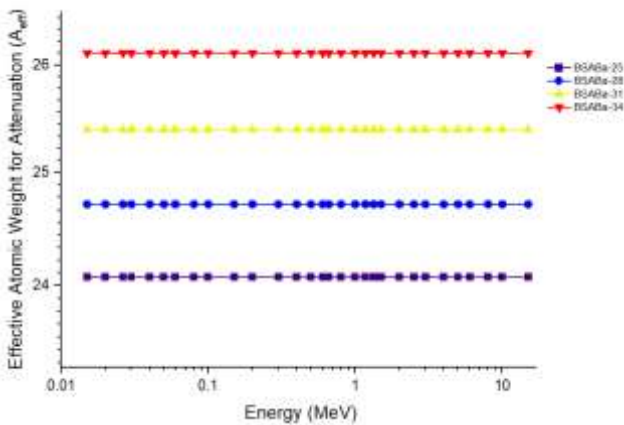

Figure 6. *Effective atomic weight for attenuation (A_{eff}) with photon energy for for BSBa-x (x=25, 28, 31 and 34) glasses.*

According to our findings, the maximum LAC values for the BSABa-34 sample are observed at the investigated photon energies. The chemical structure and theoretichal density value of the BSABa-34 sample may clarify the situation. Where the density of BSABa-25 is 3.798 g/cm^3 in the BSABa-34 and 3.957 g/cm^3 in the BSABa-34 sample.

Figure 7. (a) *Variations of exposure buildup factor (EBF)* ***(b)*** *energy absorption buildup factor (EABF) with photon energy at different mean free paths for BSABa-25 glass system.*

Figure 8. (a) *Variations of exposure buildup factor (EBF)* ***(b)*** *energy absorption buildup factor (EABF) with photon energy at different mean free paths for BSABa-28 glass system.*

Figure 9. **(a)** *Variations of exposure buildup factor (EBF)* **(b)** *energy absorption buildup factor (EABF) with photon energy at different mean free paths for BSABa-31 glass system.*
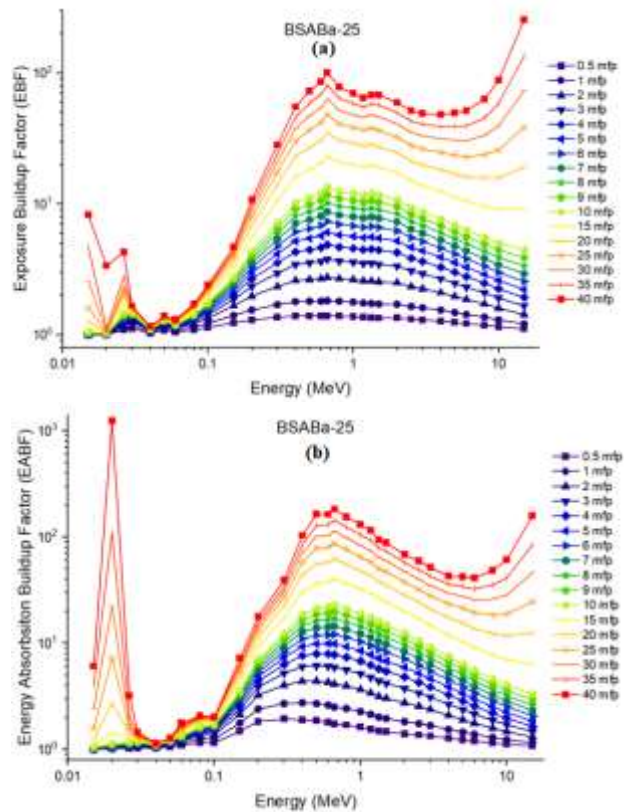

Figure 10. **(a)** *Variations of exposure buildup factor (EBF)* **(b)** *energy absorption buildup factor (EABF) with*

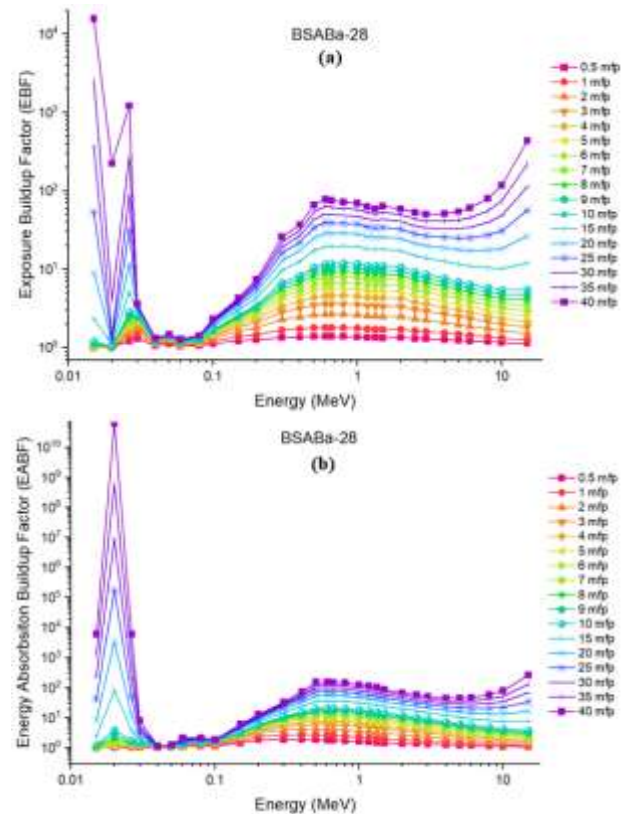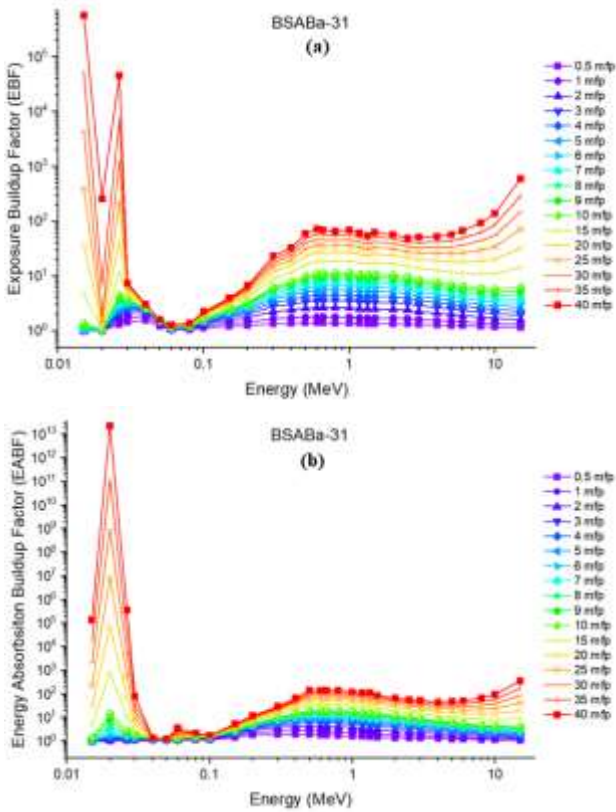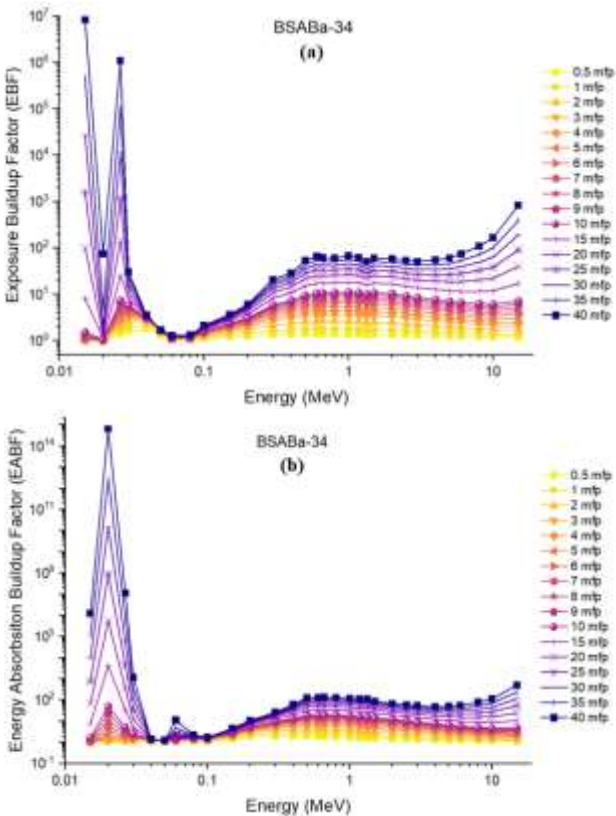*photon energy at different mean free paths for BSABa-34 glass system.*

As a result, the aforementioned substitution results in a noticeable increase in LAC values. For BSABa-25, BSABa-28, BSABa-31, and BSABa-34 samples at 0.015 MeV, LAC values are stated as 69.000 ,76.000 ,83.100 and 90.400 cm^{-1}, respectively. Furthermore, LAC values at 15 MeV (highest energy of recent investigation) are stated as 0.099, 0.103, 0.107 and 0.111, respectively. The increase in BaO content in glass samples from 25% to 34% resulted in a rigid increase in density.

The mean free path (MFP) is also a determining factor for a material's gamma shielding abilities. Figure 2 shows a graphical representation of the MFP values for four different types of glass. At various gamma ray energies, the lowest measured MFP values for the BSABa-34 sample are also reported.

In terms of gamma ray attenuation properties, the effective atomic number (Z_{eff}) is a useful term for evaluating the material's suitability for gamma-ray applications, and it is related to the partial photon mitigation process. Figure 3 shows the (Z_{eff}) of the investigated glass samples as a function of photon energy. According to the results, the maximum Z_{eff} for the BSABa-34 glass sample is reported as 48.392 for 0.04 MeV. Other BSABa-x samples have been shown to be in similar situations. Z_{eff} - BSABa-34 > BSABa-31 > BSABa-28 > BSABa-25 is the overall order of Zeff. In terms of N_{eff} values for BSABa-x glass samples, there is also a linear relationship between the effective atomic number (N_{eff}), as shown in Figure 4, with Neff-BSABa-34 > BSABa-31 > BSABa-28 > Zeff-BSABa-25 as the overall order of N_{eff} .

Investigated glasses are also tested in terms of the HVL. The term HVL is a crucial parameter for determining the thickness of shielding material needed to reduce the initial intensity by half (50%). As a result, this parameter can be used for future glass shield applications that take into account the physical environment and the suitability of shielding material placement in a given region. Figure 5 (a) illustrates the changes in the half value layer (HVL) values of the glass samples against to incident photon energy. The HVL values of glass samples increase as the incident photon energy increases. From 0.015 to 5 MeV, a rigid increment is registered. The average maximum HVL values for all glass samples are reported as 6.075, 5.949, 5.826 and 5.708 cm at 5 MeV photon energy for BSABa-25, BSABa-28, BSABa-31 and BSABa-34

samples, respectively. It can be seen that, HVL difference between BSABa-25 and BSABa-34 sample is 0.367 cm at 5 MeV. It means that BaO additive from 25 to 34% decreased the required shielding thickness as 0.367 cm for 5 MeV gamma rays. Similarly, the lowest HVL values are observed for BSABa-34 sample at all energies. This is another indicator for superior shielding properties of BSABa-34 sample against ionizing gamma rays. A similar pattern can be seen in Figure 5 (b), which shows the HVL values, which are the material depth values that enable the intensity of incoming radiation to be reduced to one-tenth of its original value. Besides, the MFP value (Figure 2) is clearly on a downward slope, similar to the HVL value.

The effective atomic weight (A_{eff}), which is known as the ratio of atomic weight to total atomic number, reaches its maximum value for BSABa-34 glass sample as seen in Figure 6. As the BaO concentration rises, the effective atomic weight value rises as well, indicating that the BSABa-34 glass becomes more radiation resistant.

The buildup factor is a correction factor for the effect of scattered radiation in the presence of secondary particles in the medium. The accumulation causes of secondary ionizing radiation must be considered when accounting for secondary ionizing radiation accumulation. As a result, the factor of accumulation is a multiplier that makes up for the reaction to non-confronted photons in order to integrate the contribution of scattered photons. The multiplier in the buildup portion absorbs non-confronted photons, allowing the contribution of scattered photons to be included. Exposure buildup factor (EBF) and energy absorption buildup factor (EABF) are two subcategories of the principle of buildup factor (EABF). The Py-MLBUF is used to measure the terms of EBF and EABF values for four BSABa-x separate glasses between 0.5 and 40 mfp. Figure 7-10 (a) describes the relationship between exposure buildup factor (EBF) and energy for various mfp values. Different chemical reactions take place in various natural settings. The first region shown peaked because the atomic number is close to the binding energy of the elements with the highest atomic numbers. As a consequence, in the Compton resonance region, the EBF values are nearly constant. The third field of interest is pair production, where there is a small rise in EBF due to absorption processes. The EBF value of the BSABa-34 sample is found to be the lowest. This is an excellent example of how well materials can shield gamma rays. As a consequence, among the investigated specimens, the best extracted sample is BSABa-34, which has the lowest EBF values. In the energy absorption buildup factor (EABF) is plotted against photon energy (MeV) from 5 to 40 mfp and a similar pattern can be seen. in Figure 7-10 (b).

4. Conclusions

In terms of radiation shielding parameters, we investigated $5B_2O_3 - 40SiO_2 - (55-x) Al_2O_3 - xBaO$ (BSABa-x) glass systems (where x = 25, 28, 31 and 34) and determined their radiation resistance properties. The glass density increased from 3.798 g/cm^3 to 3.957 g/cm^3 when the BaO concentration is increased linearly (i.e. 25, 28, 31 and 34% mole). On the other hand, from 25 to 34 mole percent BaO reinforcement, a total increase of 0.159 g/cm^3 is given (i.e. between BSABa-25 and BSABa-34). As a result, we would like to emphasize that a direct 34% mole substitution of BaO results in a net density difference of 0.159 g/cm^3. The hypothesis that the radiation resistance of glass will increase as BaO density increases is clearly validated by the results, and it can be stated that BaO has a clear effect on the radiation attenuation qualities. It can be concluded that BaO has a clear effect on the attenuation properties of radiation. The BSABa-34 with the highest BaO additive exhibits the greatest attenuation of photons, indicating that BaO reinforcement has strong anti-nuclear radiation resistance properties. Finally, in light of the scientific community's ongoing efforts on the promising lead-free barium and aluminum oxide added to borosilicate glass system, we would like to propose some potential future investigations.

Author Statements:

- The authors declare that they have equal right on this paper.
- The authors declare that they have no known competing financial interests or personal relationships that could have appeared to influence the work reported in this paper
- The authors declare that they have nobody or no-company to acknowledge.

References

[1] A.S. Abouhaswa, H.O. Tekin, E. Kavaz, U. Perisanoglu. Optical and nuclear radiation protection characteristics of lithium bismo-borate glasses: Role of ZrO_2 substitution. Radiation Physics and Chemistry,

2021.https://doi.org/10.1016/j.radphyschem.2021.109428.

[2] H.O.Tekin, L.R.P. Kassab, Shams A.M. Issa, C.D.S. Bordon, E.E. Altunsoy Guclu, G.R. da Silva Mattos, O. Kilicoglu. Synthesis and nuclear radiation shielding characterization of newly developed germanium oxide and bismuth oxide glasses. Ceramic International, 2019. https://doi.org/10.1016/j.ceramint.2019.08.204.

[3] Singh J, Singh H, Sharma J, Singh T, Singh PS. Fusible alloys: a potential candidate for gamma rays shield design. Prog. Nucl. Energy, 2018. https://doi.org/10.1016/j.pnucene.2018.04.002.

[4] Kaewkhao J., Pokaipisit A., Limsuwan P. Study on borate glass system containing with Bi_2O_3 and BaO for gamma-rays shielding materials: Comparison with PbO. Journal of Nuclear Materials 2010; 399: 38–40. https://doi.org/10.1016/j.jnucmat.2009.12.020.

[5] Sodhi K.S., Krishna S., Saxena A.K., Sinha A., Khandelwal N., Lee E.Y. Clinical application of "Justification" and "Optimization" principle of ALARA in pediatric CT imaging:'how many children can be protected from unnecessary radiation?'. Europ. Jour. Rad. 2015. https://doi.org/10.1016/j.ejrad.2015.05.030.

[6] S.A.M. Issa. Effective atomic number and mass attenuation coefficient of PbO–BaO–B_2O_3 glass system.
Radiat.Phys.Chem., 2016. https://doi.org/10.1016/j.radphyschem.2015.11.025.

[7] N. Singh, K.J. Singh, K. Singh, H. Singh. Comparative study of lead borate and bismuth lead borate glass systems as gamma-radiation shielding materials. Nucl. Instrum. Meth. Phys. Res. B 225 (2004) 305–309. https://doi.org/10.1016/j.nimb.2004.05.016

[8] Ab Latif Wani, Anjum Ara, Jawed Ahmad Usmani. Lead toxicity: a review. Interdisiplinary toxicology, 2015. https://doi.org/10.1515/intox-2015-0009.

[9] Monisha Jaıshankar, Tenzin Tseten, Naresh Anbalagan, Blessy B. Mathew , Krishnamurthy N. Beeregowda. Toxicity, mechanism and health effects of some heavy metals. Interdisiplinary toxicology, 2014. https://doi.org/10.2478/intox-2014-0009.

[10] Y.Al-Hadeethi, S.A.Tijani. The use of lead-free transparent 50BaO - (50-x) borosilicate - xBi_2O_3 glass system as radiation shields in nuclear medicine. Journal of Alloys and Compounds, 2019. https://doi.org/10.1016/j.jallcom.2019.06.259.

[11] H.O. Tekin, O. Kilicoglu. The influence of gallium (Ga) additive on nuclear radiation shielding effectiveness of Pd/Mn binary alloys. Journal of Alloys and Comp., 2019. https://doi.org/10.1016/j.jallcom.2019.152484.

[12] Ersundu A.E., Buyukyildiz M., Celikbilek Ersundu M., Sakar E., Kurudirek M. The heavy metal oxide glasses within the WO_3-MoO_3-TeO_2 system to investigate the shielding properties of radiation applications. Progress in Nuclear Energy, 2018. https://doi.org/10.1016/j.pnucene.2017.10.008.

[13] P.A. Meyer, M.J. Brown, H. Falk. Global approach to reducing lead exposure and poisoning Mutat. Res. Rev.Mutat.Res., 2008. https://doi.org/10.1016/j.mrrev.2008.03.003.

[14] K.A. Fetterly, D.J. Magnuson, G.M. Tannahill, M.D. Hindal, V. Mathew. Effective use of radiation shields to minimize operator dose during invasive cardiologyprocedures. JACC Cardiovasc. Interv., 2011. https://doi.org/10.1016/j.jcin.2011.05.027.

[15] Tijani S.A., Kamal S.M., Al-Hadeethi Y., Arib M., Hussein M.A., Wageh S., et al. Radiation shielding properties of transparent erbium zinc tellurite glass system determined at medical diagnostic energies. J. Alloy Comp., 2018. https://doi.org/10.1016/jjallcom.2018.01.109.

[16] M.A.M.Uosif, A.M.A. Mostafa Shams A.M.Issa, H.O.Tekin, Z.A. Alrowaili, O.Kilicoglu. Structural, mechanical and radiation shielding properties of newly developed tungsten lithium borate glasses: an experimental study. Journal of Non-Crystalline Solids, 2020. https://doi.org/10.1016/j.jnoncrysol.2019.119882.

[17] E.Kavaz, H.O.Tekin, G.Kilic, G.Susoy. Newly developed Zinc-Tellurite glass system: An experimental investigation on impact of Ta_2O_5 on nuclear radiation shielding ability. Journal of Non-Crystalline Solids, 2020. https://doi.org/10.1016/j.jnoncrysol.2020.120169.

[18] H.A.Saudi, H.O.Tekin, Hesham M.H. Zakalyde Shams, A.M.Issa, G.Susoy, M.Zhukovsky. The impact of samarium (III) oxide on structural, optical and radiation shielding properties of thallium-borate glasses: Experimental and numerical investigation. Optical Materials, 2021. https://doi.org/10.1016/j.optmat.2021.110948.

[19] G. Kilic, S. Issa, E. İlik, O. Kilicoglu, H.O. Tekin. A journey for exploration of Eu2O3 reinforcement effect on zinc-borate glasses: Synthesis, optical, physical and nuclear radiation shielding properties. Ceramics International, 2021. https://doi.org/10.1016/j.ceramint.2020.09.103.

[20] El-Sayed A. Waly, Michael A. Fusco, Mohamed A. Bourham. Gamma-ray mass attenuation coefficient and half value layer factor of some oxide glass shielding materials. Ann. Nucl. Energy, 2016. https://doi.org/10.1016/j.anucene.2016.05.028.

[21] R. Wu, J.D. Myers, M.J. Myers. New generation high-power rare-earth-doped phosphate glass fiber and fiber laser Proc SPIE – Solid State Lasers X, 4267 (2001), pp. 56-60. ISBN: 1-55752-661-3. https://www.osapublishing.org/abstract.cfm?URI=ASSL-2001-MB2.

[22] J. Hubbell. Photon mass attenuation and energy-absorption coefficients Int J Appl Radiat Isot, 1982. https://doi.org/10.1016/0020-708X(82)90248-4.

[23] G. Susoy, E.E.A. Guclu, O. Kilicoglu, M. Kamislioglu, M.S. Al-Buriahi, M.M. Abuzaid, H.O. Tekin. The impact of Cr_2O_3 additive on nuclear radiation shielding properties of LiF–SrO–B_2O_3 glass system. Materials Chemistry and Physics, 2020. https://doi.org/10.1016/j.matchemphys.2019.122481.

[24] C. Jayachandran. Calculated effective atomic number and kerma values for tissue-equivalent and dosimetry materials Phys Med Biol, 16 (4) (1971), p. 617. https://doi.org/10.1088/0031-9155/16/4/005.

[25] M. Taylor, R. Franich, J. Trapp, P. Johnston. Electron interaction with gel dosimeters: effective atomic numbers for collisional, radiative and total interaction processes Radiat Res, 171 (1) (2009), pp. 123-126. doi: 10.1667/RR1438.1.

[26] Mohammad W. Marashdeh, Ibrahim F. Al-Hamarneh, Eid M. Abdel Munem, , A. A. Tajuddin, A. Ariffin, Saleh Al-Omari. Determining the mass attenuation coefficient, effective atomic number, and electron density of raw wood and binderless particleboards of *Rhizophora* spp. by using Monte Carlo simulation, Results in Physics, 2015. https://doi.org/10.1016/j.rinp.2015.08.009.

[27] Kulwinder Singh Mann, Sukhmanjit Singh Mann. Py-MLBUF: Development of an online-platform for gamma-ray shielding calculations and investigations. Annals of Nuclear Energy, 2021. https://doi.org/10.1016/j.anucene.2020.107845.

[28] S. Kaewjaeng, J. Kaewkhao, P. Limsuwan, U. Maghanemi. Effect of BaO on Optical, Physical and Radiation Shielding Properties of SiO_2-B_2O_3-Al_2O_3-CaO-Na_2O Glasses System. Procedia Engineering, 2012. https://doi.org/10.1016/j.proeng.2012.02.058.

[29] Singh K., Singh H., Sharma V., Nathuram R., Khanna A., Kumar R., Bharri S.S., Sahora H.S. Gamma-ray attenuation coefficient in bismuth borate glass , Journal of Nuclear Instruments and Methods in Physics Research 2002; 194:1-6. http://dx.doi.org/10.4236/jep.2016.72023.

[30] Sing S., Kumar A., Sing D., Thind K.S. Barium-borate-flyash-glasses: As radiation shielding materials, Journal of Nuclear Instruments and Methods in Physics Research, 2008; 206:140-146. https://doi.org/10.1016/j.nimb.2007.10.018.

[31] E.Kavaz, F.I.El Agawany, H.O.Tekin, U.Perisanoglu, Y.S.Rammah. Nuclear radiation shielding using barium borosilicate glass ceramics, 2020. https://doi.org/10.1016/j.jpcs.2020.109437.

[32] U. Kara, S.A.M. Issa, G. Susoy, M Rashad, E. Kavaz, N.Y. Yorgun, H.O.Tekin. Synergistic effect of serpentine mineral on $Li_2B_4O_7$ glasses: optical, structural and nuclear radiation shielding properties. Applied Physics A, 2020. https://doi.org/10.1016/j.jnoncrysol.2020.120049.

[33] H.O. Tekin, Shams A.M. Issa, E. Kavaz. The direct effect of Er_2O_3 on bismuth barium telluro borate glasses for nuclear security applications. Mater. Res. Express., 2019. https://doi.org/10.1088/2053-1591/ab4cb5.

[34] M.M. Abuzaid, G. Susoy, S.A.M. Issa, W. Elshami, O. Kilicoglu, H.O. Tekin. Relationship between melting-conditions and gamma shielding performance of fluoro-sulfo-phosphate (FPS) glass systems: a comparative investigation. Ceramics International, 2020. https://doi.org/10.1016/j.ceramint.2020.03.065.

[35] O. Kilicoglu, H.O. Tekin. Bioactive glasses and direct effect of increased K_2O additive for nuclear shielding performance: a comparative investigation. Ceramics International, 2020. https://doi.org/10.1016/j.ceramint.2019.09.095.

[36] U. Kara, E. Kavaz, ShamsA.M.Issa, M. Rashad, G. Susoy, A.M.A. Mostafa, N. Yildiz Yorgun, H.O. Tekin. Optical, structural and nuclear radiation shielding properties of $Li_2B_4O_7$ glasses: efect of boron mineral additive. Applied Physics A, 126 (2020), p. 261. https://doi.org/10.1007/s00339-020-3397-8.

[37] H.O. Tekin, V.P. Singh, T. Manici. Effects of micro-sized and nano-sized WO_3 on mass attenauation coefficients of concrete by using MCNPX code Appl. Radiat. Isot., 2017. https://doi.org/10.1016/j.apradiso.2016.12.040.

[38] M.M. Hosamani, N.M. Badiger Determination of effective atomic number of composite materials using backscattered gamma photons – a novel

method Chem Phys. Lett, 2018. https://doi.org/10.1016/j.cplett.2018.02.012.

[39] Perisanoglu U., Kavaz E., Tekin H.O., Armoosh S.R., Ekinci N., Oltulu M. Comparison of gamma and neutron shielding competences of Fe–Cu- and brassadded Portland cement pastes: an experimental and Monte Carlo study. Appl. Phys. A Mater. Sci. Process., 2020. https://doi.org/10.1007/s00339-020-03648-6.

[40] Saddeek Y.B., Issa S.A.M., Guclu E.E.A., Kilicoglu O., Susoy G., Tekin H.O. Alkaline phosphate glasses and synergistic impact of germanium oxide (GeO2) additive: mechanical and nuclear radiation shielding behaviors.Ceram.Int., 2020. https://doi.org/10.1016/j.ceramint.2020.03.254.

[41] Tekin H.O. MCNP-X Monte Carlo code application for mass attenuation coefficients of concrete at different energies by modeling 3×3 inch NaI(Tl) detector and comparison with XCOM and Monte Carlo data. Sci. Technol.Nucl.Install., 2016. https://doi.org/10.1155/2016/6547318, 2016.

[42] Alatawi A., Alsharari A.M., Issa S.A.M., Rashad M., Darwish A.A.A., Saddeek Y.B., Tekin H.O. Improvement of mechanical properties and radiation shielding performance of AlBiBO$_3$ glasses using yttria: an experimental investigation. Ceram. Int. 2020. https://doi.org/10.1016/j.ceramint.2019.10.069.

[43] Issa Shams A.M., Susoy G., Ali A.M., Tekin H.O., Saddeek Y.B., Al-Hajry A., Algarni H., Anjana P.S., Agar O. The effective role of La2O3 contribution
on zinc borate glasses: radiation shielding and mechanical properties. Appl. Phys. A Mater. Sci. Process., 2019. https://doi.org/10.1007/s00339-019-3169-5.

[44] Kara U., Issa S.A.M., Yorgun N.Y., Kilicoglu O., Rashad M., Abuzaid M.M., Kavaz E., Tekin H.O. Optical, structural and gamma ray shielding properties of dolomite doped lithium borate glasses for radiation shielding applications. J. NonCryst. Solids, 2020. https://doi.org/10.1016/j.jnoncrysol.2020.120049.

[45] Kavaz E., Ekinci N. A study of energy absorption and exposure buildup factors in medicinal samples. Asian J. Chem., 2016. .https://doi.org/10.14233/ajchem.2016.19740.

[46] M.L. Taylor, R.L. Smith, F. Dossing, R.D. Franich. Robust calculation of effective atomic numbers: the Auto-Z$_{eff}$ software Med Phys, 2012. https://doi.org/10.1118/1.3689810.

[47] S. Gowda, S. Krishnaveni, R. Gowda. Studies on effective atomic numbers and electron densities in amino acids and sugars in the energy range 30-1333 keV. Nucl Instrum Methods B, 2005. https://doi.org/10.1016/j.nimb.2005.05.048.

[48] M.F. Kaplan Concrete radiation shielding John Wiley & Sons Inc, New York (1989). ISBN 0-470-21338-8.

[49] B. Alim, Determination of Radiation Protection Features of the Ag$_2$O Doped Boro-Tellurite Glasses Using Phy-X / PSD Software, Journal of the Institute of Science and Technology, 2020. https://doi.org/10.21597/jist.640027.

Erratum

Erratum to "Study on Determination Method of Inter Well Pumping System for Liquid Supply Shortage Well"
[IJCESEN 6-2(2020)82-87 doi: 10.22399/ijcesen.693839]

Xingyuan LIANG[1*], Jiang LEI[2], Yi LU[3]

[1]China University of Petroleum, Beijing Unconventional Oil and gas Scientific and Technology Department, 102249, Beijing-China
* **Corresponding Author** : lxypetro@163.com-- **ORCID:** 0000-0002-7583-3969

[2]Drilling & Production Technology Research Institute, CNPC Chuanqing Drilling Engineering Co., Ltd.,710018,Xiaan-China
leijiangcq@163.com - **ORCID:** 0000-0002-5487-4550

[3]Eighth Oilfield Operation, CNPC Changqing Oil Field Company, 710018,Xiaan-China
584676718@qq.com - **ORCID:**0000-0002-7583-3968

Article Info:

This paper represent correction of some information previously published paper (IJCESEN 6-2(2020)82-87 doi: 10.22399/ijcesen.693839). The details are given below.

Details of Errata:

1. Abstract: "The wells with deficient-liquid supply account for 20%-30% for all production wells, the proportion of the oil field in the long production time is greater." should be "The wells with deficient-liquid supply account for large proportion for all production wells, the proportion of the oil field in the long production time is greater."

2. Abstract: "Get the time of open well; through analyzing the relationship between the inflow performance of oil wells and the submergence to determine the close time" should be "also studied the increasing law."

3. Equation (3), (4), (8), (9) are delated.

4. Part 2.4 and 2.5 are delated.

5.Conclusion should be "We studied the intermittent system for liquid shortage wells and realized the importance of intermittent for oil operation. We also studied the variation law of annulus dynamic liquid depth and got the ground dynamometer card from electrical power curve. We conclude two conclusions, which are as follows: we draw the dynamometer card from electrical power curve, which can calculate the dynamic liquid depth. Both of the decrease and rise speed of submergence depth are first quick back slow, during the open and shut-in period."

The authors would apologize for any inconvenience caused.